Magnetite as an Indicator Mineral in Till: A Test Using the Mount Polley Porphyry Cu-Au Deposit, British Columbia

by

Laura Pisiak
B.Sc., University of Manitoba, 2011

A Thesis Submitted in Partial Fulfillment
of the Requirements for the Degree of

MASTER OF SCIENCE

in the School of Earth and Ocean Sciences

© Laura Pisiak, 2015
University of Victoria

All rights reserved. This thesis may not be reproduced in whole or in part, by photocopy
or other means, without the permission of the author.

Supervisory Committee

Magnetite as an Indicator Mineral in Till: A Test Using the Mount Polley Porphyry Cu-Au Deposit, British Columbia

by

Laura Pisiak
B.Sc., University of Manitoba, 2011

Supervisory Committee

Dr. Dante Canil (School of Earth and Ocean Sciences)
Supervisor

Dr. Laurence Coogan (School of Earth and Ocean Sciences)
Departmental Member

Dr. Stephen Rowins (School of Earth and Ocean Sciences)
Departmental Member

Abstract

Supervisory Committee
Dr. Dante Canil (School of Earth and Ocean Sciences)
Supervisor
Dr. Laurence Coogan (School of Earth and Ocean Sciences)
Departmental Member
Dr. Stephen Rowins (School of Earth and Ocean Sciences)
Departmental Member

In the Canadian Cordillera, Mesozoic calcalkaline and alkaline intrusive igneous rocks that are prospective for hosting porphyry Cu-Au mineralization may be overlain by thick glacial overburden. Previous studies have shown that magnetite from ore deposits has a unique trace element signature that differs from magnetite in common igneous or metamorphic rocks. This study investigated if the composition of ore-related magnetite in till could provide a unique exploration tool to locate porphyry deposits in glaciated terrain. Bulk till samples were collected over an area of ~700 km^2 surrounding the Mount Polley porphyry Cu-Au deposit, south-central British Columbia. Twenty elements were measured by LA-ICP-MS in ~50 detrital magnetite grains in each of 20 till samples. Previously proposed discrimination diagrams are proven to be of limited use in correctly identifying ore-related magnetite. Therefore, linear discriminant analysis (LDA) was performed on a compiled dataset of magnetite compositions from various porphyry deposits and intrusive igneous rocks in order to rigorously redefine the chemical signature of hydrothermal magnetite from porphyry systems. Application of the LDA models to magnetite in till found that the dispersal of hydrothermal grains from Mount Polley is coincident with the deposit and the interpreted ice-flow history. Anomalous concentrations of hydrothermal magnetite grains in till are detected up to 2.5 km west-southwest and 4 km northwest of the deposit, indicating that magnetite has a strong potential to be an effective indicator in mineral exploration for porphyry systems.

Table of Contents

Supervisory Committee ii
Abstract iii
Table of Contents iv
List of Tables vi
List of Figures vii
Acknowledgments xi
1. Introduction 1
1.1 Spinel Group: Mineralogy and Crystallography 1
1.2 Magnetite in Hydrothermal Porphyry Systems 2
1.3 Magnetite as an Indicator Mineral 4
1.4 Ground-Truth Study of Magnetite as a Porphyry Indicator Mineral 7
1.5 Research Objectives 9
2. Geological Setting 12
2.1 Location and Physiography 12
2.2 Regional Geology 12
2.3 Deposit Geology 13
2.4 Glacial History 17
3. Methodology 18
3.1 Till Sampling Survey 18
3.2 Sample Preparation 18
3.3 Petrography 21
3.4 Electron Microprobe Analysis 21
3.5 Laser Ablation-Inductively Coupled Plasma-Mass Spectrometry 22
4. Petrography 25
5. Chemistry 29
5.1 Comparison of Analytical Methods 29
5.2 “Sphenitization”: High Si and Ca in Magnetite 34
5.3 Magnetite Compositional Variability 38
6. Discussion 45
6.1 How to Distinguish Hydrothermal Magnetite 45
6.1.1 Discrimination Diagrams 45
6.1.2 Statistical Analysis 52
6.2 Application to the Mount Polley Porphyry Cu-Au Deposit 70
6.2.1 Identification of Magnetite in Till 70
6.2.2 Magnetite as an Indicator Mineral at Mount Polley 77
7. Conclusions 84
7.1 Summary 84
7.2 Future Work & Recommendations 86

Bibliography 89
Appendix A. Till Sample Locations 97
Appendix B. Magnetite from Till: Petrography, LA-ICP-MS Compositional Data & LDA Classification..... 99
Appendix C. Detection Limits for EMP Analysis 100
Appendix D. Accuracy and Precision of LA-ICP-MS Analysis..... 101
Appendix E. SYSTAT 13 Output for Linear Discriminant Analysis 108
Linear Discriminant Analysis: MDB1 108
Linear Discriminant Analysis: MDB2 111

List of Tables

Table 1. Detection limits, accuracy and precision for magnetite LA-ICP-MS analysis. . **24**

Table 2. Summary of magnetite compositional data obtained from various porphyry deposits and barren igneous intrusions. **53**

Table 3. Summary statistics for magnetite compositional groups in the MDB1 dataset. **55**

Table 4. Summary statistics for magnetite compositional groups in the MDB2 dataset. **56**

Table 5. Wilks lambda (λ) values as determined by forward stepwise linear discriminant analysis..... **62**

Table 6. Linear discriminant analysis classification summary of independent test data. **64**

Table 7. Linear discriminant analysis classification summary for individual magnetite groups..... **65**

Table 8. Results of linear discriminant analysis..... **66**

Table 9. Equations for field boundaries separating magnetite compositional groups. **69**

Table 10. Classification results for magnetite grains in till..... **73**

Table 11. Coordinates for 74 till sample locations in the vicinity of the Mount Polley porphyry Cu-Au deposit. **97**

Table 12. Minimum, mean and maximum detection limits for electron microprobe analysis..... **100**

List of Figures

Figure 1. Location map and tectonostratigraphic setting of the Mount Polley porphyry Cu-Au deposit, British Columbia (modified from Colpron & Nelson, 2011). **8**

Figure 2. Regional geology and mineral occurrences in the Mount Polley study area (modified from Plouffe et al., 2013a; bedrock geology from Logan et al., 2010). A detailed map of deposit geology is provided by Rees (2013) through a compilation of surface mapping and drill core data..... **14**

Figure 3. Till sampling locations in the Mount Polley study area (red dot). Samples analyzed in this study are indicated as larger symbols. Locations for Mount Polley bedrock samples are also shown (blue dot). Modified from Plouffe et al. (2013a). Bedrock geology from Logan et al. (2010) – legend in Figure 2. ..... **19**

Figure 4. A) Initial magnetic fraction of heavy mineral concentrates from till (sample 12 PMA 586 A01); B) Magnetite grain selection following sample refinement..... **20**

Figure 5. Petrographic varieties of magnetite from till in reflected light at 20 times magnification. A) Euhedral, homogeneous magnetite grain with 100 µm long laser-ablation raster, apatite (Ap) inclusion and minor hematite (Hem) alteration patches (sample 12 PMA 081 A01-C3). B) Subhedral magnetite grain with ilmenite (Ilm) trellis lamellae and 110 µm long laser-ablation raster (12 PMA 077 A01-D1). C) Subhedral magnetite grain with very fine trellis lamellae, potassium feldspar (Kfs) and apatite inclusions, hematite alteration, and two 30 µm laser-ablation spots (12 PMA 088 A01-D4). D) Subrounded, heterogeneous magnetite grain with fine trellis lamellae, hematite alteration, as well as blebby titanite (Ttn) predominantly concentrated in the core (12 PMA 087 A01-G6). ... **26**

Figure 6. Back-scattered electron (BSE) images of magnetite. A) Coarse ulvöspinel (Usp) and rutile (Rt) lamellae with an interstitial, fine, dark trellis lamellae of a Si-Al-Mg-rich phase (sample 12 PMA 095 A01-C11). B) Submicroscopic ilmenite (Ilm) lamellae in magnetite (12 PMA 095 A01-A15). C) Preferential titanite (Ttn) alteration of ilmenite lamellae in magnetite (12 PMA 585 A01-F4). D) Stringers and disseminations of titanite in magnetite (12 PMA 088 A01-B15). **27**

Figure 7. A comparison of LA-ICP-MS calibration methods using Ti concentrations in magnetite as a representative example of calibration for a major element. A 1:1 reference line (solid black) and data trendline (dotted) are shown. Good correlation of data (R^2 = 0.98) is observed between calibration methods, however, calibration by the 'stoichiometric Fe' method consistently produces the highest element values (A). Element concentrations

determined by AYCF calibration closely approximates the 'EMP Fe' method as illustrated by the close proximity of data to the 1:1 reference line (B). **31**

Figure 8. A comparison of LA-ICP-MS calibration methods using Cr concentrations in magnetite as a representative example of calibration for a trace element. A 1:1 reference line (solid black) and data trendline (dotted) are shown. Good correlation of data (R^2 > 0.99) is observed between calibration methods, however, calibration by the 'stoichiometric Fe' method consistently produces the highest element values (A). Element concentrations determined by AYCF calibration closely approximates the 'EMP Fe' method as illustrated by the close proximity of data to the 1:1 reference line (B). **32**

Figure 9. A comparison of LA-ICP-MS and EMP analytical methods for magnetite. A) Good correlation is observed for Cr between the two techniques, however, the EMP performs poorly when close to the detection limit as indicated by data scatter below ~1000 ppm. B) Significant scatter is present in Ti between the two techniques, likely the result of discrepancies between the techniques caused by the small EMP beam size unable to homogenize exsolution lamellae with host magnetite. **33**

Figure 10. Ca and Si contents in magnetite normalized to their molecular weight to show approximate atomic proportions. A positive 1:1 correlation is consistent with variable mixing of magnetite (at the origin) with titanite (plots off axes). Several magnetite grains from till with high Si and low Ca may indicate potential interference by minute silicate inclusions in these grains, or possible Si in solid solution, but this is not prevalent. Mount Polley magnetite data was obtained from Canil et al. (in press) and re-calibrated using the AYCF method. **36**

Figure 11 (next page). Select binary plots showing the variation in magnetite chemistry from till. Magnetite data from Canil et al. (in press) for Mount Polley and other porphyry deposits in British Columbia were re-calibrated using the AYCF method. Magnetite data from porphyry deposits in the southwest United States is from Nadoll et al. (2015). Positive correlations are exhibited between elements on all binary plots, with the following notable exceptions: B) Mount Polley tends to higher V contents compared to all other porphyry deposits, as well as most magnetite in till; C,F) The Mg-Al and Ga-Mn relationships in magnetite from till is not apparent in hydrothermal magnetite; and H) The Sc-Sn correlation in hydrothermal magnetite is not observed in magnetite from till. **40**

Figure 12. Ni/(Cr+Mn) vs. Ti+V plot for magnetite compositions with discrimination fields from Dupuis & Beaudoin (2011). Magnetite from Mount Polley plots at much lower Ni/(Cr+Mn) values than that proposed for porphyry deposits due to relatively high Mn concentrations at the deposit (data from Canil et al., in press – recalculated using the AYCF calibration method). Most magnetite grains in till plot in the Fe-Ti-V field with very few grains overlapping the porphyry field. **46**

Figure 13. Ca+Al+Mn vs. Ti+V plot of magnetite compositions with discrimination fields from Dupuis & Beaudoin (2011). Magnetite from Mount Polley plots slightly above the porphyry field based on relatively high Mn concentrations (data from Canil et al., in press – recalculated using the AYCF calibration method). Similar to Figure 11, magnetite in till predominantly plots in the Fe-Ti-V field with minor overlap with the porphyry field. ... **48**

Figure 14. Al+Mn vs. Ti+V plot of magnetite compositions with skarn and porphyry discrimination fields from Nadoll et al. (2015). The skarn+porphyry field is a transitional zone between the two deposit types. Magnetite from Mount Polley is successfully classified as porphyry magnetite, with the exception of one analysis (data from Canil et al., in press – recalculated using the AYCF calibration method). There is no distinction for igneous magnetite, therefore, magnetite data from barren igneous intrusions in the Cordillera (Mountjoy, 2011) and till are erroneously classified as porphyry magnetite. **49**

Figure 15. Ti vs. Ni/Cr plot of magnetite compositions with igneous and hydrothermal discrimination fields from Dare et al. (2014). Analyses with Cr values below detection were assigned the detection limit value of 1.76 ppm, which gives the minimum value for Ni/Cr. Magnetite from Mount Polley is successfully classified as porphyry magnetite (data from Canil et al., in press – recalculated using the AYCF calibration method). Magnetite from till is predominantly classified as igneous, but a small proportion of grains overlap into the hydrothermal field..... **51**

Figure 16. Box and whisker plots showing variation for minor elements Mg, Al, Ti, V and Mn in the compositional groups of magnetite classified from barren igneous rocks (BIG), ore-related igneous rocks (OIG) and hydrothermal porphyry related (HTP) for A) MDB1 and B) MDB2. The two datasets are broadly similar, with the exception of lower Al and Ti values in BIG from MDB2. ..... **58**

Figure 17. Box and whisker plots showing variation for trace elements Co, Ni and Sn in the compositional groups of magnetite classified from barren igneous rocks (BIG), ore-related igneous rocks (OIG) and hydrothermal porphyry related (HTP) for A) MDB1 and B) MDB2. Note that Sn was not included in MDB2 due to an insufficient number of analyses. **59**

Figure 18. Territorial plots of the discriminant scores for the full MDB1 and MDB2 training datasets for linear discriminant analyses LDA1 (A) and LDA2 (B). Equations for the boundaries between the compositional groups are given in Table 9. Scores of group means indicated as black diamonds in each respective field. Abbreviations: HTP – hydrothermal porphyry, OIG – ore-related igneous, BIG – barren igneous. **68**

Figure 19. Territorial plots of the discriminant scores for magnetite in till using the linear functions of LDA1 (A) and LDA2 (B). Equations for the boundaries between the

compositional groups are given in Table 9. A total of 71 magnetite grains in till are classified as hydrothermal (HTP) using LDA1, whereas 93 magnetite grains are classified as hydrothermal using LDA2. Abbreviations: HTP – hydrothermal porphyry, OIG – ore igneous, BIG – barren igneous..... **72**

Figure 20. The percentage of hydrothermal porphyry (HTP) magnetite grains identified in each till sample using the three different methods of classification. The proportion of HTP grains in till are generally consistent between the LDA1 and LDA2 models (A), whereas there is less agreement between the LDA models and the Ti-Ni/Cr discrimination diagram (B,C)..... **75**

Figure 21. Hydrothermal magnetite grains determined by A) LDA1 and B) LDA2 are plotted on the Ti vs. Ni/Cr diagram with igneous and hydrothermal fields from Dare et al. (2014). Most magnetite grains from LDA do not coincide with the proposed hydrothermal field illustrating the discrepancy between the methods of classification for magnetite compositions. **76**

Figure 22. The percentage of hydrothermal porphyry magnetite (HTP) grains in each till sample as determined by the LDA1 model plotted on the geological map for each sample location. Symbol size is proportional to percentage HTP magnetite grains in the sample. Modified from Plouffe et al. (2013a). Bedrock geology from Logan et al. (2010) – legend in Figure 2. ..... **78**

Figure 23. The percentage of hydrothermal porphyry magnetite (HTP) grains in each till sample as determined by the LDA2 model plotted on the geological map for each sample location. Symbol size is proportional to percentage HTP magnetite grains in the sample. Modified from Plouffe et al. (2013a). Bedrock geology from Logan et al. (2010) – legend in Figure 2. ..... **79**

Figure 24. The percentage of hydrothermal (HT) magnetite grains in each till sample as determined by the Ti-Ni/Cr discrimination diagram of Dare et al. (2014) plotted on the geological map for each sample location. Symbol size is proportional to percentage hydrothermal magnetite grains in the sample. Modified from Plouffe et al. (2013a). Bedrock geology from Logan et al. (2010) – legend in Figure 2. ..... **80**

Figure 25. Accuracy of LA-ICP-MS analyses recorded from September 16, 2013 through April 20, 2015 using the USGS basaltic glass reference BCR2g. **101**

Acknowledgments

I would like to sincerely thank my supervisor, Dante Canil, for his guidance (and patience) throughout this project. Thank you to Laurence Coogan, Steve Rowins, Dan Marshall, Alain Plouffe, Travis Ferbey, Bob Anderson and Carter Grondahl for their assistance and input in the project. A very large thank you goes out to Jody Spence for hours of analytical assistance and to Terri Lacourse for help with statistical analysis. Lastly, thank you to the Society of Economic Geologists and BC Geoscience for their scholarship support. This study was also supported by research grants from Natural Sciences and Engineering Research Council of Canada (NSERC) and BC Ministry of Energy and Mines. Till sampling was funded by the Geological Survey of Canada's Targeted Geoscience Initiative-4 program.

1. Introduction

1.1 Spinel Group: Mineralogy and Crystallography

The spinel group comprises the cubic oxide minerals (space group *Fd3m*) that are found in many types of igneous, metamorphic and sedimentary rocks. Spinels are of the general formula AB_2O_4, where A and B are divalent and trivalent cations, respectively. Oxygen atoms are arranged in layers of cubic close packing with cations occupying interstices in the oxygen framework as tetrahedral and octahedral coordination polyhedra (Waychunas, 1991). The spinel unit cell consists of 32 oxygen atoms with 8 tetrahedral and 16 octahedral sites, for which two end-member spinel structures occur based on cation distribution (Verwey & Heilmann, 1947). In a 'normal' spinel, A cations occupy tetrahedral sites and B cations occupy octahedral sites, whereas in an 'inverse' spinel, A cations occupy half of the octahedral sites and B cations are split equally between them. A more appropriate formula for an inverse spinel is $B[AB]O_4$, where square brackets identify cations in octahedral coordination.

Extensive solid solution exists between spinel group end-members, for which there are three main series based on the dominant B cation: the spinel series (Al^{3+}), magnetite series (Fe^{3+}) and chromite series (Cr^{3+}). Typically, the A cation is Mg^{2+} or Fe^{2+}, but there are a number of other divalent cations that commonly substitute including Mn, Ni, Co and Zn that form other important, but less common, spinel group minerals such as gahnite ($ZnAl_2O_4$) and trevorite ($NiFe^{3+}{}_2O_4$). Similarly, V^{3+}, Ga^{3+} and Ti^{4+} are common substituting elements for the B cation, however, tetravalent cations require coupled substitution with a divalent cation to maintain charge neutrality. There is considerable

flexibility in the spinel structure, which allows for the accommodation of a number of other elements with variable ionic radius and charge (+1 to +6; Lindsley, 1976).

The chemical variability of the spinel group minerals and their ubiquity in a wide range of igneous and metamorphic rocks have led to the recognition of systematic compositional variations as a function of the geological environment during formation. A number of classic studies have shown that in addition to crystallographic factors such as ionic radius and charge balance, physicochemical parameters including temperature, pressure, cooling rate, fO_2, fS_2, silica activity, and the composition of melt or fluid play an important role in element partitioning in spinel group minerals (Buddington & Lindsley, 1964; Irvine, 1965; Frost, 1991). Extensive study of spinel chemistry over a wide range of temperature and pressure conditions have led to a long history of application as a petrogenetic indicator in many different rock types (e.g., Irvine, 1967; Dick & Bullen, 1984; Allan et al., 1988; Sack & Ghiorso, 1991; Roeder, 1994; Barnes & Roeder, 2001; Dare et al., 2012, 2014).

1.2 Magnetite in Hydrothermal Porphyry Systems

Magnetite is the most abundant of all spinel group minerals and occurs in a wide range of geological environments including many types of ore deposits. Magnetite has the general formula $Fe^{2+}Fe^{3+}{}_2O_4$ with the inverse structure whereby Fe^{2+} occurs in octahedral coordination sites and Fe^{3+} is distributed over both octahedral and tetrahedral sites. Extensive solid solution occurs between magnetite and ulvöspinel ($Fe^{2+}{}_2TiO_4$) with intermediate members generally referred to as ‘titanomagnetites’. Titanium substitution in magnetite typically occurs as a coupled exchange of Ti^{4+} for Fe^{3+} in the octahedral site and

Fe^{2+} for Fe^{3+} in the tetrahedral site, which is directly linked to temperature and, to a lesser extent, fO_2 (Buddington & Lindsley, 1964; Waychunas, 1991).

Magnetite occurs in a number of hydrothermal ore-forming environments, such as porphyry systems, where it precipitates from hydrothermal solution with various other minerals. In high-temperature magmatic-hydrothermal fluids, Fe is one of the most abundant solutes and is primarily transported as the neutral chloride complex $FeCl_2$ (Chou & Eugster, 1977). In porphyry systems magnetite typically precipitates by reaction with SO_2 (Eq. 1), which is the dominant sulfur species in high-temperature, moderately oxidized, sulfur-rich fluids derived from arc magmas (Richards, 2015). Precipitation can occur by a variety of mechanisms including decreasing temperature, changes in fluid chemistry by fluid-rock interaction or fluid mixing, or increasing pH of the fluid by reactions such as:

$$9FeCl_2 + SO_2 + 10H_2O \rightarrow 3Fe_3O_4^{mag} + H_2S + 18H^+ + 18Cl^- \quad (1)$$

Hydrothermal magnetite precipitates during virtually all stages of hydrothermal alteration in porphyry Cu systems, but is primarily associated with extensive K-silicate alteration or with Ca-Na-silicate alteration that predominates in deeper parts of the porphyry system (Sillitoe, 2000). In these alteration zones magnetite occurs as disseminated grains, clots, massive aggregates and veinlets that can precede or be accompanied by sulphide mineralization (Sillitoe, 2000). Magnetite may also form during metasomatic replacement of country rock forming skarn deposits adjacent to the host igneous intrusion.

1.3 Magnetite as an Indicator Mineral

Indicator minerals have long been used in provenance studies and mineral exploration in areas of extensive overburden. A specific type of bedrock lithology or the presence of mineralization is indicated by the physical and/or chemical characteristics of resistate minerals in till, soil or stream sediments. These resistate indicator minerals have proven successful in locating a variety of mineral deposit types including diamondiferous kimberlite pipes and base metal sulphides (Averill, 2001). There have been numerous studies on the application of magnetite as an indicator mineral in provenance research for a variety of igneous rock types (Grigsby, 1990; Razjigaeva & Naumova, 1992; Yang et al., 2009). Magnetite is relatively robust as it is resistant to supergene weathering and physical abrasion during transport, whereas other potential porphyry minerals such as sulphides can rapidly break down in the oxidizing surficial environment (Averill, 2001). Additionally, magnetite is easily identified and separated from heavy mineral concentrates due to its strong magnetism. Only recently, with increased demand for new pathfinders in mineral exploration, is magnetite being examined as a potential indicator mineral for fingerprinting various types of hydrothermal ore deposits.

The chemistry of hydrothermal magnetite has been investigated in a variety of ore deposits including skarn, Fe-oxide-Cu-Au (IOCG) and porphyry Cu(-Mo-Au) (e.g., McQueen & Cross, 1998; Carew, 2004; Kamvong et al., 2007; Dupuis & Beaudoin, 2011; Nadoll et al., 2012, 2014, 2015; Huang et al., 2014; Dare et al., 2014; Chen et al., 2015; Canil et al., in press). These studies suggest that the variation in minor and trace element contents in magnetite is systematically related to the type of mineralizing environment. It is well known that the composition of spinel group minerals is related to the

physicochemical conditions during its formation (Buddington & Lindsley, 1964; Irvine, 1965; Frost, 1991), however, there is lack of experimental and thermodynamic data for magnetite crystallizing from hydrothermal fluids. The same conditions that govern the composition of magmatic magnetite is broadly applicable to hydrothermal systems with the added complexities of lower temperature and short time duration of many porphyry systems that make it difficult to obtain equilibrium and can result in compositional heterogeneity in hydrothermal magnetite (Canil et al., in press).

Several studies have used an empirical approach to fingerprint the chemical signature of magnetite from various hydrothermal ore-forming environments by employing simple binary plots with various element combinations or ratios. Dupuis & Beaudoin (2011) developed discrimination diagrams using average Fe-oxide compositions determined by electron microprobe (EMP) for a number of deposit types including IOCG, Kiruna, banded iron formation, porphyry Cu, skarn, Fe-Ti-V, Ni-Cu-PGE and volcanogenic massive sulphide. Application of the Ni+Cr vs. Si+Mg discrimination diagram has proved successful in differentiating Ni-Cu-PGE deposits (Dare et al., 2012; Boutroy et al., 2014). The Ni/(Cr+Mn) vs. Ti+V and Ca+Al+Mn vs. Ti+V diagrams proposed to distinguish a number of other deposit types, including porphyry Cu, have had limited success (Nadoll et al., 2014; Canil et al., in press).

Dare et al. (2014) used LA-ICP-MS data from a variety of hydrothermal ore deposits and igneous rocks to broadly distinguish hydrothermal from igneous magnetite using Ti vs. Ni/Cr. They suggest that the behavior of Ni and Cr is coupled in silicate magmas, whereby Ni/Cr < 1 for all igneous magnetite including Ti-poor magnetite from felsic rocks. Despite a lack of experimental evidence, they state that Ni probably has much

greater solubility in fluids compared to Cr, therefore Ni/Cr > 1 for hydrothermal magnetite. The application of this discrimination diagram by Canil et al. (in press) to several porphyry deposits in the Canadian Cordillera proved successful using mean sample values.

A number of other studies employed various types of multivariate statistical analyses to understand the compositional variance of magnetite in a dataset. Nadoll et al. (2012) used factor analysis to identify five factors that are able to discriminate between igneous, low-temperature hydrothermal and metamorphic magnetite in the Belt Supergroup, United States. They determined that hydrothermal magnetite has elevated values for the Mg-Mn factor, whereas igneous magnetite can be identified by high values for Co-Ni-V. Nadoll et al. (2015) calculated discriminant measures on magnetite from porphyry Cu and skarn deposits, as well as their respective host rocks, in the southwestern United States. They identified Mg, Al, Ti, V, Mn, Co, Zn and Ga as key elements that account for the compositional variation in magnetite and propose Al+Mn vs. Ti+V to broadly discriminate porphyry and skarn magnetite, although no distinction for igneous magnetite was made. Canil et al. (in press) employed principal components analysis on hydrothermal magnetite from porphyry Cu(-Au-Mo) and skarn deposits in the Canadian Cordillera and determined two trace element patterns that explain a large proportion of the compositional variability: 1) positive correlations of Al, Ti and V related to temperature and fO_2, and 2) negative correlations of high valence Sn and Mo with low valence Mn and Co related to fluid chemistry or metal speciation.

The aforementioned studies contribute to an overall better understanding of the compositional variation in magnetite and the controls by which element substitution takes place under hydrothermal conditions. The systematic variation in magnetite chemistry

advocates for further evaluation of magnetite as a tool for fingerprinting various types of ore deposits. Since previous work lacks direct application to an existing hydrothermal ore deposit in an exploration context, a ground-truth study near a well-known, exposed mineralized system can be used to test if the proposed discrimination methods of such studies work for various types of ore deposits.

1.4 Ground-Truth Study of Magnetite as a Porphyry Indicator Mineral

The Canadian Cordillera is an ideal setting to test the potential of magnetite as an indicator mineral as it is predominantly composed of accreted magmatic arcs (Fig. 1; Dickinson, 2004). The low level of denudation in many accreted terranes in the Cordillera provides a favorable geology to explore for porphyry mineralization. Calcalkaline and alkaline igneous rocks in the accreted arcs are host to numerous porphyry deposits variably enriched in Cu, Au, Mo, Ag, Sn, and W (Sinclair, 2007).

Quaternary glaciation has resulted in a locally extensive, unconsolidated, sediment cover that masks bedrock geology and challenges mineral exploration because new deposits are likely buried beneath thick overburden. Current exploration methods in the Canadian Cordillera rely strongly on bulk geochemical anomalies of ore-related elements (e.g., Cu, As, Mo, Ag and Au) in till or stream sediments. Ambiguities often arise in interpreting this type of geochemical data due to the varied and differential behavior of pathfinder elements during weathering and surface runoff. Alternatively, sediment dispersal trains produced by resistate minerals in basal till have been reliably detected several kilometers down-ice from bedrock sources (Whiting & Faure, 1991; Levson, 2001;

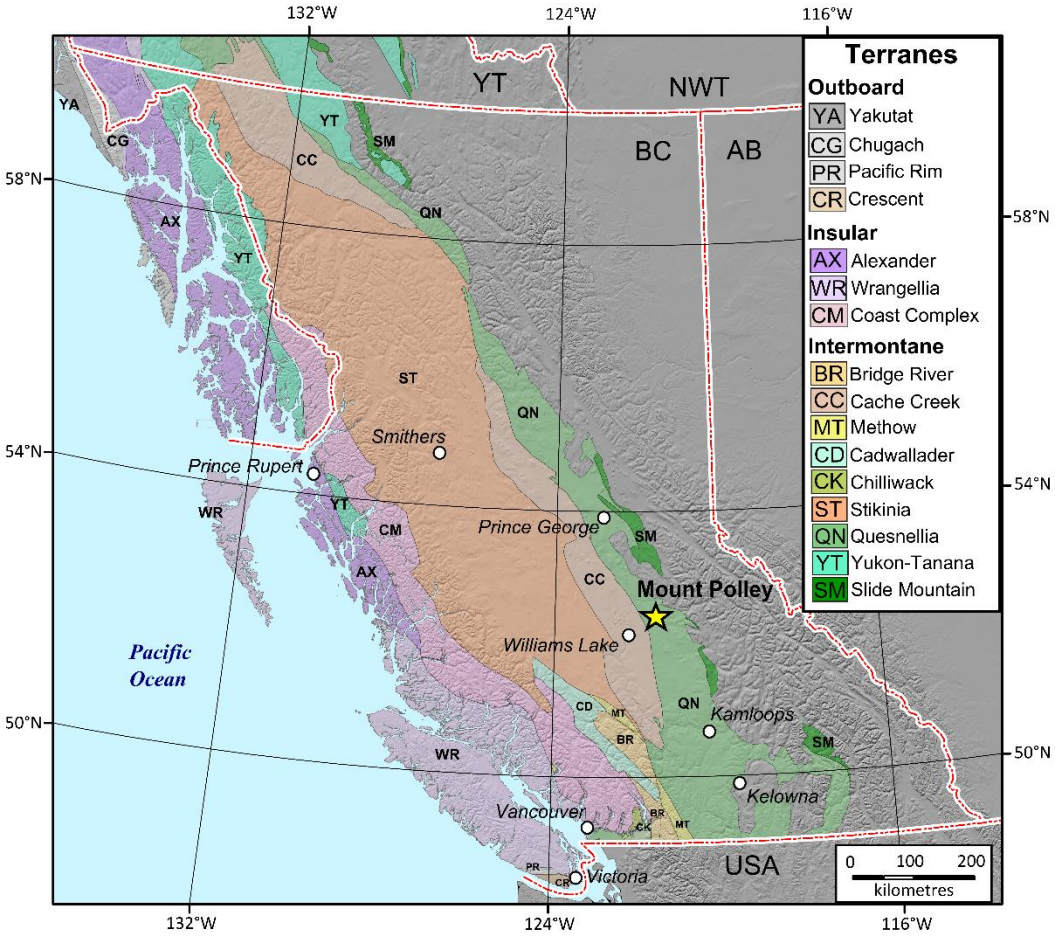

Figure 1. Location map and tectonostratigraphic setting of the Mount Polley porphyry Cu-Au deposit, British Columbia (modified from Colpron & Nelson, 2011).

Sappin et al., 2014). If there is sufficient knowledge of ice-flow history and directions in the Cordillera, this can be used as a drift prospecting method for the delineation of exploration targets. In this regard, the Mount Polley porphyry Cu-Au deposit (Fig. 1) presents an ideal location to test the use of magnetite composition in till as an indicator mineral for porphyry Cu deposit exploration. A systematic till sampling survey has been performed surrounding the Mount Polley deposit, and the ice-flow history of the region has been well-studied and reasonably constrained (Plouffe et al., 2013a; Hashmi, 2015). In addition, the trace element composition of magnetite from bedrock and lithologies hosting the Cu-Au ore has been recently studied (Canil et al., in press).

1.5 Research Objectives

This research is part of the Natural Resources of Canada's Targeted Geoscience Initiative 4 (TGI-4) program, which is aimed at developing new exploration strategies for effective targeting of mineral deposits. The overall goal of this study was to evaluate the potential of magnetite trace element chemistry as an indicator mineral in drift prospecting for mineralized porphyry systems. Three main objectives for this study are:

1) Determine the minor and trace element composition of magnetite grains in till sampled at various locations surrounding the Mount Polley porphyry deposit using laser ablation-inductively coupled plasma-mass spectrometry (LA-ICP-MS).
2) Statistically and objectively define a chemical signature of hydrothermal magnetite from mineralized porphyry systems using discriminant analysis applied to a large database of magnetite compositions, and develop unique classification functions that can be applied to unknown magnetite grains to determine provenance.

3) Critically evaluate magnetite as a potential indicator by application of the discriminant functions to magnetite grains analyzed from tills sampled in the region surrounding the Mount Polley deposit, and interpret any resulting anomalies.

This study utilized LA-ICP-MS to fully characterize magnetite composition as it provides trace element concentrations with very low detection limits. An initial goal was to determine the optimum method of gathering and calibrating LA-ICP-MS data that would be most efficient and favorable for application in mineral exploration.

A second related fundamental goal was to define the signature of hydrothermal magnetite from mineralized porphyry systems using a more rigorous approach than those previously proposed. For this purpose, discriminant analysis was selected as it is a multivariate statistical method that uses the collective significance of the variables (i.e., elements) to distinguish sources. The magnetite compositional database was obtained from Mountjoy (2011), Nadoll et al. (2015) and Canil et al. (in press), in order to have a sufficiently large dataset, as well as compare the results of the discriminant analysis using data obtained from different laboratories using different analytical procedures (e.g., detection limits, standards, calibration methods). The resulting classification functions derived from discriminant analysis are then able to be applied to magnetite with unknown provenance.

As a ground-truth evaluation of magnetite as an indicator mineral for porphyry mineralization, the classification functions were applied to magnetite grains in till to determine if hydrothermal magnetite from the Mount Polley deposit can be successfully identified. Additionally, discriminant diagrams previously proposed in the literature were also used as a comparison of discrimination methods. Important considerations were

whether a geochemical anomaly (sediment dispersal train) is produced that is distinct from background values, and to what extent does the anomaly coincide with the ice-flow direction relative to the source of mineralization.

2. Geological Setting

2.1 Location and Physiography

The Mount Polley porphyry Cu-Au deposit is located 56 km northeast of Williams Lake and 8 km southwest of Likely, British Columbia, at latitude 52°33'N and longitude 121°38'W (Fig. 1). The deposit occurs near the eastern margin of the Fraser Plateau, a subdivision of the Interior Plateau, which is characterized by low to moderate relief and rolling topography. The Fraser Plateau is bordered by the Quesnel Highlands, followed by the Cariboo Mountain Range to the east. Mount Polley is situated on a topographic high (1266 masl) that separates Polley and Bootjack Lakes. There is significant overburden in the study area, with bedrock exposure mainly confined to steep slopes and road cuts.

2.2 Regional Geology

The Mount Polley deposit occurs in the Quesnel Terrane of the Intermontane Belt, which comprises Late Triassic to Early Jurassic volcanic arc rocks that were accreted to the continental margin of ancestral North America during the late Early Jurassic (Rees, 2013; Fig. 1). Quesnellia is fault-bounded and juxtaposed to the east by Paleozoic to Mesozoic rocks of the pericratonic Kootenay Terrane, and to the west by coeval oceanic rocks of the Cache Creek Terrane that has been interpreted as a subduction accretionary complex (Logan & Mihalynuk, 2005). Late Paleozoic ocean floor rocks assigned to the Slide Mountain Terrane is locally exposed along the eastern margin of Quesnellia (Rees, 2013).

The Mount Polley deposit was emplaced in metasedimentary and basalt to andesitic volcanic arc rocks of the Triassic Nicola Group that now form an open northwest-plunging syncline in the study area (Fig. 2; Logan & Mihalynuk, 2005; Rees, 2013). Detailed lithological descriptions of local stratigraphy is given by Logan & Mihalynuk (2005) and summarized below. The Nicola Group is subdivided into a lower metasedimentary unit that comprises a 2.5 to 4 km thick sequence of siltstones, sandstones and argillites which grade upwards into basal units of the upper volcanic-arc assemblage. The upper assemblage ranges from 5 to 6.5 km in thickness and predominantly consists of subaqueous pyroxene±olivine-phyric basalt and basaltic andesite flows, breccias and subvolcanic intrusions that become analcime-bearing upwards in the stratigraphic sequence. The uppermost units of the Nicola Group include limestone, conglomerate, lahar-tuffite and quartz-phyric dacite as the arc gradually changed from subaqueous to shallow-water then to subaerial deposition (Rees, 2013). The youngest rocks in the study area are predominantly sedimentary, with minor Tertiary volcanic rocks of the Kamloops and Chilcotin Groups (Fig. 2).

2.3 Deposit Geology

The Mount Polley intrusive complex hosting the deposit is a high-level, north-northwest trending, silica-undersaturated, alkalic composite stock, approximately 4 by 6 km in size (Rees, 2013). The intrusive complex is predominantly composed of fine-grained porphyritic diorite and monzonite with subordinate plagioclase porphyry and syenite dikes (Logan & Mihalynuk, 2005). The complex is interpreted to have formed during the later

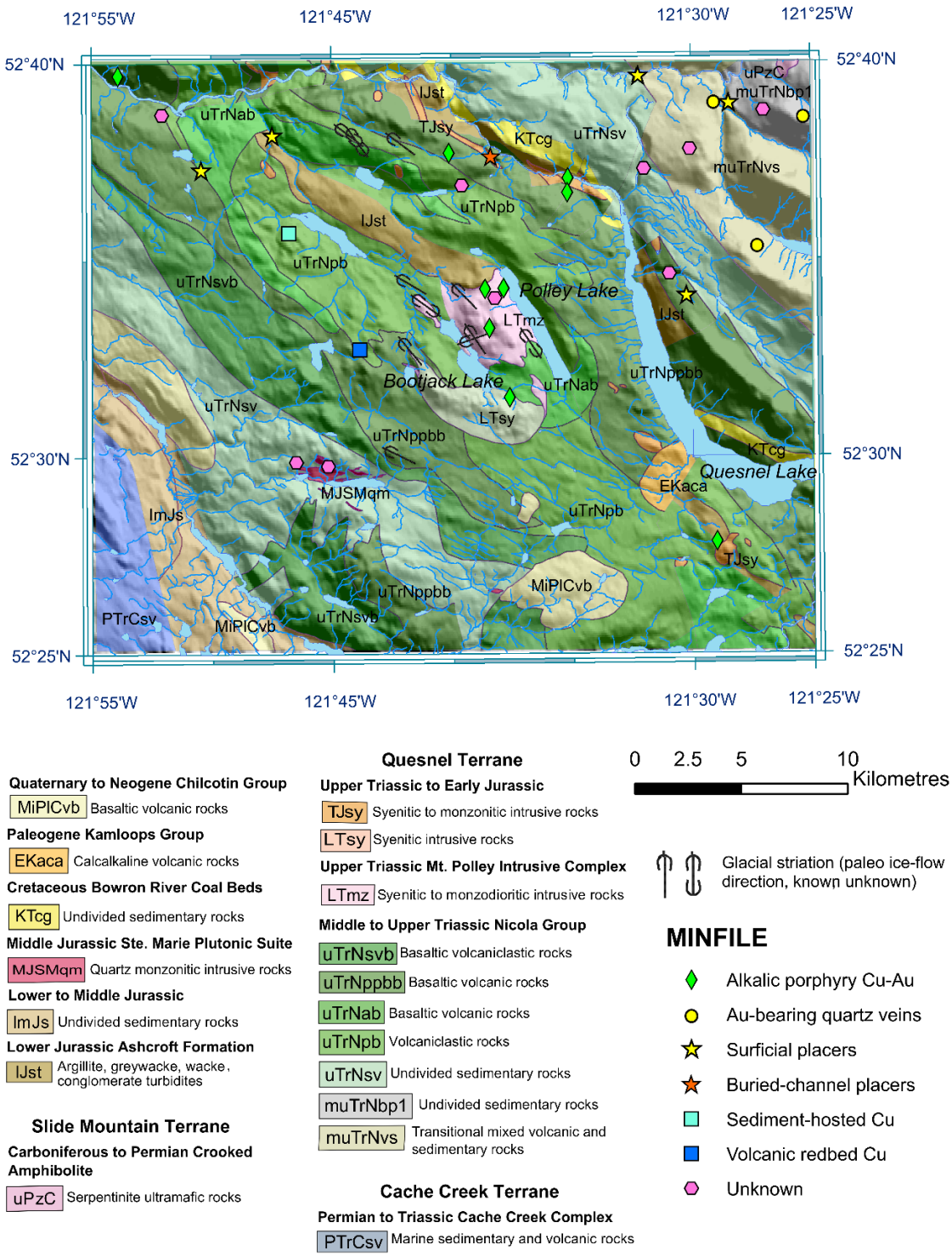

Figure 2. Regional geology and mineral occurrences in the Mount Polley study area (modified from Plouffe et al., 2013a; bedrock geology from Logan et al., 2010). A detailed map of deposit geology is provided by Rees (2013) through a compilation of surface mapping and drill core data.

stage of arc uplift (Rees, 2013) with crystallization ages of the intrusions estimated at ~205 Ma using U-Pb zircon ages (Mortensen et al., 1995; Logan et al., 2007).

The Bootjack stock is a strongly silica-undersaturated nepheline syenite intrusion that also occurs in the study area ~2 km south of Mount Polley. Despite the similar age and close proximity, the Bootjack stock is not related to the Mount Polley intrusive complex and is not associated with significant alteration or mineralization (Bath & Logan, 2006).

Intrusion and hydrothermal breccias at Mount Polley are the major host for Cu-Au mineralization. Intrusion breccias are characterized by an igneous matrix of plagioclase porphyry or quartz syenite, with matrix-supported clasts of monzonite to diorite country rock (Logan & Mihalynuk, 2005). Hydrothermal breccias are heterolithic, with a porous and vuggy matrix that is predominantly composed of biotite, actinolite, albite or magnetite (Fraser, 1994).

Alteration at Mount Polley is concentrically zoned and summarized below from Fraser (1994). Calc-potassic alteration is dominant at the core of the complex and coincides with Cu-Au (-Ag) mineralization (Fraser et al., 1992; Rees, 2013). This type of alteration is separated into three distinct subtypes: biotite, actinolite, and potassium feldspar-albite zones. Other characteristic minerals of calc-potassic alteration include magnetite and diopside, as well as andradite garnet in the northern part of the complex (Rees, 2013). The core is surrounded by a discontinuous garnet-epidote zone with minor chlorite, zeolites and pyrite, followed by an outer propylitic halo of epidote, pyrite and albite. An extensive pyrite zone also occurs northeast of the deposit.

Several major faults separate and truncate the deposit into distinct zones. For example, the prominent, north-trending, east-dipping Polley Fault separates the core of the

intrusive complex into the Central and West zones (Logan & Mihalynuk, 2005). The Central zone is characterized by biotite and actinolite subtypes of calc-potassic alteration, whereas the West zone is characterized by potassium feldspar-albite (Logan & Mihalynuk, 2005). These two zones host the bulk of the mineralization at Mount Polley as low-grade, disseminated and stockwork chalcopyrite, pyrite and lesser bornite (Rees, 2013). Native Au occurs as minute inclusions in chalcopyrite and pyrite (Logan & Mihalynuk, 2005; Rees, 2013). Mineralization is typically associated with magnetite, which correlates well with Cu and Au grades (Fraser et al., 1992; Rees, 2013). Secondary copper minerals related to supergene weathering including covellite, chalcocite, malachite, azurite and chrysocolla are minor and not significantly enriched at the deposit (Rees, 2013).

Mineralization in the northern portion of the Mount Polley intrusive complex (north of the east-west Green Giant Fault) includes the Northeast and Boundary zones. These zones are characterized by high-grade chalcopyrite, bornite and lesser pyrite concentrated mainly as breccia cement and stockwork veining (Logan & Mihalynuk, 2005; Rees, 2013). In addition to gold, silver is also abundant in the Northeast zone and both metals correlate well with copper (Rees, 2013). In contrast to the Central and West zones, magnetite is not directly associated with the mineralization in the northern part of the complex due to magnetite replacement by Cu-sulphides (Rees, 2013). The age of mineralization at Mount Polley was determined by Logan et al. (2007) as 205.2 ± 1.2 Ma using $^{40}Ar/^{39}Ar$ in hydrothermal biotite intergrown with chalcopyrite from the Northeast zone.

The smaller Southeast and Pond zones occur in the southern part of the complex near the contact with Nicola group volcanic rocks. Mineralization typically includes chalcopyrite and pyrite, as well as molybdenite in the southern part of the Southeast zone

(Rees, 2013). The Pond zone, which is characterized by andradite garnet-epidote skarn-type alteration, also contains rare bornite and high silver concentrations (Rees, 2013).

2.4 Glacial History

The Late Wisconsinan Fraser Glaciation deposited a thick blanket of glacial sediment in the Quesnel Terrane and much of the Interior Plateau. Ice build-up of the Cordilleran Ice Sheet began ~29 ka, with complete deglaciation occurring by ~11.5 ka (Ryder et al., 1991). Ice-flow indicators as measured from erosional features on outcrop indicate two directions of ice-flow movement: 1) early westward ice-flow (oriented at 250-275°) during advancement of valley and piedmont glaciers from the Cariboo Mountains; and 2) later north-westward ice-flow (oriented at 290-330°) during glacial maximum, which was caused by an ice divide to the south of Mount Polley at 52°N latitude (Plouffe et al., 2013a; Hashmi, 2015). The NW-trending direction is the dominant ice-flow movement recorded in the study area (Hashmi, 2015).

3. Methodology

3.1 Till Sampling Survey

The Geological Survey of Canada and the BC Geological Survey conducted a till sampling survey between 2011 and 2013 in the region surrounding the Mount Polley deposit as part of the Natural Resources of Canada's Targeted Geoscience Initiative 4 (TGI-4) program (Anderson et al., 2012; Plouffe et al., 2013b; Ferbey et al., 2014). A total of 74 till samples, covering an area of ~700 km^2, were the basis for this study (Fig. 3; Appendix A). Mineralized rocks were also sampled from areas exposed to glaciation. The composition of hydrothermal magnetite from some of these samples in the Mount Polley deposit were investigated by Canil et al. (in press).

3.2 Sample Preparation

For each sampling location, ~10 kg of till was collected at an average depth of 80 cm below the soil weathering horizon. Bulk till samples, processed by Overburden Drilling Management Limited (Nepean, Canada), were first wet sieved to a <2 mm size fraction and concentrated by density on a shaking table. The heavy minerals recovered were further concentrated in heavy liquids (methylene iodide) and sieved into three size fractions: 1-2 mm, 0.5-1 mm and 0.25-0.5 mm. Magnetic separation was performed on the 0.25-0.5 mm heavy mineral fraction of the processed till samples. Magnetite grains were picked from the ferromagnetic heavy mineral fraction using a hand magnet and binocular microscope at the University of Victoria (Victoria, Canada) and approximately 100-125 grains per till sample were randomly selected, mounted in epoxy and polished for analysis (Fig. 4).

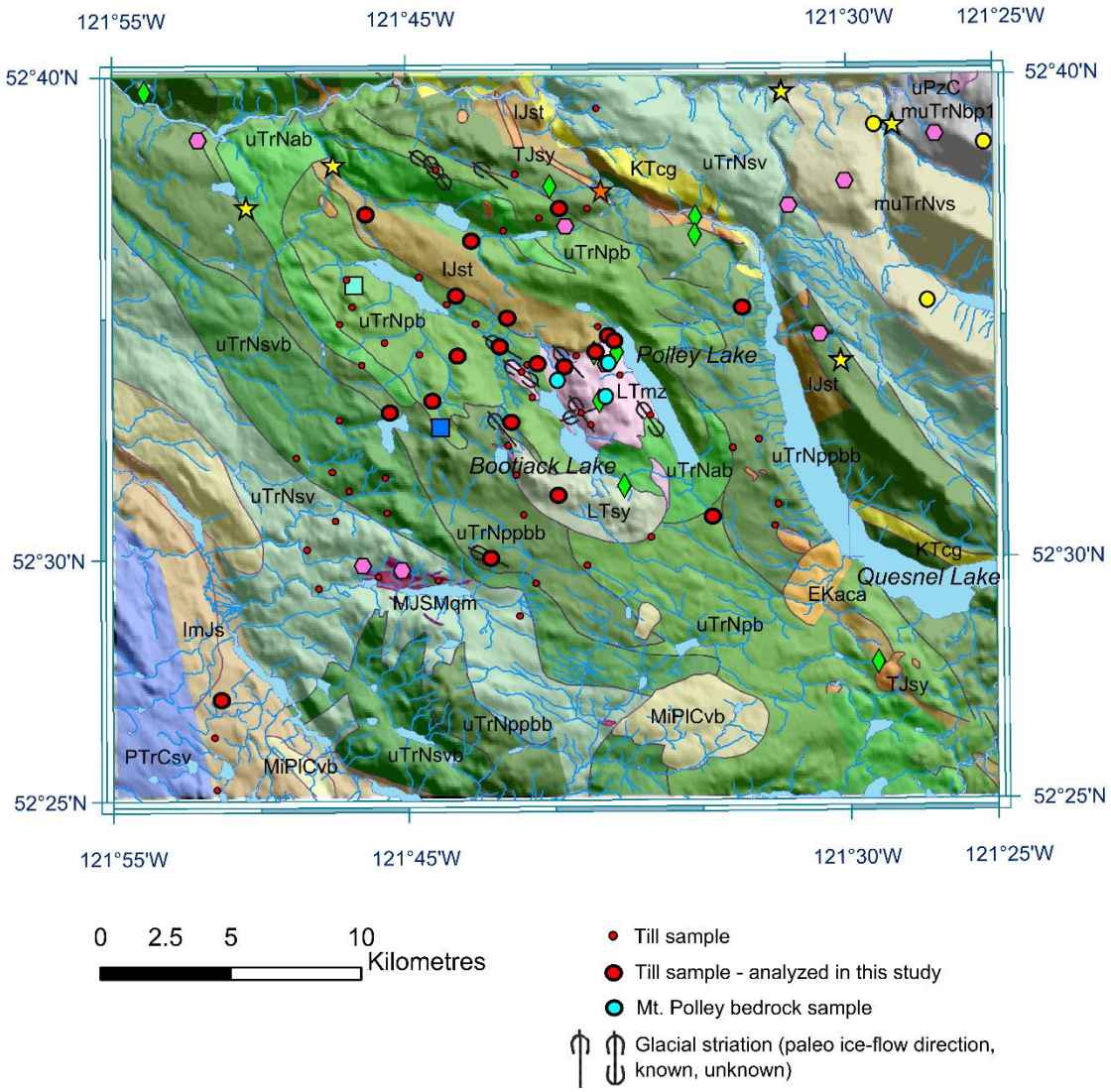

Figure 3. Till sampling locations in the Mount Polley study area (red dot). Samples analyzed in this study are indicated as larger symbols. Locations for Mount Polley bedrock samples are also shown (blue dot). Modified from Plouffe et al. (2013a). Bedrock geology from Logan et al. (2010) – legend in Figure 2.

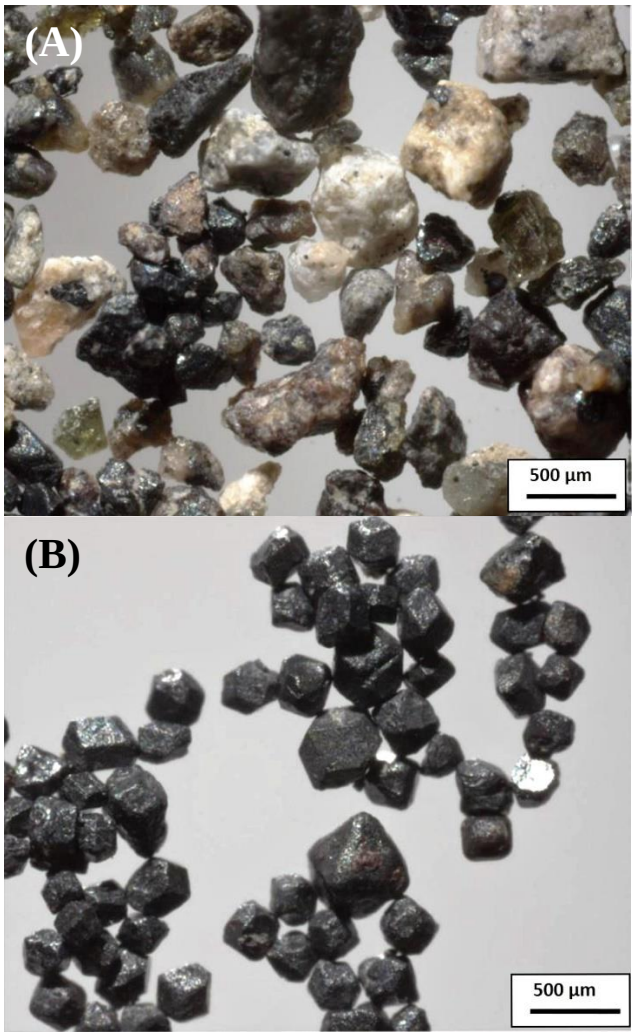

Figure 4. A) Initial magnetic fraction of heavy mineral concentrates from till (sample 12 PMA 586 A01); B) Magnetite grain selection following sample refinement.

3.3 Petrography

Reflected light microscopy was used to examine internal textures of the magnetite. Magnetite grains were classified according to their crystal form, quality (e.g., intensity of pitting or fracturing), exsolution textures, alteration and abundance of mineral inclusions (Appendix B). Magnetite grains with appreciable alteration, fracturing or with a significant number of inclusions were excluded because they would not be amenable to further microanalysis.

A subset of magnetite grains in each sample was further examined with a Hitachi S-4800 field emission scanning electron microscope (SEM) at the University of Victoria using an accelerating voltage of 16 kV and emission current of 20 nA. Textures were documented using back-scattered electron (BSE) imaging. Identification of exsolution and alteration phases, as well as mineral inclusions, was performed using semi-quantitative energy dispersive x-ray spectrometry (EDS).

3.4 Electron Microprobe Analysis

The concentrations of Mg, Al, Si, Ca, Ti, V, Cr, Mn, Fe and Ni in magnetite from a subset of till samples were determined using a CAMECA SX 50 electron microprobe (EMP) at the University of British Columbia (Vancouver, Canada). The EMP was operated at an accelerating voltage of 15 kV, beam current of 20 nA and spot size of 5 μm. Counting times of 20 sec was used for all elements except 40 sec count times was used for V, Cr and Ni. For nearly all elements, less than 5% of analyses were below the detection limits of the EMP, except Cr and Ni for which ~30% of analyses were below detection. Detection limits for the EMP are given in Appendix C.

3.5 Laser Ablation-Inductively Coupled Plasma-Mass Spectrometry

Fifty magnetite grains per till sample were randomly selected for elemental analysis by laser ablation-inductively coupled plasma-mass spectrometry (LA-ICP-MS) at the University of Victoria, Canada (Appendix B). Analysis of Mg, Al, Si, Ca, Sc, Ti, V, Mn, Cr, Co, Ni, Cu, Zn, Ga, Nb, Mo, Sn, Ta and W was performed using a 213 nm Nd: YAG UV laser operating at 50-63% energy and 10 Hz, and interfaced to a Thermo Scientific XSERIES 2 Quadrupole ICP-MS. Spot and raster ablation methods were employed depending on mineral texture and quality, with the beam focused to a spot size of 25-55 μm. Data collection for each analysis included 30 sec of background signal followed by 20 or 30 sec of ablation. External calibration using standard reference material silicate glasses NIST611, NIST613 and NIST615 was performed for every 10 analyses. Matrix-matched standards are not required for magnetite as demonstrated by Nadoll & Koenig (2011) who obtained reliable results using NIST 610 for calibration at spot sizes greater than 25 μm. Time-resolved spectra were processed off-line using a custom spreadsheet. Obvious heterogeneities in time resolved spectra (e.g., by inclusions) were edited to remove contaminated sections from the spectra if possible, or were discarded.

Three different methods of standardization were employed: 1) internal standardization using an assumed stoichiometric amount of Fe in pure Fe_3O_4 magnetite (i.e., 72 wt.% Fe); 2) internal standardization using the Fe concentration as determined by EMP analysis; and 3) the ablation yield correction factor (AYCF) method of Liu et al. (2008), an internal standard-independent calibration that corrects for the absolute amount of material ablated and calibrates to the total counts per second for each analysis. A comparison of the three different calibration methods is discussed in a subsequent section.

Accuracy and precision was monitored over time in each analytical session using the USGS basaltic glass reference BCR2g (Appendix D). Accuracy for elements Mg, Si, Ca, Sc, Ti, V, Mn, Co, Ni, Nb, Mo and W is better than 5%. Elements Cr, Fe and Ta have accuracies between 5 and 10%; Al, Cu and Sn between 10 and 20%; and Zn and Ga are the lowest at 20-30%. Precision was better than 20% for all elements except Cr, Zn, Ga and W. Detection limits are calculated using the 3σ criterion, whereby the limit of detection for each element is calculated using three times the standard deviation of the gas background signal that contains zero analyte (Longerich et al., 1996). A summary of detection limits, accuracy and precision values are given in Table 1.

Table 1. Detection limits, accuracy and precision for magnetite LA-ICP-MS analysis.

Element	Isotope	DL, min (ppm)	DL, max (ppm)	DL, med (ppm)	Accuracy (%)	Precision (%)
Mg	26	2.13	92	6.53	5	13
Al	27	0.53	121	6.23	13	11
Si	29	123	42820	380	1	6
Ca	42	81	899	160	5	5
Sc	45	0.03	3.49	0.41	3	15
Ti	47	0.45	691	4.23	2	13
V	51	0.08	32	0.52	5	15
Cr	52	0.71	109	1.76	9	22
Mn	55	0.3	61	0.9	3	15
Fe	57	11	3546	76	8	14
Co	59	0.02	1.17	0.13	4	15
Ni	60	0.1	6.08	1.63	4	17
Cu	63	0.08	3.85	0.54	14	15
Zn	66	0.12	28	0.4	22	21
Ga	69	0.01	1.5	0.07	29	30
Nb	93	0.003	0.91	0.05	2	12
Mo	95	0.02	1.17	0.12	2	14
Sn	118	0.04	0.88	0.08	15	14
Ta	181	0.001	0.94	0.01	10	17
W	182	0.004	1.49	0.04	1	26

Accuracy and precision calculated based on analysis of BCR2g. Abbreviations: min – minimum, max – maximum, med – median.

4. Petrography

Magnetite grains in till exhibit a wide variety of morphologies, textures, alteration and inclusions (Fig. 5). As an isometric mineral, magnetite typically forms octahedral and dodecahedral crystal forms, and granular or massive aggregates. In the till samples, magnetite grains vary in shape from subhedral-euhedral octahedrons and cubo-octahedrons, to more commonly rounded to sub-rounded forms, which likely result from sediment transport. Some magnetite grains are highly fractured or strongly pitted, whereas others are relatively pristine or homogeneous (Fig. 5A).

In reflected light, polished magnetite surfaces are typically gray with brownish tint, but is often characterized by exsolution of a slightly less reflective phase. Exsolved phases of ilmenite ($FeTiO_3$) or, very rarely, ulvöspinel (Fe_2TiO_4) +/- rutile (TiO_2) typically occur as trellis-type lamellae ranging from submicroscopic to 10 μm in width (Figs. 5, 6). Parallel or sandwich-type lamellae are also observed, but are much less common. Some magnetite grains contain more than one exsolution phase. For example, Figure 6A shows thick ulvöspinel + rutile lamellae with thin interstitial trellis replaced by an unknown secondary Si-Al-Mg phase in magnetite. Ilmenite exsolution occurs by subsolidus oxidation during cooling, whereas ulvöspinel exsolution occurs from cooling alone below 600°C (Haggerty, 1991).

There are two predominant types of alteration present in magnetite from till: 1) martitization due to oxidation, and 2) ‘sphenitization’ by late stage fluids (Haggerty, 1976). Hematite alteration of magnetite (martitization) predominantly occurs along grain boundaries, crystallographic planes (lamellae), adjacent to fractures, or as localized patches, and exhibits no preference for any specific textural or morphological type of

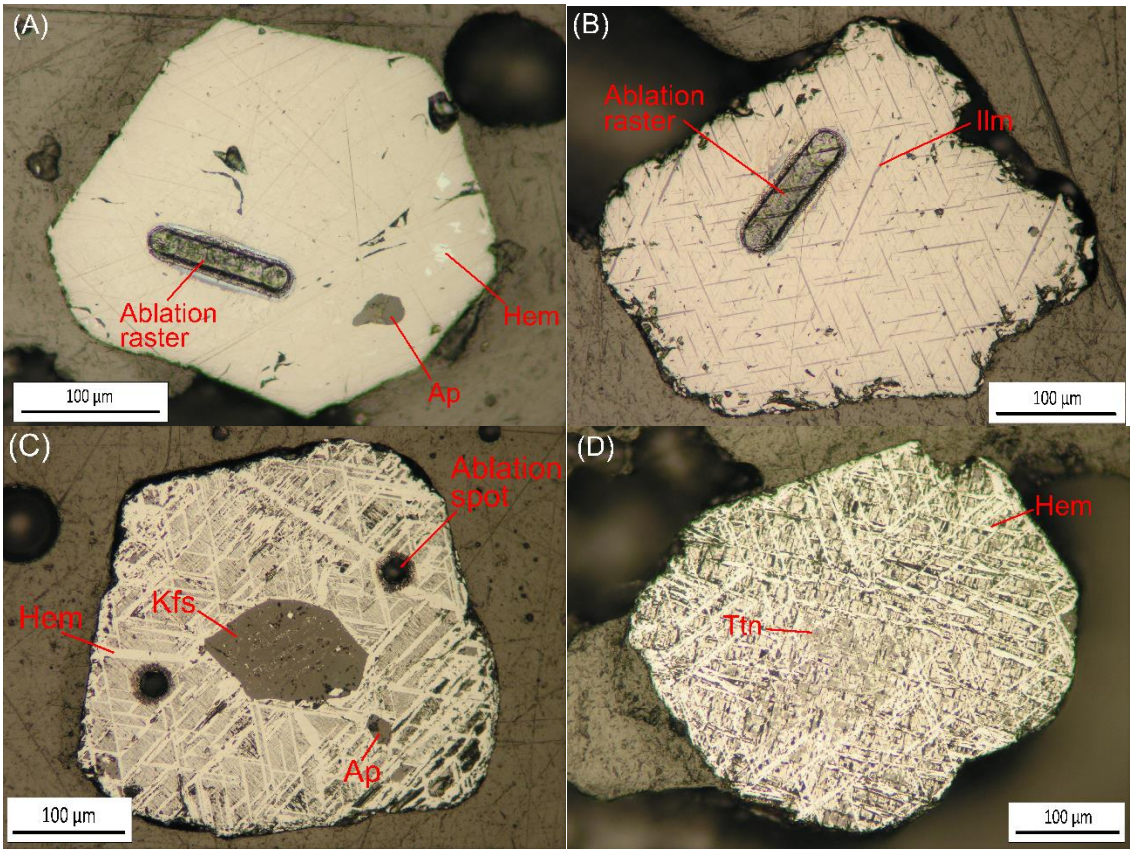

Figure 5. Petrographic varieties of magnetite from till in reflected light at 20 times magnification. A) Euhedral, homogeneous magnetite grain with 100 µm long laser-ablation raster, apatite (Ap) inclusion and minor hematite (Hem) alteration patches (sample 12 PMA 081 A01-C3). B) Subhedral magnetite grain with ilmenite (Ilm) trellis lamellae and 110 µm long laser-ablation raster (12 PMA 077 A01-D1). C) Subhedral magnetite grain with very fine trellis lamellae, potassium feldspar (Kfs) and apatite inclusions, hematite alteration, and two 30 µm laser-ablation spots (12 PMA 088 A01-D4). D) Subrounded, heterogeneous magnetite grain with fine trellis lamellae, hematite alteration, as well as blebby titanite (Ttn) predominantly concentrated in the core (12 PMA 087 A01-G6).

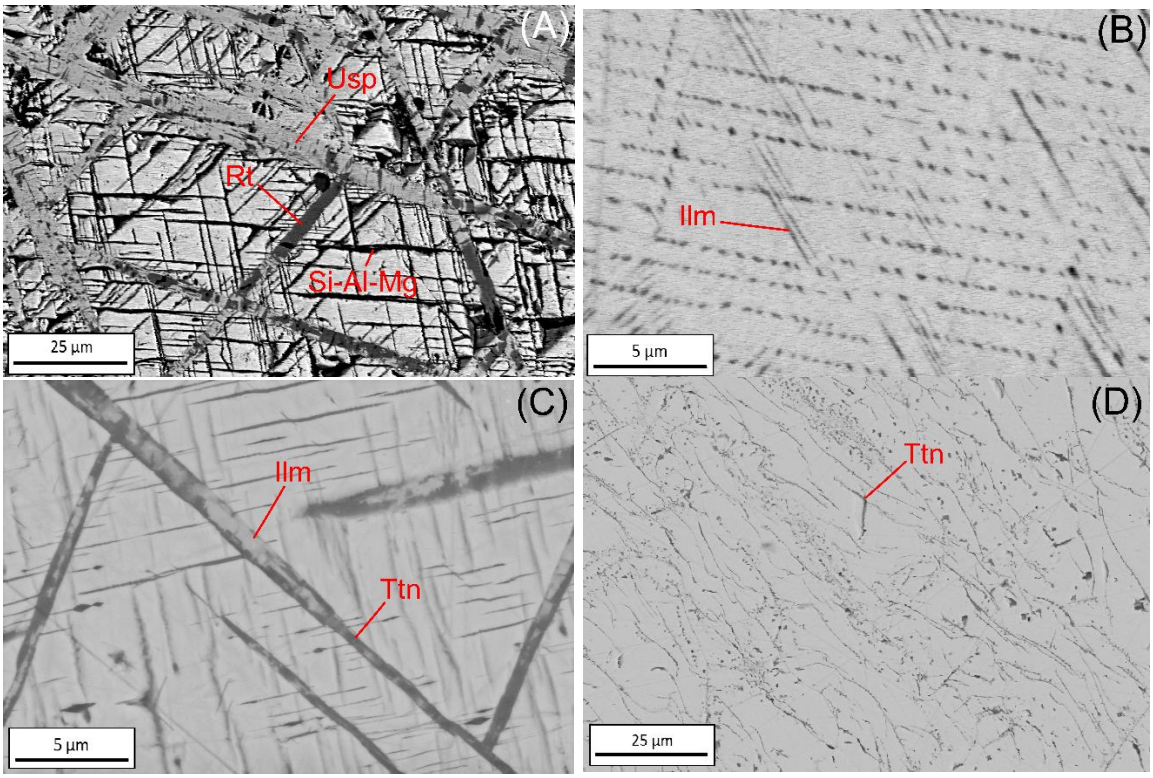

Figure 6. Back-scattered electron (BSE) images of magnetite. A) Coarse ulvöspinel (Usp) and rutile (Rt) lamellae with an interstitial, fine, dark trellis lamellae of a Si-Al-Mg-rich phase (sample 12 PMA 095 A01-C11). B) Submicroscopic ilmenite (Ilm) lamellae in magnetite (12 PMA 095 A01-A15). C) Preferential titanite (Ttn) alteration of ilmenite lamellae in magnetite (12 PMA 585 A01-F4). D) Stringers and disseminations of titanite in magnetite (12 PMA 088 A01-B15).

magnetite (Fig. 5). This alteration is easily identified in reflected light, whereas alteration of magnetite to titanite (sphenitization) is highly variable and cryptic in comparison. In exsolved magnetite grains titanite is commonly observed as a preferential replacement product of Ti-rich lamellae (Fig. 6C) indicating that its formation postdates oxidation-exsolution, whereas in magnetite grains without exsolution, titanite is commonly observed as irregular stringers or fine disseminations (Figs. 6D). In addition, titanite may form along grain boundaries or as localized patches (Fig. 5D), similar to hematite.

Mineral inclusions may be present and/or abundant in some magnetite grains (Figs. 5A, C). Apatite is the most common type of inclusion followed by quartz, potassium feldspar and chalcopyrite in decreasing abundance.

5. Chemistry

5.1 Comparison of Analytical Methods

Quantitative LA-ICP-MS analysis typically uses the concentration of a major element in the unknown as an internal standard to which to normalize the ablation yield (or count rate) of all other elements (Longerich et al., 1996). The internal standard must be in sufficient concentrations and is typically determined by another analytical method. This study employed three calibration methods for the reduction of magnetite LA-ICP-MS spectra. The 'EMP Fe' calibration method uses the Fe concentration in magnetite as determined by EMP as the internal standard. To obviate the step of obtaining EMP data, the 'stoichiometric Fe' calibration method assumes the maximum stoichiometric amount of Fe that can occur in magnetite and, therefore, is an approximation that produces the maximum possible trace element concentrations. The third type of calibration, the ablation yield correction factor (AYCF) method, is an internal standard-independent strategy that calibrates to the total counts per second in each analysis assuming that all elements in the sample have been analyzed (Liu et al., 2008). For magnetite, the suite of elements selected for LA-ICP-MS analysis covers the range of known elemental substitutions in magnetite that occur in measurable concentrations and, therefore, safely satisfies this assumption. The AYCF equation of Liu et al. (2008) is modified to normalize magnetite data to 72 wt. %, the sum of all cation concentrations in stoichiometric magnetite, using the following equation:

$$AYCF = \frac{72}{\sum_{j=1}^{N}\left(cps_{sam}^{j} * l^{j}\right)} \tag{2}$$

where, cps_{sam}^{j} is the count rate for element j in the sample, and l^{j} is the slope of the calibration curve (ppm/cps) for element j using the standard reference materials. In comparison, the cation sum for pure end-member Fe_2TiO_4, which is commonly in solid solution with magnetite, is 71 wt. %. Therefore, it can be assumed that minor elemental substitution in magnetite would produce negligible differences in trace element concentrations when normalized to the cation sum of pure stoichiometric magnetite.

For all major and minor elements in magnetite, the 'stoichiometric Fe' calibration method produced consistently higher concentrations than the 'EMP Fe' method (Figs. 7A, 8A). On average, the 'stoichiometric Fe' calibration produces element concentrations approximately 13% higher, to a maximum of 35%. In contrast, the AYCF method produces element concentrations on average within only a few percent of that calculated using the 'EMP Fe' calibration method (Figs. 7B, 8B). For each analysis, with the exception of Cu and Zn, the maximum difference observed between AYCF and 'EMP Fe' methods is 20-25%. The low mass elements Mg, Al, Si and Ca cannot be compared between calibration methods because spurious concentrations arise from calibration with Fe as an internal standard. This effect could potentially be related to the low concentration of Fe in the NIST reference materials to which the data is calibrated. On the other hand, the calibration curves for Mg, Al, Si and Ca using the internal standardless AYCF method are well defined and considered reliable. Thus, the AYCF method is preferred over either internal standardization calibration methods by providing accurate calibration of all elements in magnetite while eliminating the time for an additional analytical step in determining the concentration of the internal standard.

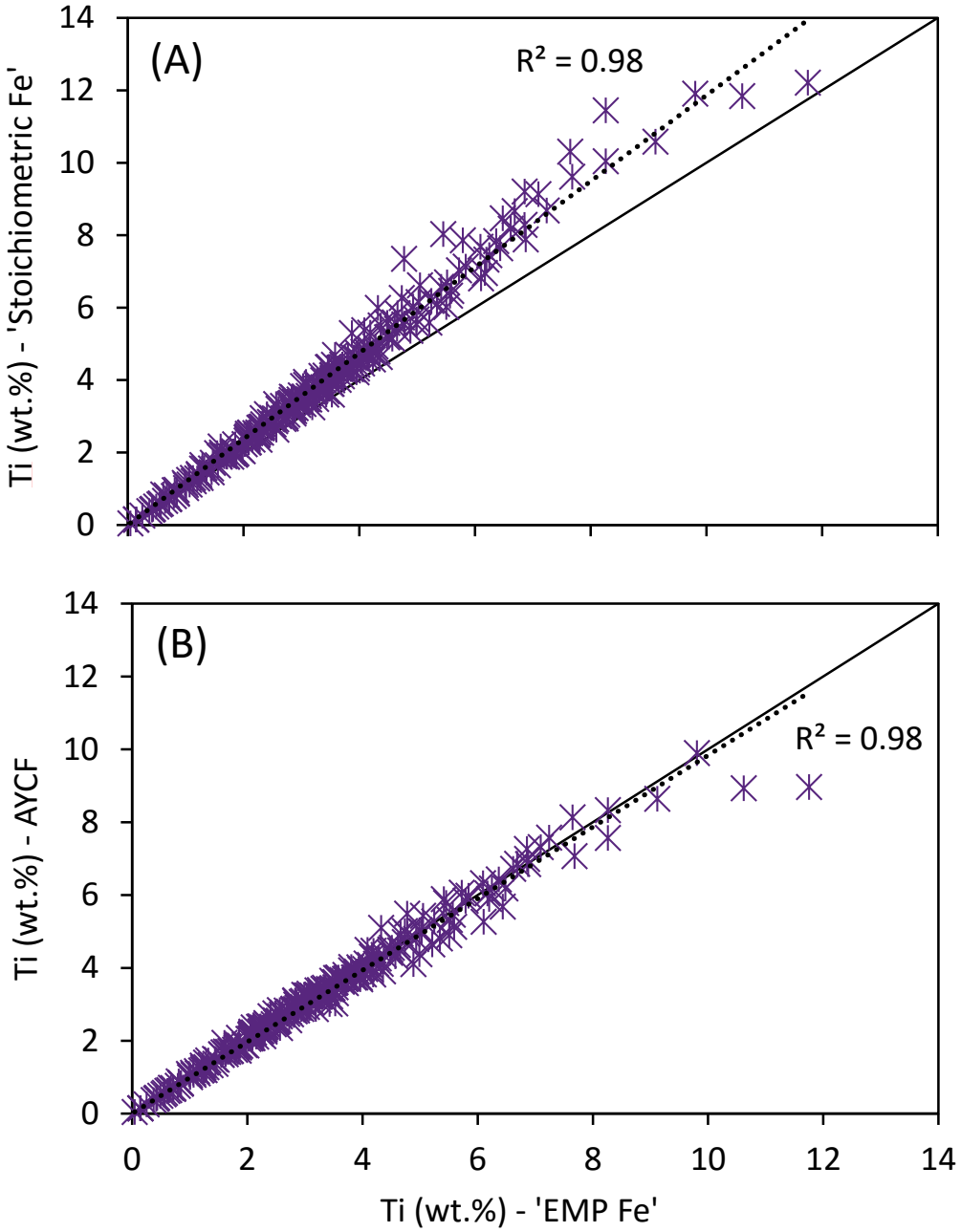

Figure 7. A comparison of LA-ICP-MS calibration methods using Ti concentrations in magnetite as a representative example of calibration for a major element. A 1:1 reference line (solid black) and data trendline (dotted) are shown. Good correlation of data (R^2 = 0.98) is observed between calibration methods, however, calibration by the 'stoichiometric Fe' method consistently produces the highest element values (A). Element concentrations determined by AYCF calibration closely approximates the 'EMP Fe' method as illustrated by the close proximity of data to the 1:1 reference line (B).

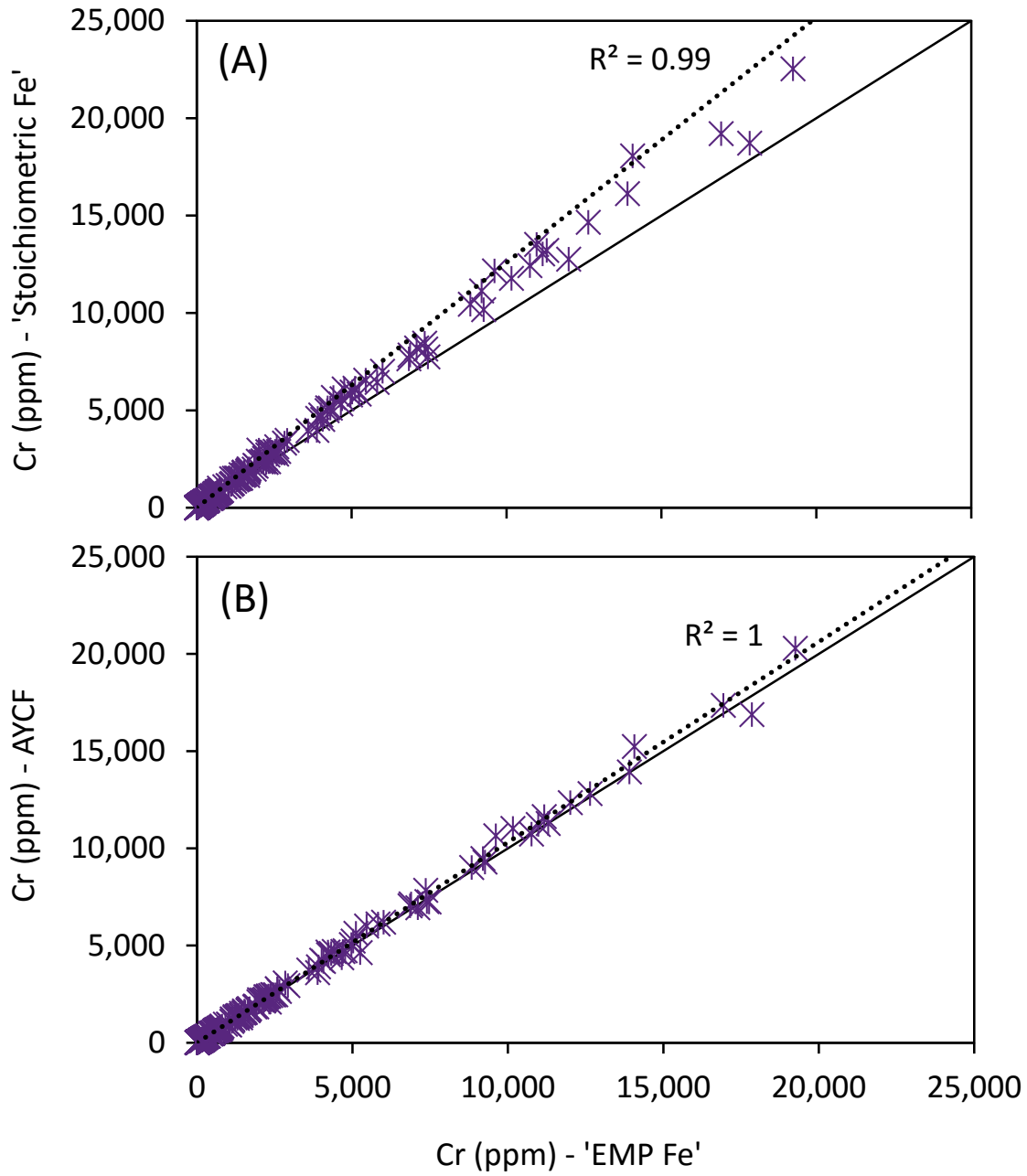

Figure 8. A comparison of LA-ICP-MS calibration methods using Cr concentrations in magnetite as a representative example of calibration for a trace element. A 1:1 reference line (solid black) and data trendline (dotted) are shown. Good correlation of data (R^2 > 0.99) is observed between calibration methods, however, calibration by the 'stoichiometric Fe' method consistently produces the highest element values (A). Element concentrations determined by AYCF calibration closely approximates the 'EMP Fe' method as illustrated by the close proximity of data to the 1:1 reference line (B).

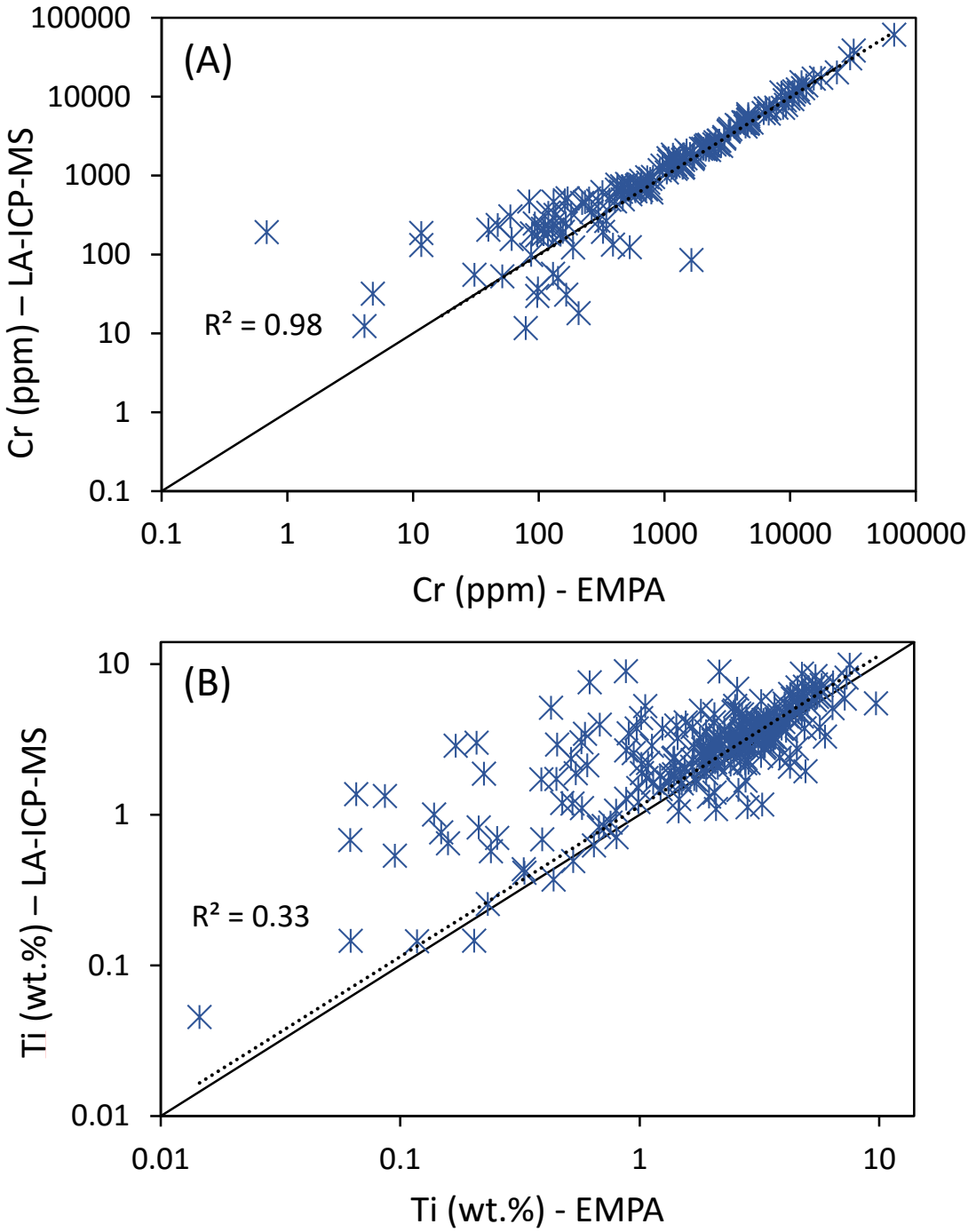

Figure 9. A comparison of LA-ICP-MS and EMP analytical methods for magnetite. A) Good correlation is observed for Cr between the two techniques, however, the EMP performs poorly when close to the detection limit as indicated by data scatter below ~1000 ppm. B) Significant scatter is present in Ti between the two techniques, likely the result of discrepancies between the techniques caused by the small EMP beam size unable to homogenize exsolution lamellae with host magnetite.

Elements such as Mg, Al, Ti, V, Cr and Mn occur in significant concentrations in magnetite and are often detectable by both EMP and LA-ICP-MS. Other elements that occur in much lower concentrations (<0.1 wt.%) such as Si, Ca, Cr and Ni, however, are often near or below detection for the EMP (Fig. 9A). Significant scatter observed for certain elements may be an artifact of the difference in beam size between the EMP and LA-ICP-MS (Fig. 9B). For example, extensive exsolution is observed in a large proportion of the magnetite grains in this study (Figs. 5, 6) and the lamellae are often at scales coarser than the size of the electron beam. The smaller electron beam of EMP is less able to homogenize entire bulk composition signal during analysis in this case. This difference in sampling would contribute significantly to differences in concentrations for elements that are heterogeneously distributed in magnetite, such as Ti which can be concentrated in exsolution lamellae. A larger beam size is possible for EMP, however, the rastering capability of the laser is most efficient for homogenizing material during analysis. Preference is given to element concentrations determined by LA-ICP-MS analysis rather than EMP based on the greater sensitivity and lower detection limits of the former instrument and the fact that the laser spot size (25-55 μm) homogenizes more of the crystal during analysis and is, therefore, a better representation of the total primary magnetite composition before exsolution processes.

5.2 “Sphenitization”: High Si and Ca in Magnetite

A large proportion of magnetite grains from till are characterized by elevated concentrations of Si and Ca up to 7.3 and 6.0 wt.%, respectively. Both Si and Ca are typically incompatible elements in spinel group minerals from the Earth’s crust. A number

of studies have documented several weight percent Si in magnetite from various environments with Ca concentrations, if measured, typically less than 1 wt.%. (Vincent & Phillips, 1954; Shcheka et al., 1977; Newberry et al., 1982; Shiga, 1988; Westendorp et al., 1991; Dare et al., 2014). Some studies suggest that high Si contents are likely attributed to a Fe_2SiO_4-equivalent spinel component in solid solution with magnetite rather than contamination by minute silicate impurities (e.g., Newberry et al., 1982; Westendorp et al., 1991). Alternatively, Shcheka et al. (1977) suggested variable amounts of a Ca_2SiO_4 spinel component in magnetite based on similarly high Ca contents. The majority of Si-bearing magnetite in the aforementioned studies is described as zoned or containing discrete domains for which Si is concentrated, features that have not been observed in magnetite from till.

The majority of magnetite grains in till that are enriched in Si and Ca are characterized by approximately equal atomic proportions of these two elements (Fig. 10). This is not consistent with substitution of a Ca_2SiO_4 spinel component, but rather the result of varying degrees of mixing between magnetite and titanite ($CaTiSiO_5$). The 1:1 stoichiometry of Si to Ca in many of the magnetite grains is consistent with sphenitization observed petrographically on a variety of scales (Fig. 5,6). From the Si and Ca contents, the maximum amount of titanite alteration observed in any individual grain is 33%, however, 90% of magnetite grains contain less than 14% titanite and half of all magnetite grains contain less than 2% titanite.

Haggerty (1976) suggests that the sphenitization of magnetite forms by the metasomatic introduction of SiO_2 and CaO by late stage H_2O-rich fluids or by the breakdown of plagioclase, followed by the removal of FeO from magnetite to form other

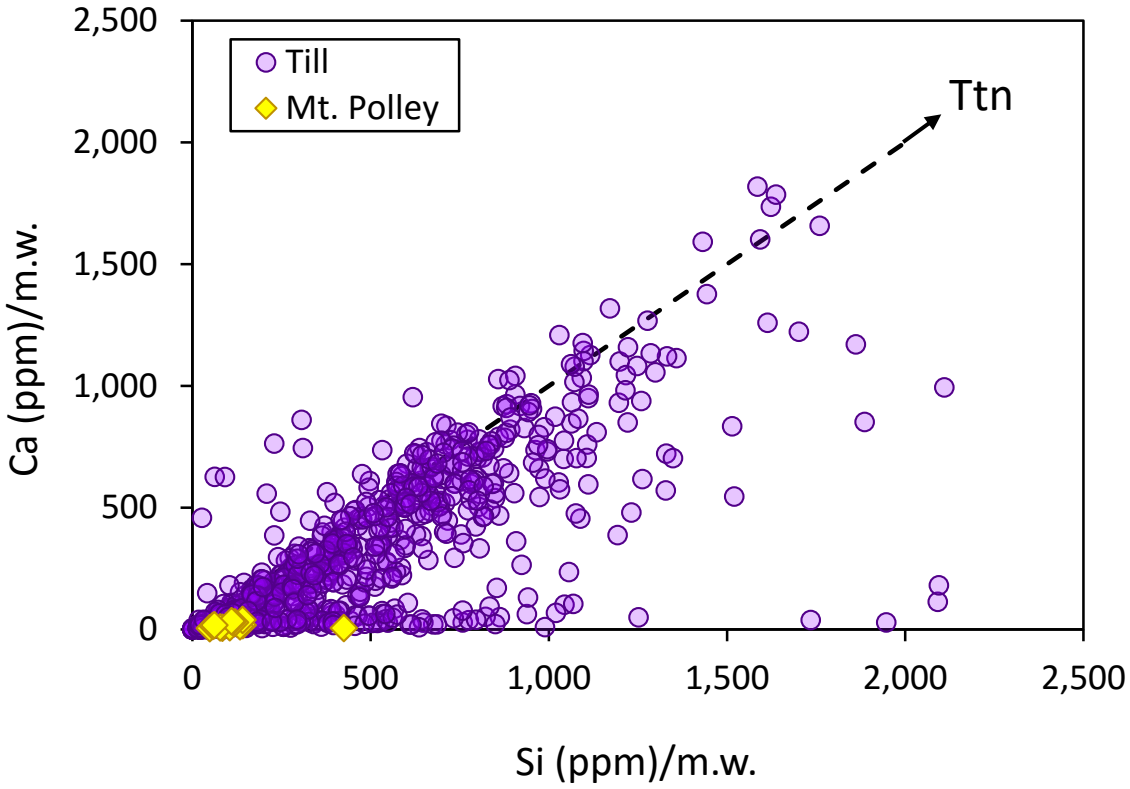

Figure 10. Ca and Si contents in magnetite normalized to their molecular weight to show approximate atomic proportions. A positive 1:1 correlation is consistent with variable mixing of magnetite (at the origin) with titanite (plots off axes). Several magnetite grains from till with high Si and low Ca may indicate potential interference by minute silicate inclusions in these grains, or possible Si in solid solution, but this is not prevalent. Mount Polley magnetite data was obtained from Canil et al. (in press) and re-calibrated using the AYCF method.

minerals in the rock such as sulphide, chlorite or amphibole. This phenomenon has been documented in various igneous and metamorphic rock types such as metasomatized intrusive rocks (Weisse et al., 1985), I- and S-type granites (Whalen & Chappell, 1988) and hydrothermally altered oceanic crust (Shau et al., 2000). Sphenitization is also relatively common during regional, low-grade metamorphism (Haggerty, 1976). Weisse et al. (1985) commonly observed preferential titanite alteration of ilmenite lamellae in magnetite from the Nahant gabbro, United States, similar to that observed in till near Mount Polley (Fig. 6C). Haggerty (1976) documents examples of titanite replacement for both exsolved lamellae and host magnetite.

In porphyry and skarn deposits of the Canadian Cordillera, sphenitization was observed petrographically in very few samples and, when observed, was present in very trace amounts. The chemistry of magnetite from Mount Polley confirms that this is not a characteristic phenomenon since magnetite in the deposit contains, on average, less than 0.3 wt.% Si and 0.05 wt.% Ca, which would correspond to less than 1% titanite if at all present (Fig. 10). In fact, greater degrees of sphenitization in magnetite in till were observed at greater distances down-ice or away from the Mount Polley deposit. Grains with any appreciable amount of sphenitization are interpreted as likely sourced from the various volcanic, subvolcanic and sedimentary rocks of the Nicola Group that dominate the study area rather than being hydrothermal in origin and specific to the Mount Polley porphyry deposit.

5.3 Magnetite Compositional Variability

A large compositional variability is observed in the detrital magnetite grains and reflects the diverse bedrock sources of till. Presumably the majority of magnetite in till is igneous in origin, being derived from Nicola Group volcanic arc rocks that cover most of the study area (Fig. 2). Figure 11 illustrates some major element trends in the dataset, as compared to hydrothermal magnetite from the Mount Polley deposit, as well as other porphyry deposits in the Canadian Cordillera and the southwest United States.

Titanium is the most variable of all elements measured in magnetite, ranging from 50 ppm to 13.5 wt.%, and shows a strong positive correlation with Al, which ranges up to 7.6 wt.% (Fig. 11A). The Ti and Al contents of magnetite are directly related to temperature-dependent solid solutions with Fe_2TiO_4 and $FeAl_2O_4$, respectively (Buddington & Lindsley, 1964; Turnock & Eugster, 1964). Therefore, elevated Ti and Al concentrations in most magnetite grains in till is consistent with a large proportion of material derived from igneous source rock. In contrast, hydrothermal magnetite typically contains substantially lower Ti and Al than magnetite in igneous rocks (Fig. 11A; e.g., Dupuis & Beaudoin, 2011; Dare et al., 2014; Nadoll et al., 2014; Canil et al., in press).

Other major elements that occur in significant concentrations in magnetite grains from till are trivalent V and Cr with maximum concentrations of 0.7 and 8.1 wt.%, respectively. Nadoll et al. (2014) suggested that higher V contents are more typical of magmatic magnetite, however, magnetite at the Mount Polley deposit contains significantly high V compared to most in till (Fig. 11B). Magnetite with elevated Cr concentrations has been documented in serpentinized mafic-ultramafic rocks as ‘ferritchromit’, a product of hydrothermally altered magmatic spinels (e.g., Mellini et al.,

2005). Chromium-rich magnetite is, therefore, likely derived from ultramafic rocks of the Slide Mountain Terrane that occurs immediately east of Quesnellia with serpentinites of the Crooked Amphibolite unit outcropping in the far northeast corner of the study area (Fig. 2).

Divalent Mn, Mg and Zn have maximum concentrations of 6.5, 4.3 and 1.9 wt.%, respectively. Magnesium and Al exhibit a positive correlation in magnetite from till, but this trend is not as apparent in hydrothermal magnetite, which could be partially due to the immobility of Al in hydrothermal fluids compared to Mg (Fig. 11C). In contrast, Mn and Zn are positively correlated for magnetite from both till and porphyry systems (Fig. 11E). Elevated concentrations of Si and Ca are also observed in some grains, but as was shown previously is related to sphenitization and not direct elemental substitution in magnetite (Fig. 10).

Minor elements that are detectable in most magnetite grains include Ni (max. 3021 ppm), Cu (1807 ppm), Co (759 ppm) and Ga (213 ppm). Nickel shows a strong positive correlation with Cr (Fig. 11D). Gallium is generally correlated with Mn and Zn, suggesting minor components of $MnGa_2O_4$ and $ZnGa_2O_4$ (Fig. 11F), however, this trend is not observed in hydrothermal magnetite. Of the trace elements, only Sc and Sn are measurable in nearly all magnetite grains but are less than 77 and 12 ppm, respectively. More than 10% of all analyses were below detection for Nb, Mo, Ta and W for which the maximum contents of each element is less than ~150 ppm. Tin concentrations in hydrothermal magnetite are positively correlated with Mo and Sc, however, the same relationship between Sn and Sc is not observed in magnetite from till (Figs. 11G, H).

Figure 11 (next page). Select binary plots showing the variation in magnetite chemistry from till. Magnetite data from Canil et al. (in press) for Mount Polley and other porphyry deposits in British Columbia were re-calibrated using the AYCF method. Magnetite data from porphyry deposits in the southwest United States is from Nadoll et al. (2015). Positive correlations are exhibited between elements on all binary plots, with the following notable exceptions: B) Mount Polley tends to higher V contents compared to all other porphyry deposits, as well as most magnetite in till; C,F) The Mg-Al and Ga-Mn relationships in magnetite from till is not apparent in hydrothermal magnetite; and H) The Sc-Sn correlation in hydrothermal magnetite is not observed in magnetite from till.

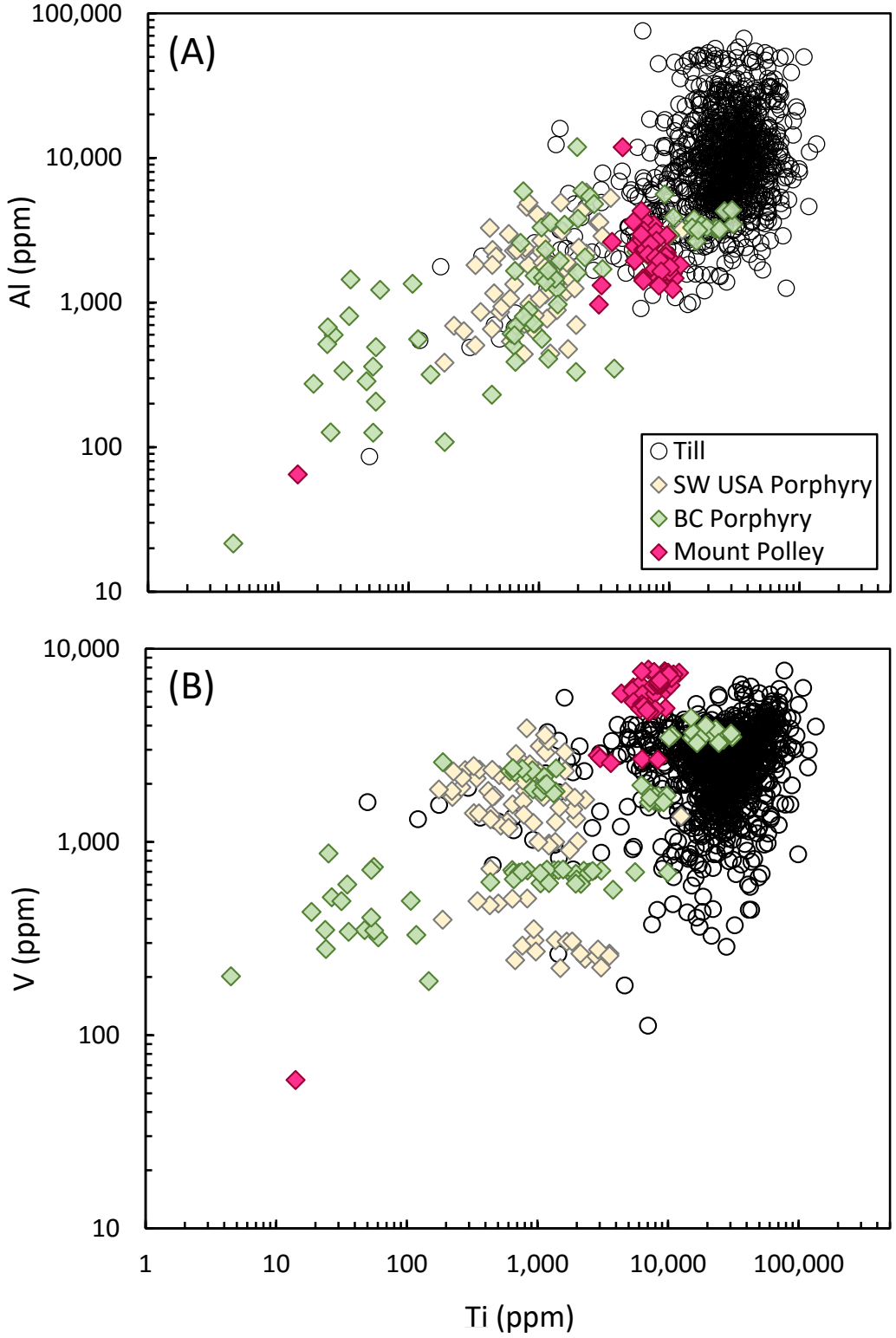
(A)
Al (ppm)
100,000
10,000
1,000
100
10
Till
SW USA Porphyry
BC Porphyry
Mount Polley
(B)
V (ppm)
10,000
1,000
100
10
1
10
100
1,000
10,000
100,000
Ti (ppm)

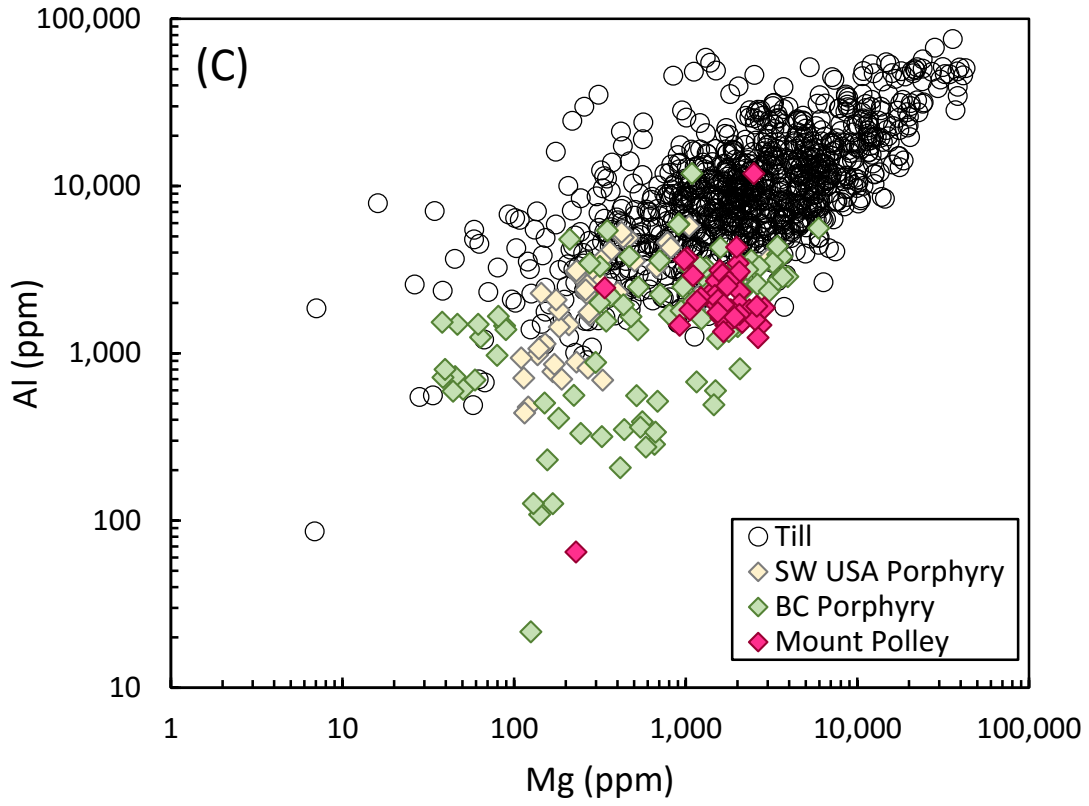
(C)
Al (ppm)
Mg (ppm)
100,000
10,000
1,000
100
10
1
10
100
1,000
10,000
100,000
Till
SW USA Porphyry
BC Porphyry
Mount Polley

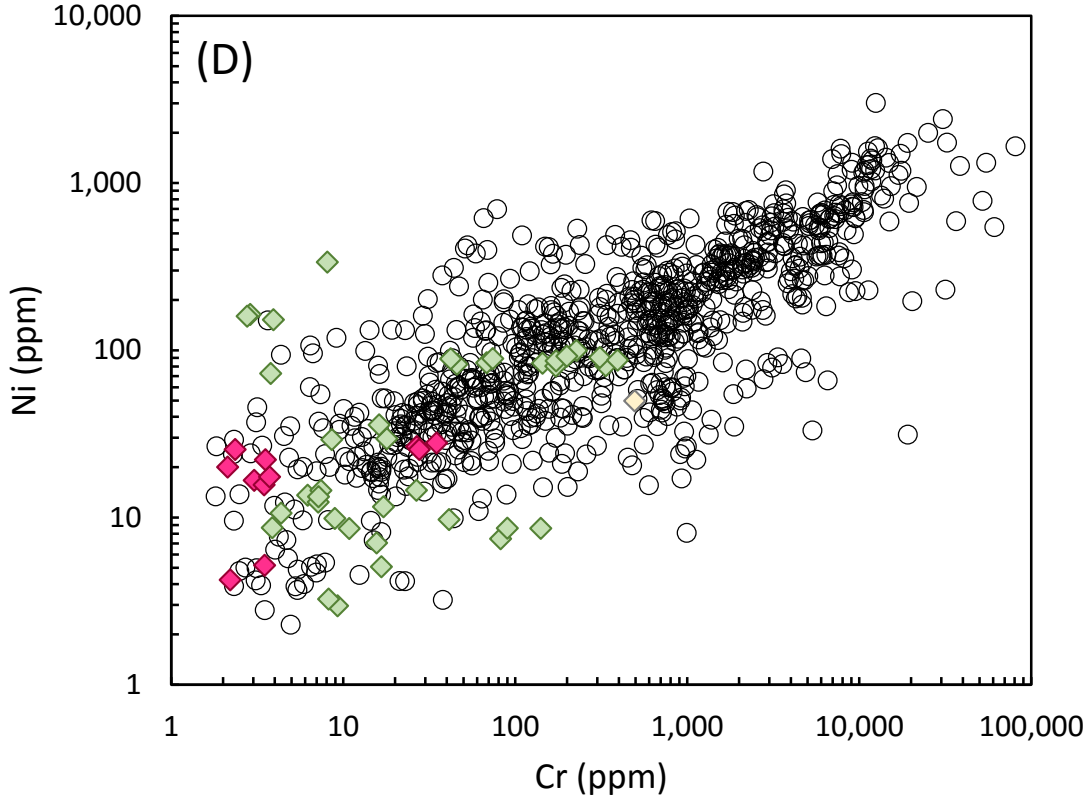
(D)
Ni (ppm)
Cr (ppm)
10,000
1,000
100
10
1
1
10
100
1,000
10,000
100,000

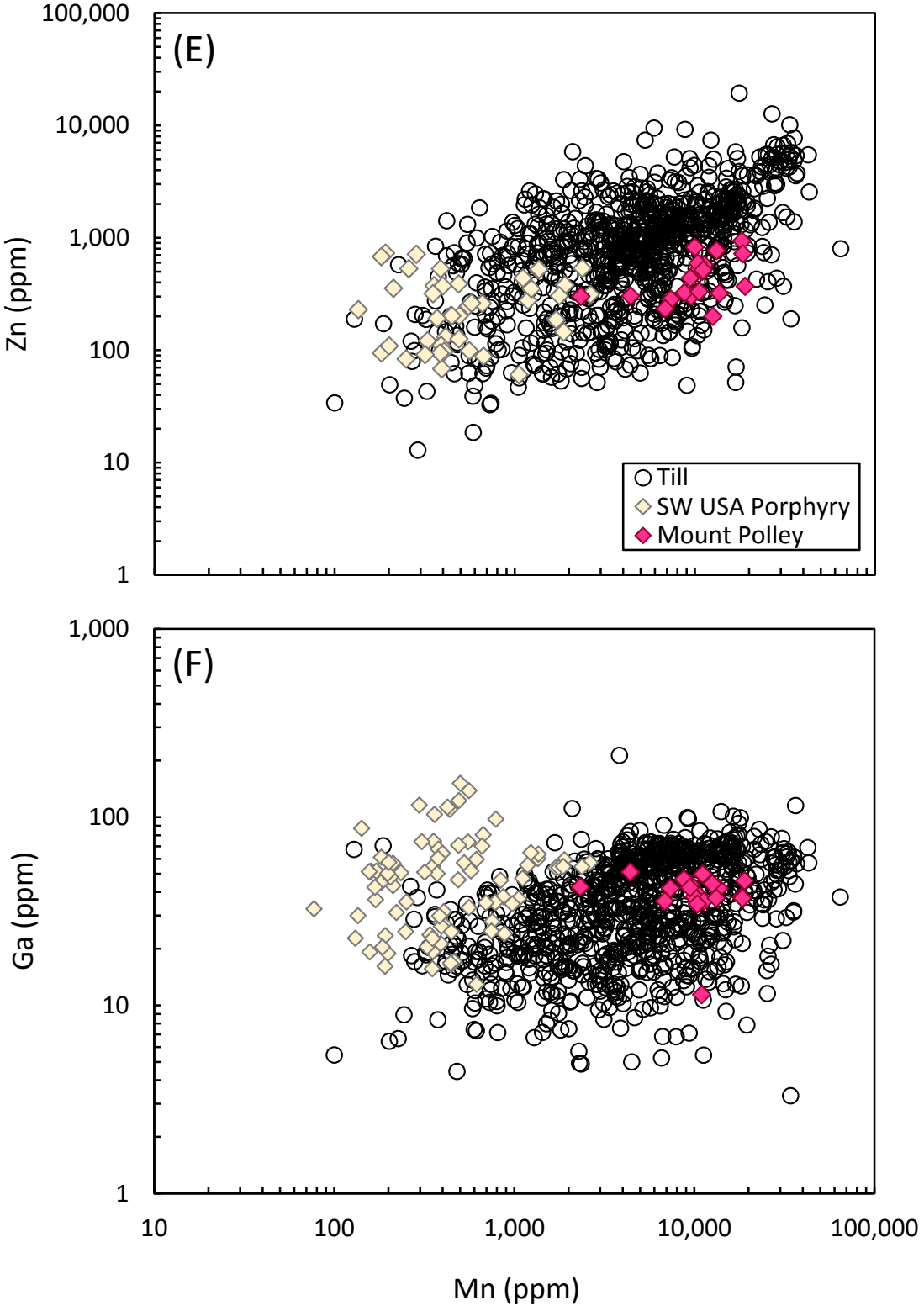
(E)
100,000
10,000
1,000
100
10
1
Zn (ppm)
Till
SW USA Porphyry
Mount Polley
(F)
1,000
100
10
1
Ga (ppm)
10
100
1,000
10,000
100,000
Mn (ppm)

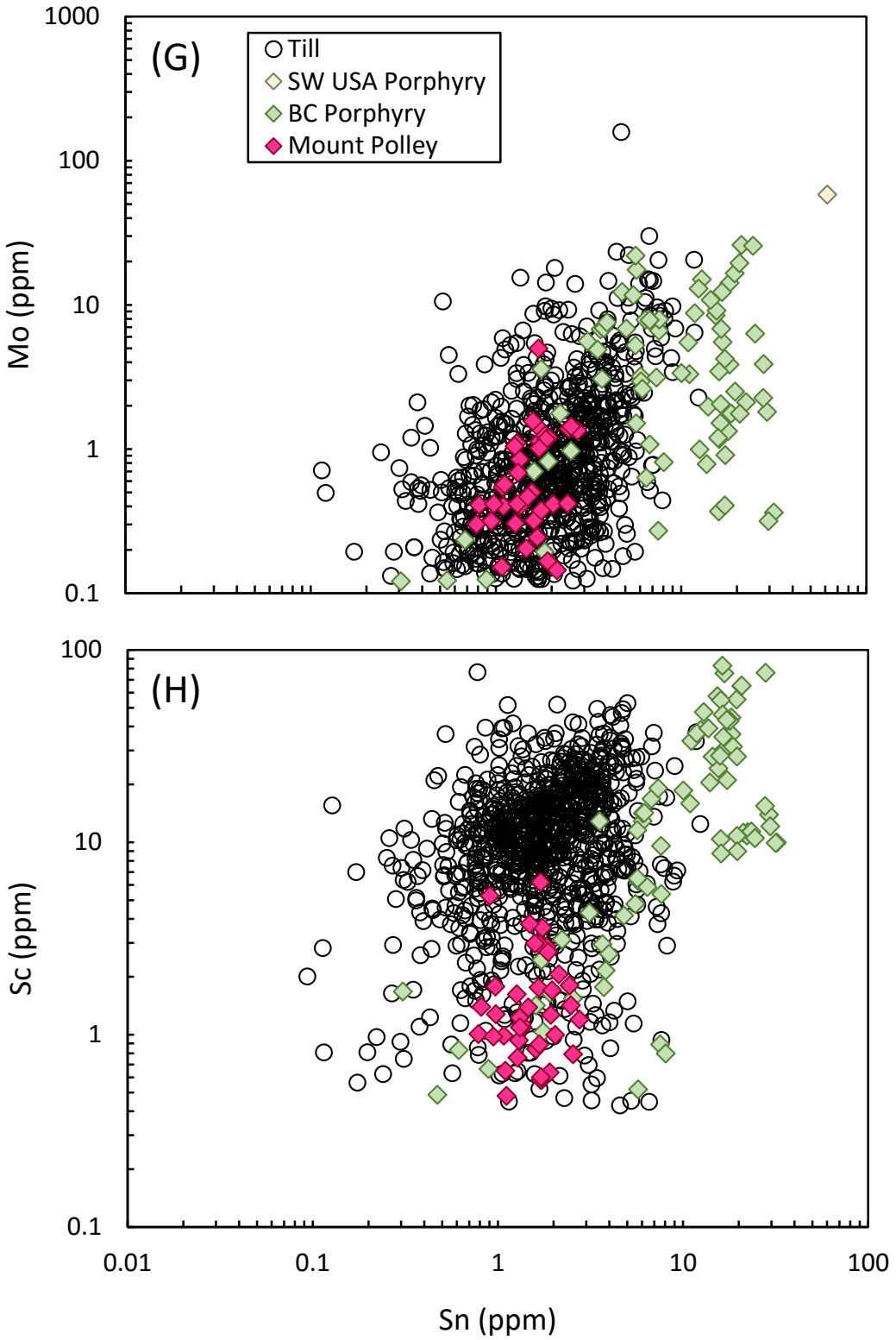
(G)
Till
SW USA Porphyry
BC Porphyry
Mount Polley
Mo (ppm)
1000
100
10
1
0.1
(H)
Sc (ppm)
100
10
1
0.1
0.01
0.1
1
10
100
Sn (ppm)

6. Discussion

6.1 How to Distinguish Hydrothermal Magnetite

6.1.1 Discrimination Diagrams

As noted in the introduction, previous work has attempted to use the trace element chemistry of magnetite to fingerprint a variety of mineral deposit types. This study is specifically focused on the identification of hydrothermal magnetite derived from porphyry systems for which several discrimination diagrams have been proposed. Below I examine how these diagrams perform on magnetite from known porphyry settings, and if any magnetite grains from till samples plot within fields for hydrothermal sources.

Dupuis & Beadoin (2011) developed two diagrams to distinguish magnetite compositions of porphyry, iron-oxide-Cu-Au (IOCG), skarn, Kiruna, banded iron formation (BIF), and Fe-Ti-V deposits. Their plot of Ni/(Cr+Mn) vs. Ti+V was tested by Nadoll et al. (2014) using magnetite from porphyry deposits in the southwest United States. They found that hydrothermal porphyry magnetite plots below the respective field. Similarly, average magnetite compositions from porphyry deposits in British Columbia plot even further below the porphyry field on Ni/(Cr+Mn) vs. Ti+V (Canil et al., in press). Magnetite from the Mount Polley deposit is at the upper limit of Ti+V for porphyry magnetite, but is markedly Mn-enriched of all deposits considered and thus plots significantly far below the porphyry field (Fig. 12). Most magnetite in tills from this study have high Ti+V values and, therefore, fall into the Fe-Ti-V field with very few grains classified as porphyry (Fig. 12).

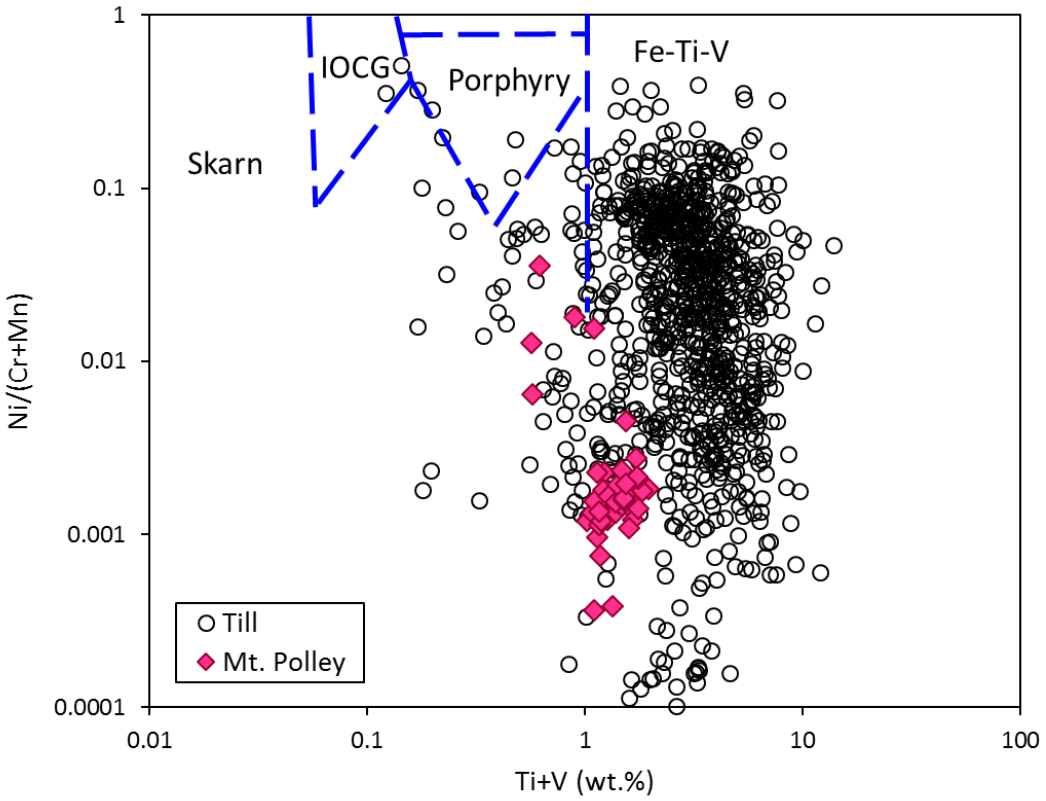

Figure 12. Ni/(Cr+Mn) vs. Ti+V plot for magnetite compositions with discrimination fields from Dupuis & Beaudoin (2011). Magnetite from Mount Polley plots at much lower Ni/(Cr+Mn) values than that proposed for porphyry deposits due to relatively high Mn concentrations at the deposit (data from Canil et al., in press – recalculated using the AYCF calibration method). Most magnetite grains in till plot in the Fe-Ti-V field with very few grains overlapping the porphyry field.

A second discrimination diagram proposed by Dupuis & Beaudoin (2011) for fingerprinting porphyry magnetite is a plot of Ca+Al+Mn vs. Ti+V. Nadoll et al. (2014) found that porphyry magnetite roughly coincides with the respective field, but also extends into the fields for IOCG, skarn, Kiruna and Fe-Ti-V deposits. Magnetite from the Mount Polley deposit plots slightly above the porphyry field, likely due to elevated Mn concentrations in magnetite from the deposit (Fig. 13). Magnetite grains in till from this study mainly overlap with the Fe-Ti-V field, with only a small number of grains (<30) classified as porphyry (Fig. 13). Caution needs to be taken when using this diagram because Ca+Al+Mn values will be grossly modified by sphenitization, which was observed in a number of magnetite grains in till as described in section 5.2.

Nadoll et al. (2014) suggested that Ca be eliminated from the former diagram based on negligible Ca concentrations compared to Al and Mn, and that moderate Ca contents are more likely attributed to impurities. Additionally, they show that the Al+Mn vs. Ti+V diagram exhibits a roughly positive relationship when magnetite is plotted according to estimates of formation temperatures. Nadoll et al. (2015) used this modified diagram to define fields for distinguishing skarn and porphyry deposits from the southwest United States, and a transitional field (skarn + porphyry) for overlap between the deposit types. With the exception of one sample from Mount Polley, the deposit is accurately classified as porphyry, however, magnetite from several unmineralized igneous intrusions (Mountjoy, 2011) and all magnetite from till are all similarly classified as porphyry (or porphyry + skarn) since there is no distinction for igneous magnetite on this diagram (Fig. 14).

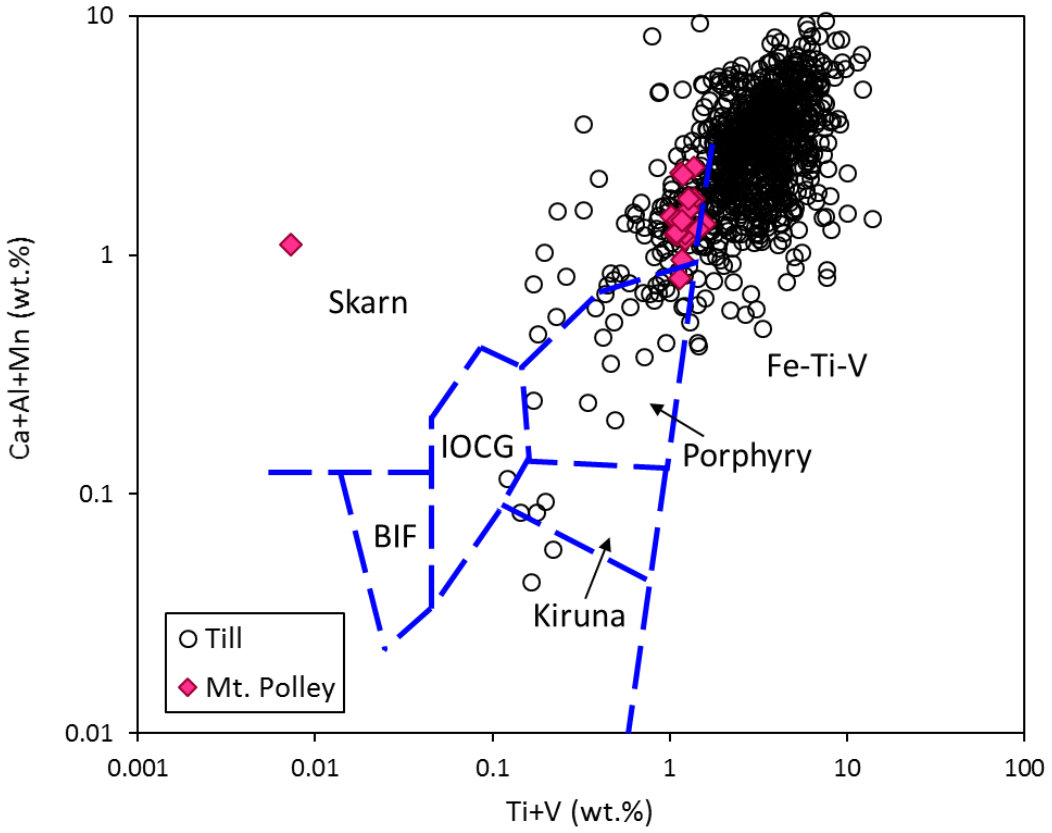

Figure 13. Ca+Al+Mn vs. Ti+V plot of magnetite compositions with discrimination fields from Dupuis & Beaudoin (2011). Magnetite from Mount Polley plots slightly above the porphyry field based on relatively high Mn concentrations (data from Canil et al., in press – recalculated using the AYCF calibration method). Similar to Figure 11, magnetite in till predominantly plots in the Fe-Ti-V field with minor overlap with the porphyry field.

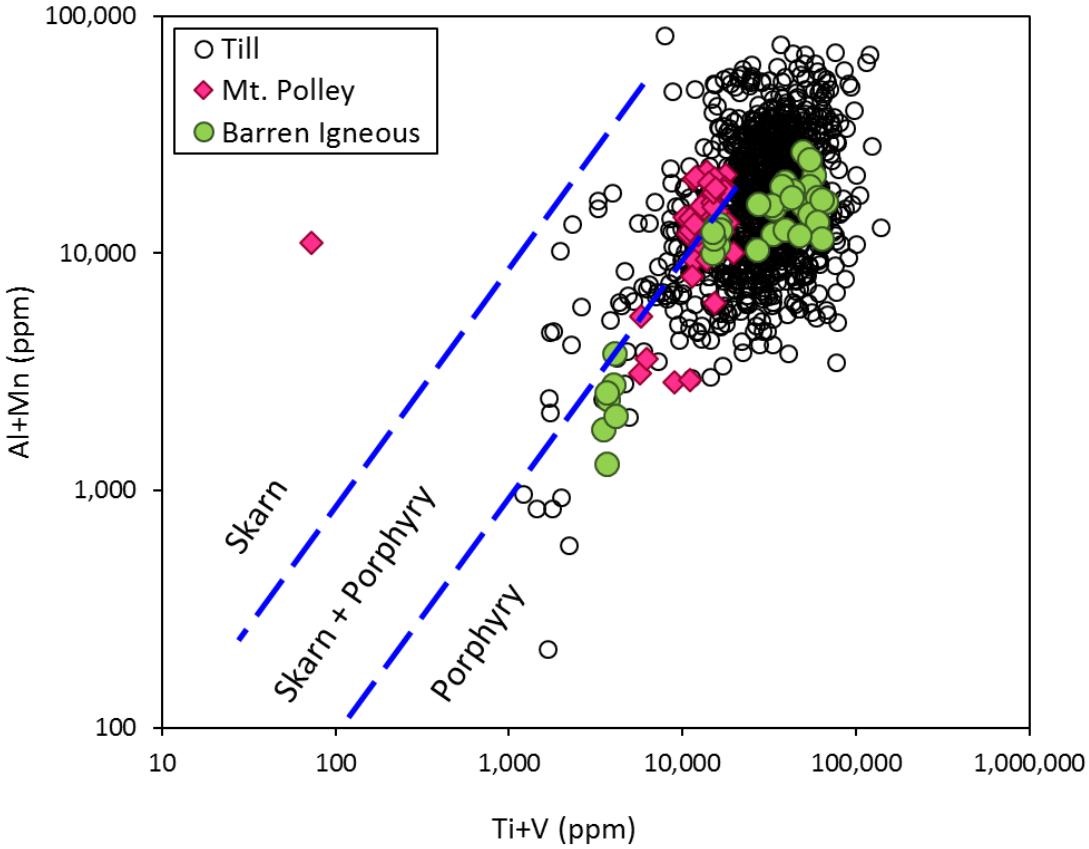

Figure 14. Al+Mn vs. Ti+V plot of magnetite compositions with skarn and porphyry discrimination fields from Nadoll et al. (2015). The skarn+porphyry field is a transitional zone between the two deposit types. Magnetite from Mount Polley is successfully classified as porphyry magnetite, with the exception of one analysis (data from Canil et al., in press – recalculated using the AYCF calibration method). There is no distinction for igneous magnetite, therefore, magnetite data from barren igneous intrusions in the Cordillera (Mountjoy, 2011) and till are erroneously classified as porphyry magnetite.

Finally, a plot of Ti vs. Ni/Cr in magnetite was proposed by Dare et al. (2014) to broadly distinguish hydrothermal from magmatic grains based on the differing behavior of Ni and Cr in fluids versus melts. Canil et al. (in press) showed all hydrothermal porphyry magnetite from Mount Polley fall within the hydrothermal field on this plot (Fig. 15). Chromium is typically in very low concentrations in hydrothermal magnetite (<150 ppm at Mount Polley). Therefore, for a large number of analyses of magnetite from Mount Polley and a small number of magnetite grains in till, the detection limit for Cr was used, producing a minimum Ni/Cr value. Magnetite from the till samples primarily plots in the igneous field, with a small proportion of grains overlapping into the hydrothermal magnetite field (Fig. 15).

According to the proposed discrimination diagrams of Dupuis & Beaudoin (2011), the majority of magnetite from till in this study would be classified as Fe-Ti-V derived, due to elevated Ti+V (Figs. 12, 13). High Ti and V contents are indicative of magnetite formed at magmatic temperatures (Nadoll et al., 2014, 2015; Canil et al., in press) and would suggest that most of the magnetite in till is derived from igneous source rocks. Since neither Ca+Al+Mn nor Ni/(Cr+Mn) values are able to properly identify hydrothermal magnetite from Mount Polley, these diagrams are unsuitable for practice. In the Al+Mn vs. Ti+V diagram of Nadoll et al. (2015), there is no distinction for igneous magnetite and substantial overlap occurs between Mount Polley and till magnetite (Fig. 14). In this way, till grains from this study would be incorrectly identified as sourced from porphyry or transitional skarn + porphyry.

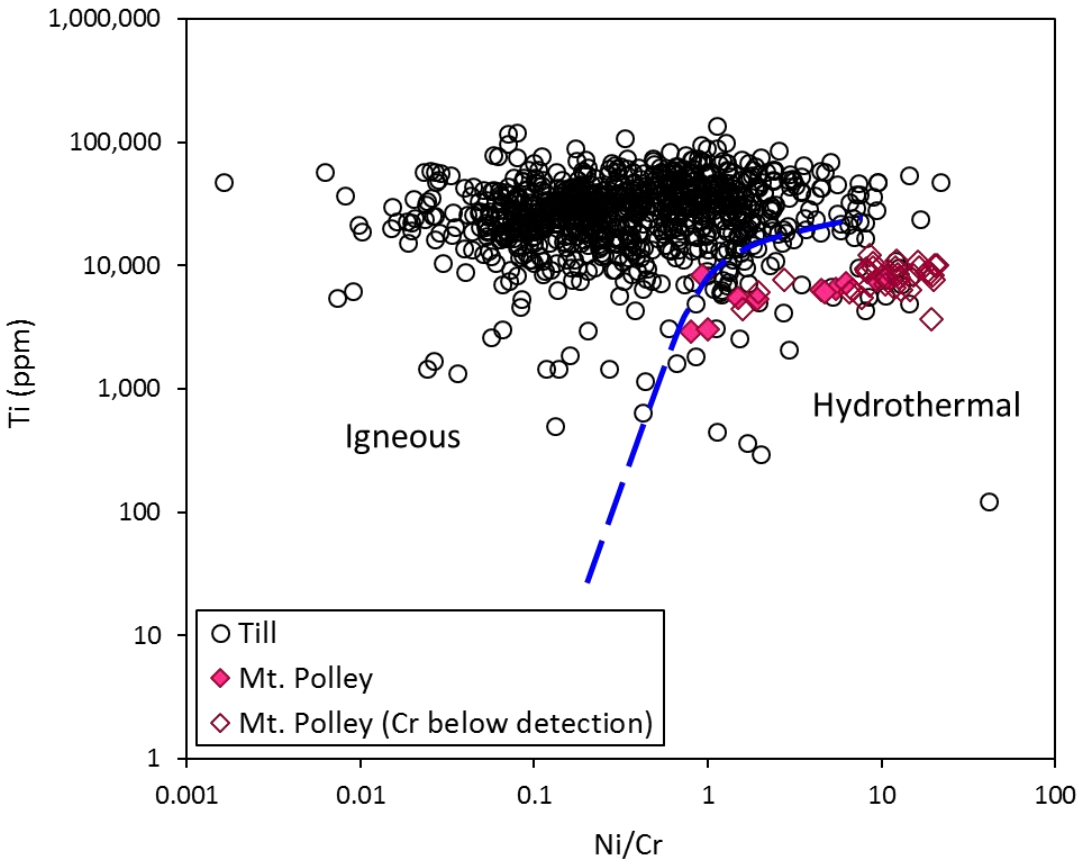

Figure 15. Ti vs. Ni/Cr plot of magnetite compositions with igneous and hydrothermal discrimination fields from Dare et al. (2014). Analyses with Cr values below detection were assigned the detection limit value of 1.76 ppm, which gives the minimum value for Ni/Cr. Magnetite from Mount Polley is successfully classified as porphyry magnetite (data from Canil et al., in press – recalculated using the AYCF calibration method). Magnetite from till is predominantly classified as igneous, but a small proportion of grains overlap into the hydrothermal field.

Evidently, there is too wide of a compositional range in hydrothermal porphyry magnetite to be accurately classified using these binary diagrams. The Ti vs. Ni/Cr diagram of Dare et al. (2014) shows potential for application of magnetite in exploration for porphyry deposits (Fig. 15), but Cr is distinctly low in hydrothermal magnetite and detection limits may pose a problem.

6.1.2 Statistical Analysis

A robust approach to characterizing the chemistry of magnetite as an indicator is to use a multivariate statistical method that applies the collective significance of all elements of interest. Discriminant analysis is a powerful technique that has been routinely used to test for differences between pre-defined groups in geochemical datasets (Davis, 2002). The analysis establishes discriminant functions that use a weighted combination of the variables (in this case elements) to provide the maximum separation and distinction between compositional groups. Each function transforms data into a single discriminant score, which is then used to allocate unknown samples to one of the pre-defined groups. In the context of this study, the primary goal of discriminant analysis is to first determine which elements have the most discriminating power between magnetite compositions from various sources. Those elements are then used to define discriminant functions that can identify the provenance of magnetite grains based on their composition.

Magnetite Database:

The first step was to compile magnetite compositions determined by LA-ICP-MS from various localities. A summary of the sources used for magnetite data and the deposits/samples studied is given in Table 2. Two datasets were formed from the compiled magnetite data for which separate discriminant analyses were performed, therefore

Table 2. Summary of magnetite compositional data obtained from various porphyry deposits and barren igneous intrusions.

Source	Elements Analyzed	Locality	Sample Type	n
Canil et al. (in press)	Mg, Al, Si, Sc, Ti, V, Cr, Mn, Co, Ni, Cu, Nb, Mo, Sn, W, Re	Copper Mountain Cu-Au deposit, BC, CAN	HTP	19
		Endako Mo deposit, BC, CAN	HTP	14
		Island Copper Cu-Mo-Au deposit, BC, CAN	HTP	27
			OIG	12
		Mount Polley Cu-Au deposit, BC, CAN	HTP	45
			OIG	5
		Pine Cu-Au deposit, BC, CAN	HTP	28
Mountjoy (2011)	Mg, Al, Sc, Ti, V, Mn, Co, Ni, Cu, Nb, Mo, Sn, W	Highland Valley Cu deposit, BC, CAN	OIG	32
		Hushamu intrusion, BC, CAN	BIG	9
		Nimpkish batholith, BC, CAN	BIG	7
		Mesachie Lake pluton, BC, CAN	BIG	16
		Argonaut intrusion, BC, CAN	BIG	8
Nadoll et al. (2015)	Na, Mg, Al, Si, S, Ca, Ti, V, Cr, Mn, Co, Ni, Cu, Zn, Ga, Ge, As, Se, Sr, Y, Nb, Mo, Ag, In, Sn, Ba, Ce, Au, Tl, Pb, Th	Chino Cu deposit, NM, USA	HTP	13
			OIG	32
		Cobre Cu deposit, NM, USA	HTP	8
			OIG	8
		Henderson Mo deposit, CO, USA	OIG	41
		Morenci Cu deposit, AZ, USA	HTP	8
			OIG	5
		Morenci Garfield Cu deposit, AZ, USA	OIG	7
		Morenci Producer Cu deposit, AZ, USA	HTP	7
			OIG	1
		Morenci Sun Ridge Cu deposit, AZ, USA	HTP	15
			OIG	4
		Safford Dos Pobres Cu deposit, AZ, USA	HTP	24
			OIG	7
		Safford Lone Star Cu deposit, AZ, USA	HTP	25
			OIG	20
		Safford San Juan Cu deposit, AZ, USA	HTP	18
			OIG	16
		Inner Zone Batholith, Japan	BIG	12

Abbreviations: n – sample size, HTP – hydrothermal porphyry, OIG – ore igneous, BIG – barren igneous.
Note: only elements that were analyzed in magnetite from all localities by the respective author are listed.

allowing a comparison of the results of the discriminant analysis using data collected at different laboratories using varying analytical procedures. The first dataset (subsequently referred to as MDB1) consists of magnetite compositions from Canil et al. (in press) and Mountjoy (2011) for six porphyry Cu(-Au-Mo) deposits and four barren igneous intrusions in the Canadian Cordillera. All data was obtained in the same LA-ICP-MS laboratory, thus providing an internally consistent dataset. Additionally, the LA-ICP-MS data of Canil et al. (in press) was re-calibrated using the AYCF method. The second dataset (MDB2) was formed by a combination of the aforementioned data with the magnetite database of Nadoll et al. (2015). The latter database consists of magnetite measured at a different LA-ICP-MS laboratory from four porphyry Cu deposits, one Climax-Mo deposit (southwest United States) and barren igneous magnetite (Japan). The larger MDB2 dataset is less internally consistent, but is a more comprehensive representation of porphyry magnetite composition from a large number of deposits and rocks in more than one geographical location.

Based on occurrence, magnetite samples in both datasets were classified into three petrologically distinct groups that make up the training dataset for statistical analysis. Hydrothermal porphyry magnetite (HTP) shows direct petrographic evidence of precipitation from fluids (by occurring in veins and hydrothermal breccias). Ore igneous magnetite (OIG) is euhedral-subhedral and occurs in fresh or altered intrusive rocks located at a porphyry deposit. Barren igneous magnetite (BIG) is euhedral-subhedral as well, but from unmineralized intrusions that are remote from or show no relation to any ore deposit. Summary statistics for the compositional groupings for magnetite in the MDB1 and MDB2 datasets are given in Tables 3 and 4, respectively. Only those elements that are common between the magnetite data sources were considered.

Table 3. Summary statistics for magnetite compositional groups in the MDB1 dataset.

Element (ppm)	Hydrothermal Porphyry (HTP) n = 133				Ore Igneous (OIG) n = 49				Barren Igneous (BIG) n = 40			
	Min	**Max**	**Median**	**σ**	**Min**	**Max**	**Median**	**σ**	**Min**	**Max**	**Median**	**σ**
Mg	38	5,950	1,103	1,053	28	8,917	242	2,131	22	4,040	1,295	1,125
Al	22	11,904	1,869	1,760	439	18,241	2,442	5,299	493	25,780	11,790	5,817
Sc	0.5	82.9	5.0	19.1	0.4	189.4	5.6	40.2	0.5	14.7	8.3	4.5
Ti	5	31,027	5,445	6,338	37	48,280	2,870	13,322	325	61,670	32,315	19,444
V	59	7,814	2,273	2,431	401	3,698	2,679	1,076	3,020	7,090	4,239	1,285
Mn	122	20,226	2,213	5,501	143	11,528	1,252	2,792	613	6,724	1,474	1,863
Co	2	143	30	18	9	178	54	33	27	73	48	11
Ni	2.4	337	26.1	44.5	16.6	300	62.8	53.2	8.9	47.5	30.6	9.4
Cu	0.6	6,115	4.8	620	0.6	4,467	14.2	885	0.6	43.6	5.1	9.0
Nb	0.06	16.5	0.27	3.98	0.07	32.7	6.60	8.92	0.05	15.8	1.30	4.68
Mo	1.1	26.1	1.5	5.4	0.1	88.8	2.6	20.2	0.1	16.7	11.6	6.7
Sn	0.3	32.1	4.0	8.4	0.1	116	1.2	31.9	0.1	20.4	9.4	6.0
W	0.04	2.66	0.38	0.47	0.04	5.27	0.25	1.06	0.04	2.35	0.39	0.51

Magnetite compositional data from Mountjoy (2011) and Canil et al. (in press) as listed in Table 2. Only elements common between sources are listed.
Abbreviations: σ – standard deviation of the mean.

Table 4. Summary statistics for magnetite compositional groups in the MDB2 dataset.

Element (ppm)	Hydrothermal Porphyry (HTP) n = 251				Ore Igneous (OIG) n = 190				Barren Igneous (BIG) n = 52			
	Min	**Max**	**Median**	**σ**	**Min**	**Max**	**Median**	**σ**	**Min**	**Max**	**Median**	**σ**
Mg	38	5,950	672	1,015	28	8,917	391	1,497	22	4,040	919	1,069
Al	22	11,904	1,818	1,614	439	19,070	3,030	3,974	493	25,780	10,350	6,370
Ti	5	31,027	1,382	5,565	37	97,796	2,213	18,095	50	61,670	18,140	21,039
V	59	7,814	1,713	2,053	74	6,657	2,014	1,140	2,210	7,090	3,800	1,321
Mn	77	20,226	754	4,601	115	12,548	1,054	2,956	441	6,724	1,532	1,708
Co	2	143	35	19	5	178	47	29	27	502	50	65
Ni	2.4	389	28.9	63.4	16.6	448	74.8	101	8.9	192	33.1	33.7
Cu	0.6	6,115	5.8	660	0.04	4,467	11.1	736.5	0.4	1,950	5.4	408
Nb	0.06	16.5	0.27	4.40	0.01	411	8.60	57.7	0.01	15.8	0.60	4.54
Mo	0.1	225	1.7	25.6	0.01	88.8	3.9	20.7	0.06	16.7	7.6	7.0
Sn	0.31	70.1	5.52	11.2	0.03	210	44.8	49.6	0.09	20.4	9.40	5.97

Magnetite compositional data from Mountjoy (2011), Nadoll et al. (2015) and Canil et al. (in press) as listed in Table 2. Only elements common between sources are listed. Abbreviations: σ – standard deviation of the mean.

Discriminant analysis requires values for all selected elements of interest. Data for the composition of magnetite from skarn deposits was available in the studies used for the compilation of MDB1 and MDB2. Magnetite in skarn, however, contains very low trace element abundances that are commonly below detection/reporting limits. For this reason, skarn was excluded as a compositional group for discriminant analysis of magnetite.

Selection and Treatment of Variables:

Only those elements that are common between the magnetite data sources could be selected as variables for discriminant analysis (Tables 3, 4). Additionally, the analysis requires values for all elements, therefore, only those elements with a sufficient number of LA-ICP-MS analyses above the limit of detection were considered. For the internally consistent MDB1 dataset, only elements Mg, Al, Ti, V, Mn, Co, Ni and Sn were selected as variables, since Cu, Nb, Mo and Sn were only measurable in 60-80% of the analyses. For the MDB2 dataset, a larger number of analyses have elements below detection. This is due to the higher limit of reporting (10σ of the background) criterion used by Nadoll et al. (2015), compared to the detection limit (3σ of the background) criterion of Mountjoy (2011) and Canil et al. (in press). To maximize the number of samples from the Nadoll et al. (2015) data that would be included in the analysis, only elements Mg, Al, Ti, V, Mn, Co and Ni were considered (Sn excluded). Censored values were not used to substitute for any elements that are below detection, therefore, these analyses were excluded. The variability in magnetite composition for each group using the selected elements of interest are shown in Figures 16 and 17.

Discriminant analysis assumes that each variable is normally distributed. Geochemical data, however, is commonly skewed and/or contains outliers (Reimann &

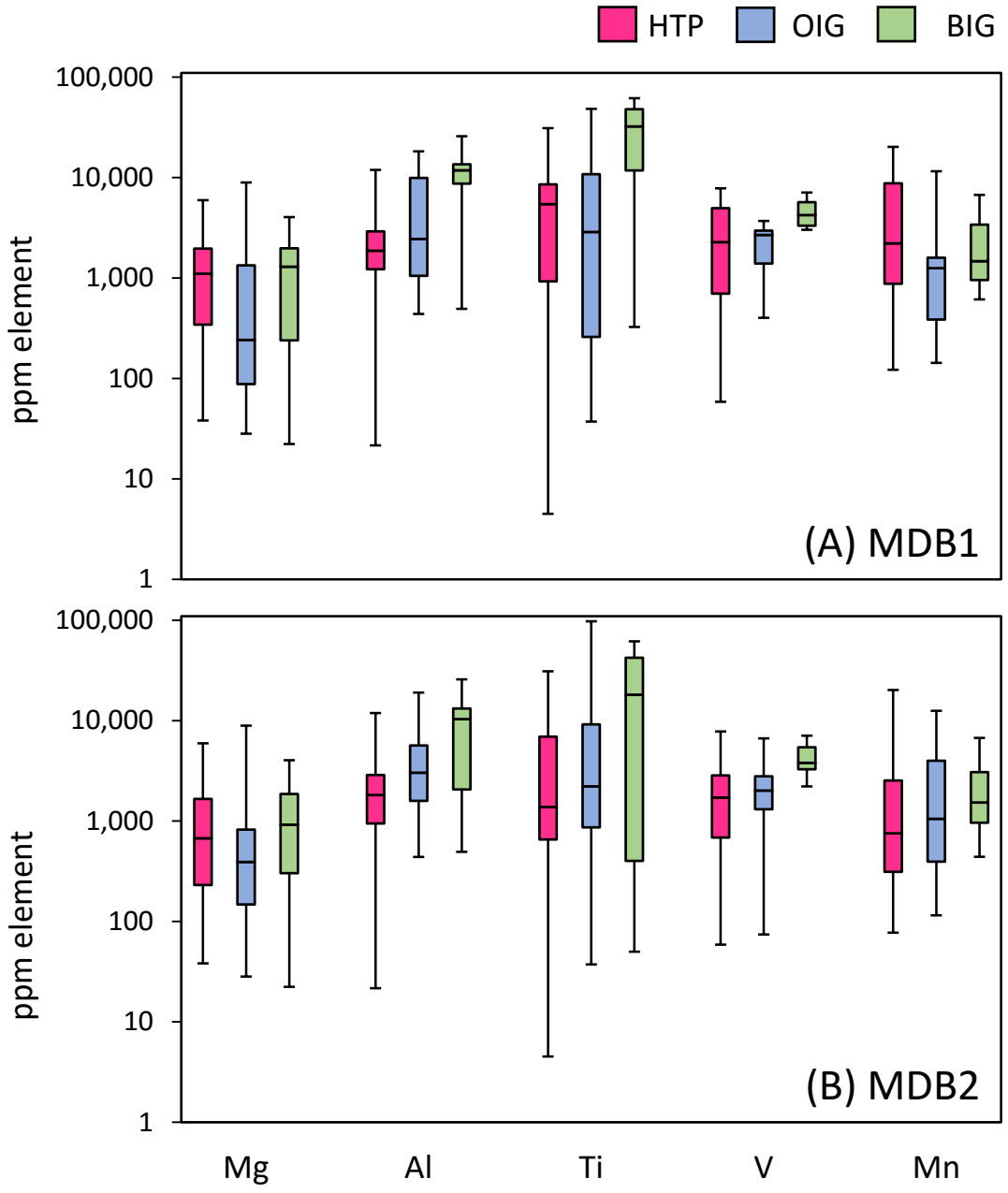

Figure 16. Box and whisker plots showing variation for minor elements Mg, Al, Ti, V and Mn in the compositional groups of magnetite classified from barren igneous rocks (BIG), ore-related igneous rocks (OIG) and hydrothermal porphyry related (HTP) for A) MDB1 and B) MDB2. The two datasets are broadly similar, with the exception of lower Al and Ti values in BIG from MDB2.

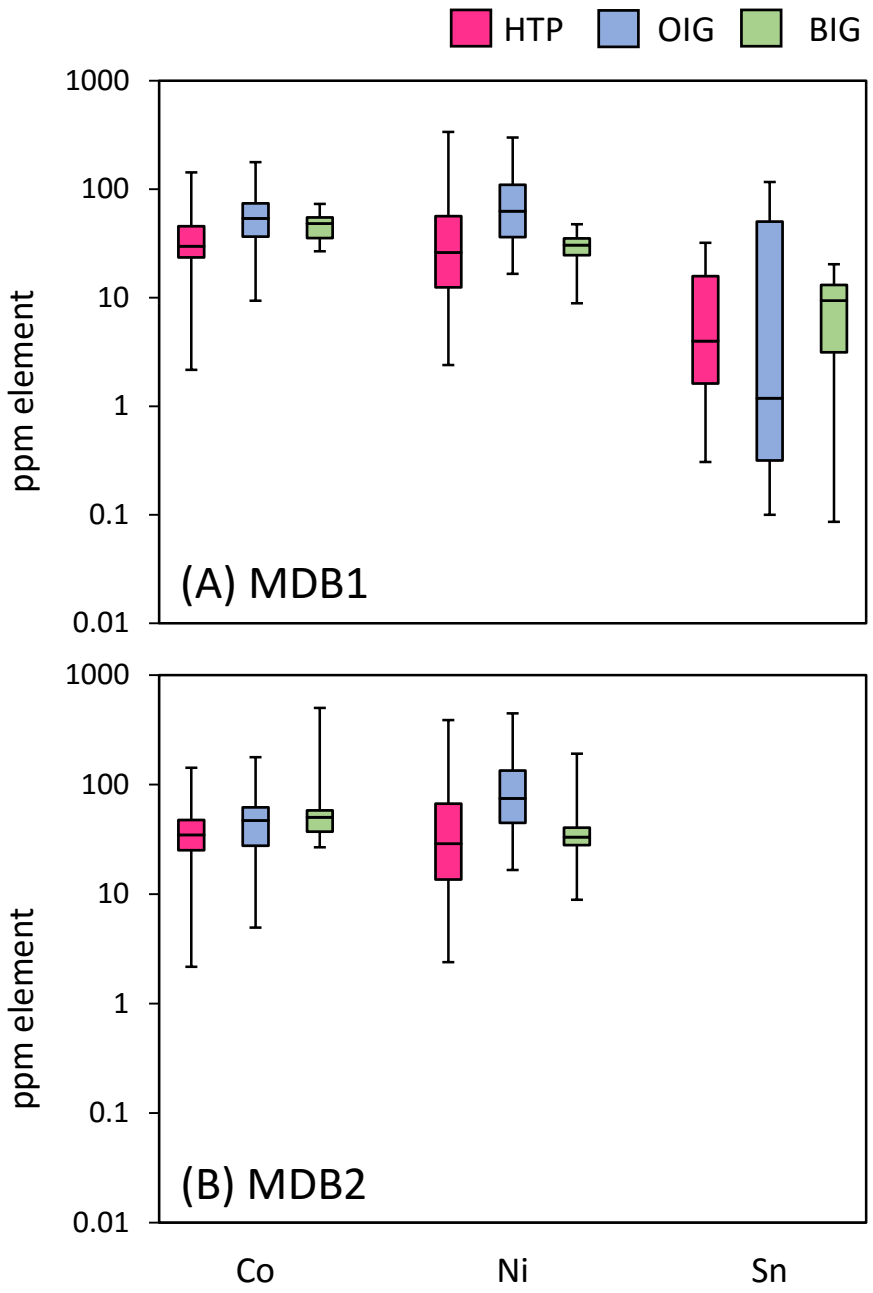

Figure 17. Box and whisker plots showing variation for trace elements Co, Ni and Sn in the compositional groups of magnetite classified from barren igneous rocks (BIG), ore-related igneous rocks (OIG) and hydrothermal porphyry related (HTP) for A) MDB1 and B) MDB2. Note that Sn was not included in MDB2 due to an insufficient number of analyses.

Filzmoser, 2000). Additionally, compositional data is constrained to a constant sum of 100%, which introduces effects of data closure in statistical analysis (Chayes, 1960). This conflicts with the assumption of variable independence since a change in any one element concentration is negatively correlated with other elements (Chayes, 1960; Vermeesch, 2006). To minimize deviations from normality and prevent the effects of data closure, each element (x_i) was transformed using the additive log-ratio method of Atchison (1986):

$$y_i = ln\left({}^{x_i}/_{x_D}\right) \quad i = 1, \ldots\ldots, D-1 \tag{3}$$

This method transforms D-part compositional data into (D – 1)-dimensional Euclidean space to which multivariate statistical methods can be applied. Iron was chosen as the component divisor (x_D) due to its high concentration and minimal variation (<10%) in magnetite. Transformed data for magnetite was imported into SYSTAT 13, a statistical software package, to perform the discriminant analysis.

Linear Discriminant Analysis

The linear method of discriminant analysis (LDA) was chosen due to the simplicity of linear functions as compared to quadratic discriminant analysis (QDA), which contain a large number of parameters that are far more complex and difficult to interpret. The number of functions generated by discriminant analysis is one less than the number of groups, therefore, two linear functions will be derived in which to distinguish magnetite. The caveat of LDA is that equal covariance between groups is required to produce reliable discriminant functions. Although QDA is the preferred method for datasets with unequal covariance, studies show that LDA is a very close approximation and can even perform better on independent test data (Vermeesch, 2006). As a comparison, both LDA and QDA

methods were carried out on both datasets and the discriminant models were tested based on their predictive power for independent test data. There was no significant improvement using QDA, therefore, it can be assumed that differences in dispersion between groups is not substantial and only the results of LDA will be discussed further.

To assess the capability of LDA for distinguishing magnetite composition, the MDB1 and MDB2 datasets were each subdivided into two parts: 1) a random 65% of the data used as 'training' for the discriminant analysis, and 2) the remaining 35% left as independent 'test' data. First, the optimum set of elements was determined as some may not significantly contribute to the discriminating power of the functions and can, therefore, be eliminated from the analysis. The stepwise method of discriminant analysis is often used for this purpose. The forward stepwise method incrementally adds elements into the discriminant analysis based on their contribution to the model as indicated by the associated change in the Wilks lambda parameter. The Wilks lambda parameter is a measure of the discriminating power, with values closer to zero indicating greater power for the chosen element(s). Decreasing the number of variables in the discriminant analysis will naturally cause an increase in the Wilks lambda parameter since the variation in the dataset is now being explained by fewer variables. Table 5 lists the Wilks lambda values associated with each element ranked in order of discriminating power by forward-stepping LDA using the training datasets. At 0.05 level of significance, all eight elements (Mg, Al, Ti, V, Mn, Co, Ni and Sn) were considered significant for the MDB1 training data, whereas, only Al, Mg, Ni and Co were significant for the MDB2 training data.

Although the stepwise method of discriminant analysis has been commonly used to optimize variable selection in many studies, it is not always the best method for selecting

Table 5. Wilks lambda (λ) values as determined by forward stepwise linear discriminant analysis.

MDB1		MDB2	
Element	**λ**	**Element**	**λ**
Al	0.761	Al	0.673
Mg	0.531	Mg	0.530
Ni	0.419	Ni	0.391
Sn	0.359	Co	0.361
V	0.321	Ti	0.344
Mn	0.259	V	0.318
Co	0.231	Mn	0.305
Ti	0.225		

Note: forward-stepping LDA was only performed on 65% of each dataset.

the most useful subset of variables (Thompson, 1995). Alternatively, multiple iterations of discriminant analyses can be performed where each element is manually removed in turn from the analysis and each discriminant model is evaluated based on the ability of the functions to correctly classify samples from an independent test dataset. Table 6 summarizes classification results on the 'test' data using various manually chosen element subsets for LDA, showing rankings according to percentage successful classification and the associated Wilks lambda value. For MDB1, 91% successful classification was achieved when Ti and Sn were excluded from the analysis. This is contrary to stepwise LDA, which determined that all eight elements (Mg, Al, Ti, V, Mn, Co, Ni and Sn) were significant in the model. Similarly, stepwise LDA determined that Mg, Al, Co and Ni were significant for the MDB2 training data, but the derived functions using only these four elements performed relatively poorly on the test data at 66% success. In contrast, 78% successful classification was achieved when using all seven elements (Mg, Al, Ti, V, Mn, Co and Ni). Evidently, the stepwise method is not ideal for variable selection in this case. Therefore, only the elements with the greatest predictive power for the independent test data were selected for further analysis. Table 7 is a detailed summary of the classification for the magnetite compositional groups using the preferred set of elements for each dataset.

The successful classification of test data using the preliminary discriminant models derived from the training data were statistically significant, therefore, discriminant analysis could then be confidently performed on the entire 100% of each dataset. Table 8 summarizes the results of the full analyses, subsequently referred to as LDA1 and LDA2 for MDB1 and MDB2, respectively (Appendix E). The discriminant functions for LDA1 are given in equations 4-5:

Table 6. Linear discriminant analysis classification summary of independent test data.

A) MDB1

	Elements Included	Elements Removed	% Class	λ
1	Mg, Al, V, Mn, Co, Ni	Ti, Sn	91	0.258
2	Mg, Al, V, Mn, Co, Ni, Sn	Ti	89	0.231
3	Mg, Al, Ti, V, Mn, Co, Ni, Sn	None	88	0.225
4	Mg, Al, Ti, V, Mn, Co, Ni	Sn	84	0.229
5	Al, Ti, V, Mn, Co, Ni	Mg, Sn	84	0.349
6	Al, V, Mn, Co, Ni, Sn	Ti, Mg	84	0.365
7	Al, Ti, V, Mn, Co, Ni, Sn	Mg	82	0.343
8	Al, V, Mn, Co, Ni	Ti, Mg, Sn	82	0.425
9	Mg, Al, Ti, V, Mn, Ni, Sn	Co	80	0.255
10	Mg, Al, Ti, V, Mn, Co, Sn	Ni	80	0.322
11	Mg, Al, Ti, Mn, Co, Ni, Sn	V	79	0.268
12	Mg, Ti, V, Mn, Co, Ni, Sn	Al	73	0.433
13	Mg, Al, Ti, V, Co, Ni, Sn	Mn	64	0.284

B) MDB2

	Elements Included	Elements Removed	% Class	λ
1	Mg, Al, Ti, V, Mn, Co, Ni	None	78	0.305
2	Mg, Al, Ti, V, Co, Ni	Mn	77	0.318
3	Mg, Al, Ti, V, Mn, Ni	Co	76	0.318
4	Mg, Al, Ti, Mn, Co, Ni	V	76	0.338
5	Mg, Al, Ti, Co, Ni	Mn, V	76	0.344
6	Mg, Al, Ti, V, Ni	Mn, Co	74	0.327
7	Al, Ti, V, Mn, Co, Ni	Mg	72	0.401
8	Mg, Al, Ti, V, Mn, Co	Ni	72	0.473
9	Mg, Al, V, Mn, Co, Ni	Ti	71	0.322
10	Mg, Al, Ti, Ni	Mn, V, Co	67	0.370
11	Mg, Al, Co, Ni	Mn, V, Ti	66	0.361
12	Mg, Ti, V, Mn, Co, Ni	Al	63	0.501

Discriminant functions calculated on 65% of the MDB1 and MDB2 datasets and applied to the remaining 35% of the data. Abbreviations: % Class - percentage of successfully classified data from the test set; λ – Wilks lambda parameter.

Table 7. Linear discriminant analysis classification summary for individual magnetite groups.

A) MDB1 Elements: Mg, Al, V, Mn, Co and Ni

		Predicted Group				
		HTP	**OIG**	**BIG**	**Total**	**%**
Actual Group	**HTP**	30	3	1	34	88
	OIG	0	6	1	7	86
	BIG	0	0	15	15	100
					56	**91%**

B) MDB2 Elements: Mg, Al, Ti, V, Mn, Co and Ni

		Predicted Group				
		HTP	**OIG**	**BIG**	**Total**	**%**
Actual Group	**HTP**	50	8	2	60	83
	OIG	4	19	2	25	76
	BIG	1	5	10	16	63
					101	**78%**

Discriminant functions calculated on 65% of the MDB1 and MDB2 datasets and applied to the remaining 35% of the data. Abbreviations: HTP – hydrothermal porphyry, OIG – ore igneous, BIG – barren igneous.

Table 8. Results of linear discriminant analysis.

A) LDA1 **Dataset: MDB1**

Discriminant Functions			**Standardized Functions**			**Scores of Group Means**		
	F1	**F2**		**F1**	**F2**		**F1**	**F2**
Mg	0.703	0.384	Mg	0.956	0.521	BIG	-1.791	0.995
Al	-1.387	0.091	Al	-1.401	0.092	HTP	1.030	0.049
V	-0.075	1.169	V	-0.666	1.039	OIG	-1.399	-1.005
Mn	0.412	-0.750	Mn	0.549	-1.000			
Co	-0.827	-0.525	Co	-0.509	-0.323			
Ni	-0.306	-1.149	Ni	-0.268	-1.005	**Statistics**		
Constant	-12.150	-11.256					**F1**	**F2**
						Eigenvalue	1.667	0.402
Wilks lambda: 0.268						Canonical Correlation	0.791	0.535
p-value: <0.001						Cumulative Dispersion	0.806	1.000
N = 218								

B) LDA2 **Dataset: MDB2**

Discriminant Functions			**Standardized Functions**			**Scores of Group Means**		
	F1	**F2**		**F1**	**F2**		**F1**	**F2**
Mg	0.627	0.477	Mg	0.814	0.619	BIG	-1.553	0.831
Al	-1.500	0.281	Al	-1.493	0.279	HTP	1.030	0.068
Ti	0.259	-0.192	Ti	0.529	-0.392	OIG	-1.064	-0.784
V	-0.404	0.790	V	-0.354	0.691			
Mn	0.212	-0.439	Mn	0.275	-0.571			
Co	-0.541	0.215	Co	-0.354	0.141	**Statistics**		
Ni	-0.567	-1.043	Ni	-0.501	-0.92		**F1**	**F2**
Constant	-14.699	-2.355				Eigenvalue	1.356	0.295
						Canonical Correlation	0.759	0.477
Wilks lambda: 0.328						Cumulative Dispersion	0.821	1.000
p-value: <0.001								
N = 253								

Abbreviations: F1: factor 1, F2: factor 2. The coefficients in the standardized functions are normalized to the variance of each element. Eigenvalues indicate the amount of variance explained by each function. The canonical correlation is a measure of the correlation between the discriminant scores and the variables. Cumulative dispersion is the percentage of variance that is added by each function.

$$F1 = 0.703Mg - 1.387Al - 0.075V + 0.412Mn - 0.827Co - 0.306Ni - 12.15 \quad (4)$$

$$F2 = 0.384Mg + 0.091Al + 1.169V - 0.75Mn - 0.525Co - 1.149Ni - 11.256 \quad (5)$$

The discriminant functions for LDA2 are given in equations 6-7:

$$F1 = 0.627Mg - 1.5Al + 0.259Ti - 0.404V + 0.212Mn - 0.541Co - 0.567Ni - 14.699 \quad (6)$$

$$F2 = 0.477Mg + 0.281Al - 0.192Ti + 0.79V - 0.439Mn + 0.215Co - 1.043Ni - 2.355 \quad (7)$$

The discriminant scores for the datasets shows a clear separation of the magnetite compositional groups on a territorial plot of the linear functions (Fig. 18). Equations for the field boundaries are calculated as points equidistant from the respective group means for which they separate (Table 9). Factor 1 (F1) effectively separates hydrothermal magnetite (HTP) from the ore (OIG) and barren (BIG) igneous groups for both analyses, with hydrothermal magnetite generally characterized by positive F1 values. Coefficients of the standardized discriminant functions can be used as an indication of the relative importance of each variable on the respective function (Table 8). Magnesium and Al have the greatest influence on F1, suggesting these two elements have the strongest discriminating power for separating hydrothermal from igneous magnetite. Factor 2 (F2) effectively separates ore and barren igneous magnetite, with the latter tending towards positive F2 values. Differences in the analyses is apparent in the standardized coefficients of the second function since F2 is mostly influenced by Mn, Ni and V, but the significance of Mn and V are relatively lower in LDA2. Slight variation is expected between the analyses because of the difference in variables selected. Minor overlap is observed between

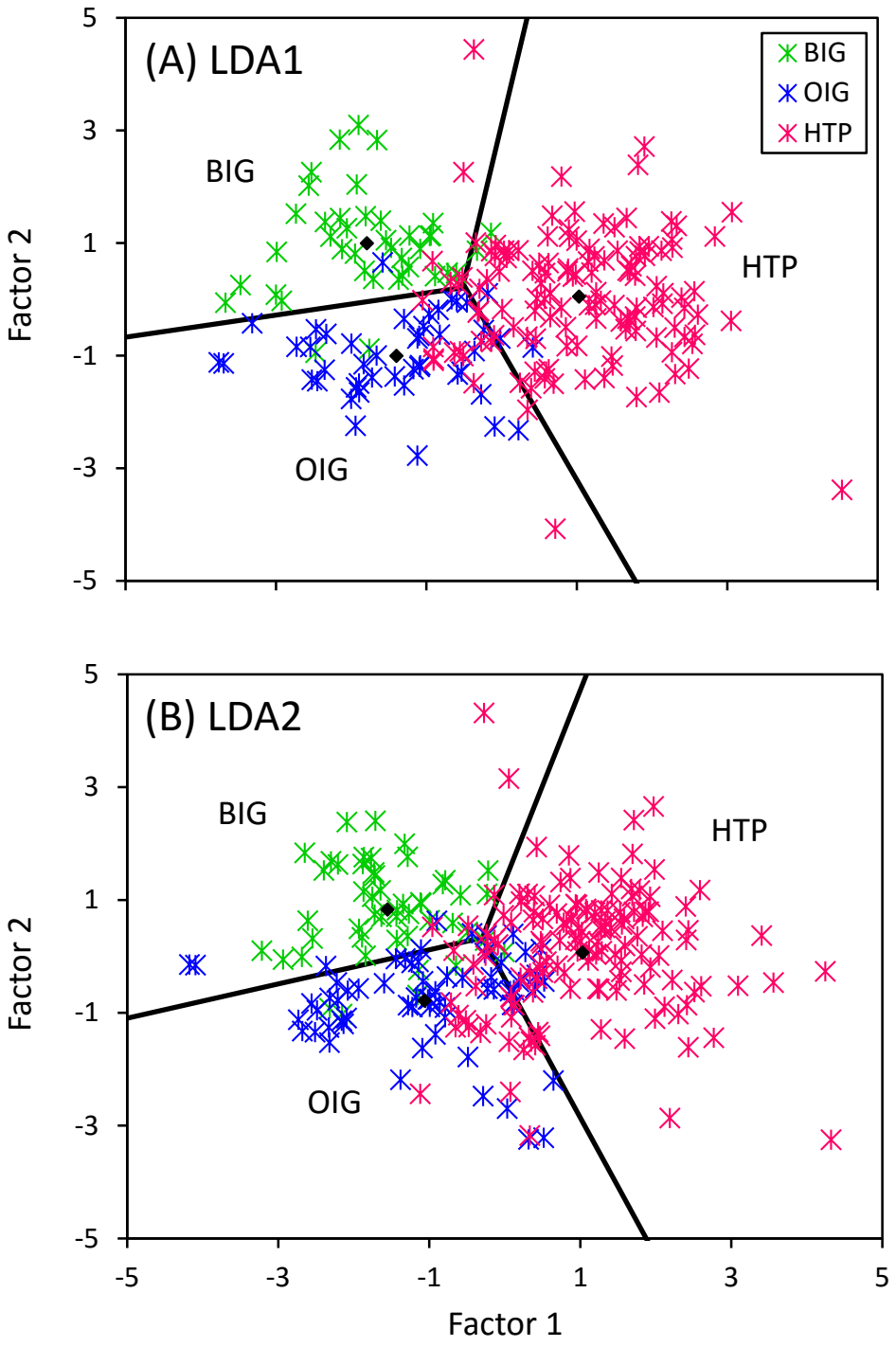

Figure 18. Territorial plots of the discriminant scores for the full MDB1 and MDB2 training datasets for linear discriminant analyses LDA1 (A) and LDA2 (B). Equations for the boundaries between the compositional groups are given in Table 9. Scores of group means indicated as black diamonds in each respective field. Abbreviations: HTP – hydrothermal porphyry, OIG – ore-related igneous, BIG – barren igneous.

Table 9. Equations for field boundaries separating magnetite compositional groups.

A) LDA1	
Between Groups	**Equation**
OIG - BIG	F2 = 0.196*F1 + 0.308
BIG - HTP	F2 = 5.586*F1 + 3.104
HTP - OIG	F2 = -2.305*F1 - 0.903

B) LDA2	
Between Groups	**Equation**
OIG - BIG	F2 = 0.303*F1 + 0.420
BIG - HTP	F2 = 3.385*F1 + 1.335
HTP - OIG	F2 = -2.458*F1 - 0.400

Equations calculated from points equidistant from group means. Field boundaries plotted in Figures 18 and 19. Abbreviations: HTP – hydrothermal porphyry, OIG – ore igneous, BIG – barren igneous.

HTP and OIG compositional fields, which becomes slightly more pronounced in LDA2 (Fig. 18). This overlap could result from potentially similar compositions of early, high-temperature, hydrothermal magnetite and late magmatic magnetite precipitating at the magmatic-hydrothermal transition. Regardless, the derived compositional fields from both analyses show strong potential for identifying magnetite provenance in mineral indicator studies.

Although the territorial plots in Figure 18 appear to be another binary classification of magnetite compositions, they are based on the collective significance of all elements in magnetite subjected to the rigour of statistical methods. This approach shows a significant classification success rate of 91 and 78% for the MDB1 and MDB2 datasets, respectively. Therefore, this classification method can now be confidently applied to magnetite of unknown provenance in till samples surrounding the Mount Polley deposit as a ground-truth test of its effectiveness as an exploration tool.

6.2 Application to the Mount Polley Porphyry Cu-Au Deposit

6.2.1 Identification of Magnetite in Till

The classification methods for magnetite composition derived from discriminant analysis and the discrimination diagrams proposed in previous studies were directly tested using till samples surrounding the Mount Polley porphyry deposit as a ground-truth evaluation. Fifty magnetite grains were analyzed per till sample that was systematically sampled at various locations in the area surrounding the deposit. Twenty sample locations were selected to determine if hydrothermal magnetite from the deposit could be

successfully identified in till, and included samples that were up-ice, down-ice or remote from the deposit (Fig. 3).

For each till sample, magnetite grains were assigned a discriminant score using each of the two sets of linear functions derived for LDA1 and LDA2 in Table 8. A territorial plot of F1 vs. F2 for both analyses with the field boundaries for the compositional groups drawn using the equations from Table 9, allowed for straightforward classification of magnetite grains into one of the three pre-defined groups (Fig. 19). Table 10A,B gives the results of the classification for magnetite along with the relative percentage of hydrothermal grains in each till sample from the area (Appendix B). The discriminant functions of LDA1 identified 71 hydrothermal porphyry magnetite grains in the area, whereas those of LDA2 identified 93 grains. The majority of magnetite grains from each classification plot in the ore igneous (OIG) compositional field using both LDA1 and LDA2 functions, suggesting that the discrimination of ore from barren igneous magnetite is not well constrained.

Magnetite compositions from till were also plotted on the discriminant diagrams proposed in the literature as described in the previous section. The diagrams of Dupuis & Beaudoin (2011) were unable to correctly classify magnetite from Mount Polley and could not identify a sufficient number of porphyry magnetite grains in till (Figs. 12, 13). The Al+Mn vs. Ti+V diagram of Nadoll et al. (2015) was only useful in distinguishing porphyry from skarn magnetite, with no distinction provided for magmatic magnetite (Fig. 14). In contrast the Ti vs. Ni/Cr diagram of Dare et al. (2014) correctly identified all magnetite samples from Mount Polley as hydrothermal. When the discriminant diagram was applied

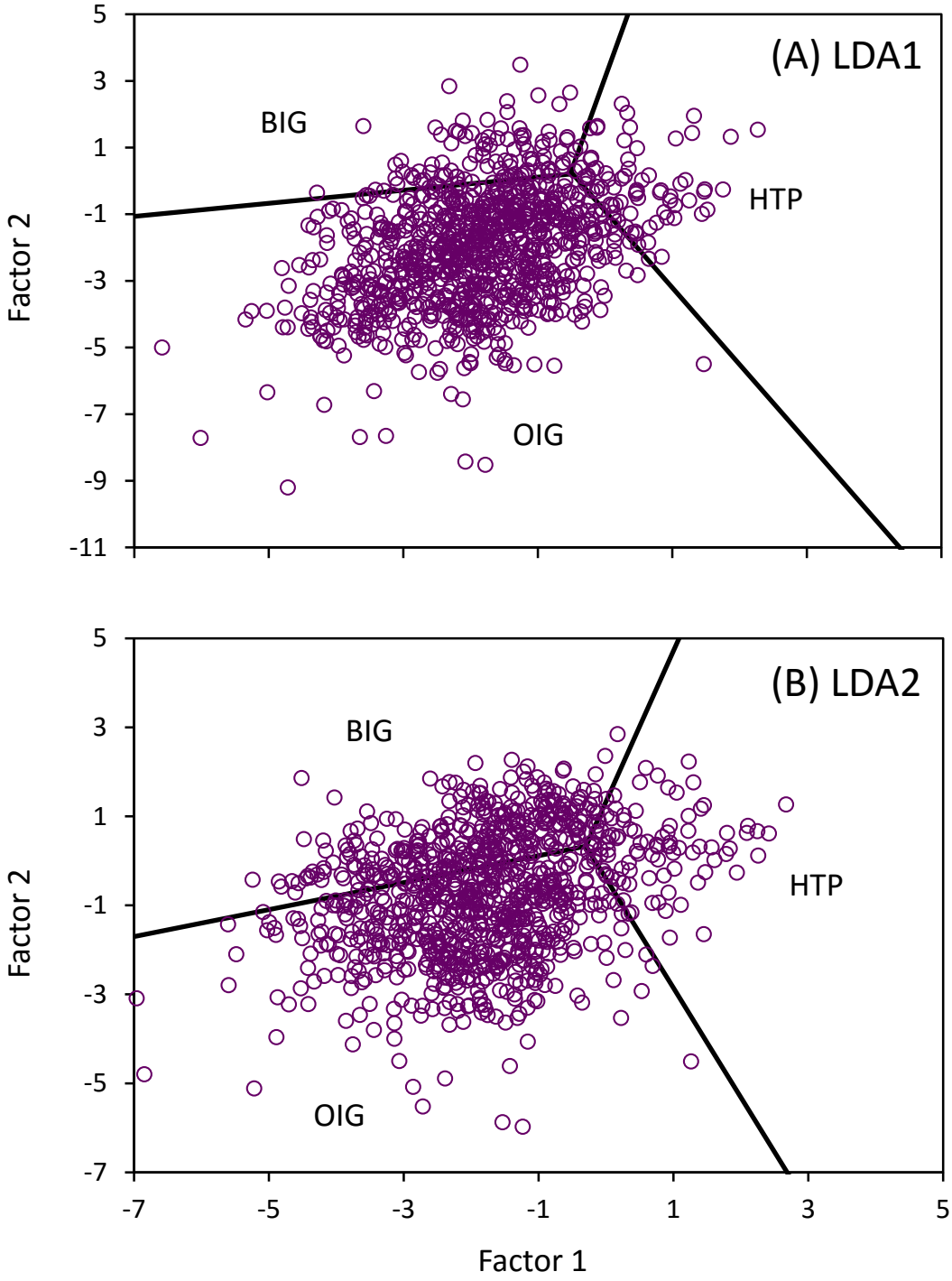

Figure 19. Territorial plots of the discriminant scores for magnetite in till using the linear functions of LDA1 (A) and LDA2 (B). Equations for the boundaries between the compositional groups are given in Table 9. A total of 71 magnetite grains in till are classified as hydrothermal (HTP) using LDA1, whereas 93 magnetite grains are classified as hydrothermal using LDA2. Abbreviations: HTP – hydrothermal porphyry, OIG – ore igneous, BIG – barren igneous.

Table 10. Classification results for magnetite grains in till.

	A) LDA1					B) LDA2				C) Ti vs Ni/Cr diagram			
Till Sample	**n**	**BIG**	**OIG**	**HTP**	**% HTP**	**BIG**	**OIG**	**HTP**	**% HTP**	**n**	**IG**	**HT**	**% HT**
12 PMA 586 A01	68	12	54	2	3	23	40	5	7	12	12	0	0
12 PMA 095 A01	30	1	27	2	7	9	19	2	7	30	27	3	10
12 PMA 083 A01	50	1	48	1	2	8	40	2	4	50	49	1	2
12 PMA 585 A01	50	9	41	0	0	16	33	1	2	50	49	1	2
12 PMA 081 A01	49	10	32	7	14	20	20	9	18	49	38	11	22
12 PMA 088 A01	50	2	47	1	2	15	31	4	8	50	44	6	12
12 PMA 077 A01	50	3	46	1	2	11	39	0	0	50	47	3	6
12 PMA 087 A01	50	3	47	0	0	14	36	0	0	50	47	3	6
12 PMA 080 A01	42	3	26	13	31	12	18	12	29	43	30	13	30
12 PMA 578 A01	50	11	37	2	4	16	30	4	8	50	44	6	12
12 PMA 575 A01	50	1	48	1	2	20	28	2	4	50	49	1	2
12 TFE 089 A01	50	6	42	2	4	16	32	2	4	50	45	5	10
12 PMA 101 A02	50	4	38	8	16	13	24	13	26	50	42	8	16
12 TFE 078 A01	50	13	36	1	2	28	22	0	0	50	48	2	4
12 PMA 094 A01	49	3	35	11	22	10	27	12	24	49	43	6	12
12 TFE 102 A01	49	8	35	6	12	21	24	4	8	49	43	6	12
12 PMA 098 A01	50	5	36	9	18	18	20	12	24	50	46	4	8
12 PMA 566 A01	44	4	39	1	2	13	29	2	5	47	43	4	9
12 PMA 071 A01	49	1	46	2	4	12	34	3	6	50	48	2	4
12 PMA 574 A01	49	3	45	1	2	21	24	4	8	50	42	8	16
Total	979	103	805	**71**	7	316	570	**93**	9	929	892	**93**	10

Abbreviations: n – total number of grains, HTP – hydrothermal porphyry, OIG – ore igneous, BIG – barren igneous, IG – igneous, HT - hydrothermal. Note that the number of grains is significantly reduced for Ti vs. Ni/Cr classification of sample 12 PMA 586 A01 since Cr was not selected for measurement during one analytical run.

to magnetite from till, 93 hydrothermal magnetite grains were identified, similar to the classification by the LDA2 model (Fig. 15, Table 10C).

As a comparison, the percentage of hydrothermal magnetite grains identified in each till sample using the three different methods of classification are plotted in Figure 20. The proportion of hydrothermal grains in till are generally consistent between the LDA1 and LDA2 models, with the latter yielding slightly higher percentages in most samples (Fig. 20A). In contrast, there is less agreement between the LDA models and the Ti-Ni/Cr discrimination diagram as indicated by significant scatter in the data (Figs. 20B, C).

Magnetite grains that were identified as hydrothermal in origin using the discriminant functions of LDA1 and LDA2 were plotted on the Ti-Ni/Cr diagram (Fig. 21). The majority of these magnetite grains plot at much lower Ni/Cr values and some slightly higher Ti contents than what is proposed for hydrothermal magnetite by Dare et al. (2014). A significant number of grains that were classified as hydrothermal by Dare et al. (2014) were not similarly identified as hydrothermal in the discriminant analysis since only a small number of grains coincide with the proposed hydrothermal field. There is discrepancy between the results of the discriminant analyses and the hydrothermal field by Dare et al. (2014). The rigorous statistical method of discriminant analysis is expected to provide a more robust determination of magnetite provenance based on the larger number of variables used in the analysis, as well as the demonstrated successful classification of independent test data in the previous section.

The textures of hydrothermal magnetite grains were also examined to determine if they were potentially useful as a petrographic discrimination tool. The majority of hydrothermal magnetite grains in till showed no exsolution, but the proportion varied with

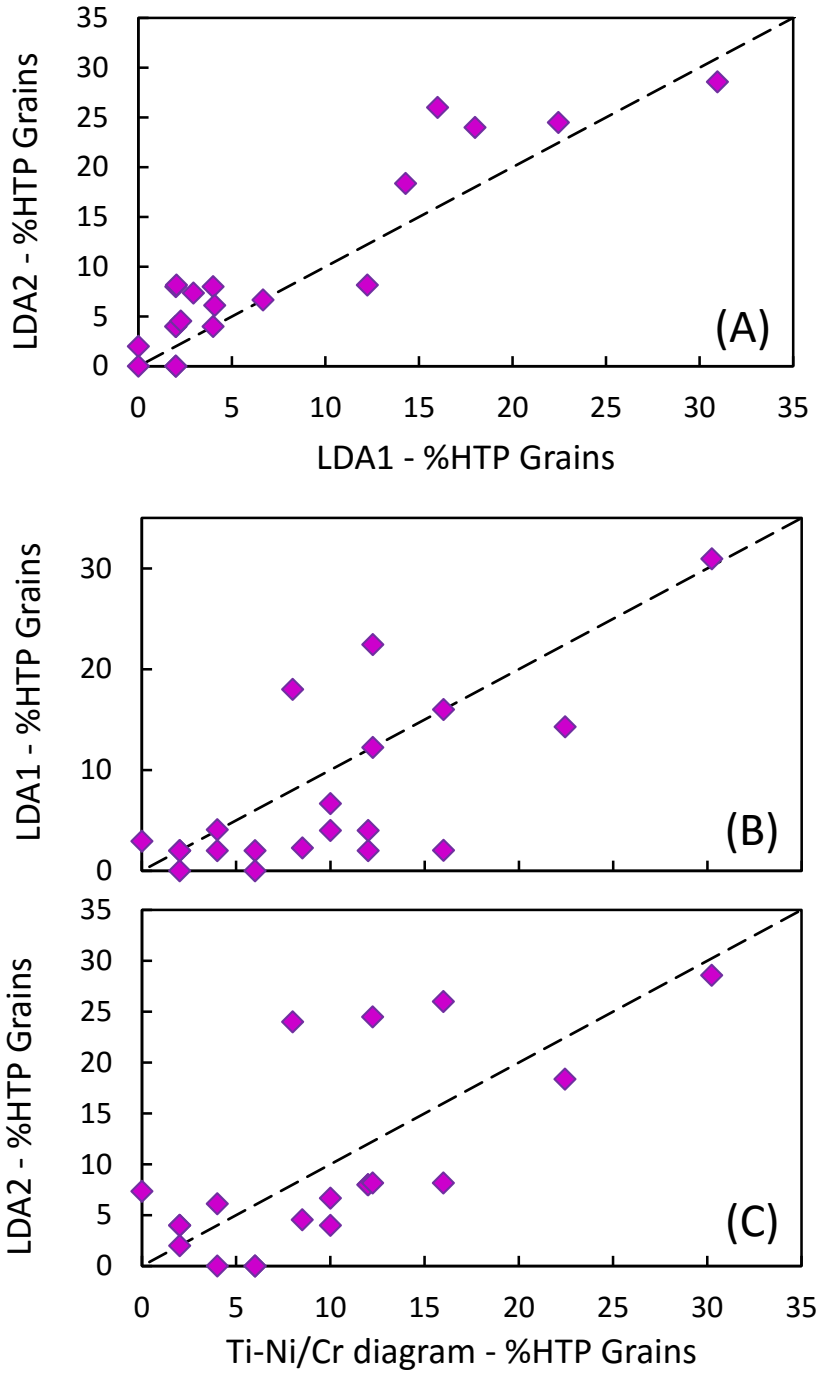

Figure 20. The percentage of hydrothermal porphyry (HTP) magnetite grains identified in each till sample using the three different methods of classification. The proportion of HTP grains in till are generally consistent between the LDA1 and LDA2 models (A), whereas there is less agreement between the LDA models and the Ti-Ni/Cr discrimination diagram (B,C).

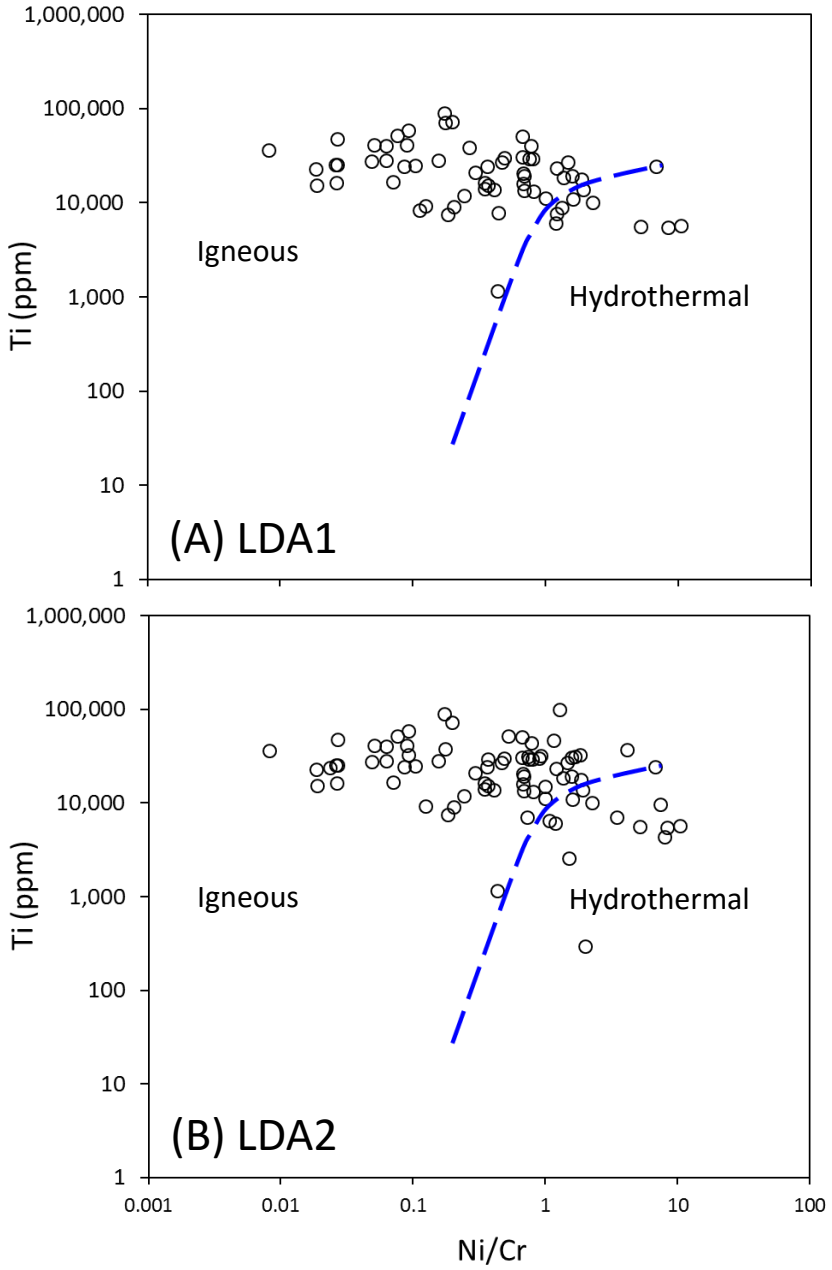

Figure 21. Hydrothermal magnetite grains determined by A) LDA1 and B) LDA2 are plotted on the Ti vs. Ni/Cr diagram with igneous and hydrothermal fields from Dare et al. (2014). Most magnetite grains from LDA do not coincide with the proposed hydrothermal field illustrating the discrepancy between the methods of classification for magnetite compositions.

the classification method: 58% for LDA1, 66% for LDA2 and 74% for the Ti-Ni/Cr diagram. The binary diagram preferentially selects low-Ti magnetite due to the upper Ti limit imposed on the hydrothermal field by Dare et al. (2014), therefore, grains identified as hydrothermal by this method have insufficient Ti contents to promote exsolution resulting in a large proportion of homogeneous grains. Although hydrothermal magnetite typically contains relatively low Ti contents, ilmenite exsolution lamellae in magnetite from porphyry systems has been documented at several localities (e.g., Celis et al., 2014; Nadoll et al., 2015; Canil et al., in press). Additionally, magmatic magnetite from felsic plutonic or rapidly cooled volcanic rocks are commonly absent of exsolution (e.g., Frost & Lindsley, 1991; Grigsby, 1990; Dare et al., 2014). Evidently, the absence of exsolution in magnetite is not a reliable indication of its provenance from hydrothermal porphyry systems. Other textural features such as presence of inclusions or alteration assemblage were not directly linked to magnetite classification in till. For example, sulphide inclusions were present in some magnetite grains, however, the bulk of these grains were classified as ore-related igneous and only a small number (~5 grains) were classified as hydrothermal in origin.

6.2.2 Magnetite as an Indicator Mineral at Mount Polley

To determine the extent that magnetite can serve as an effective indicator in mineral exploration, the dispersal of hydrothermal magnetite grains was examined with respect to the Mount Polley porphyry deposit. The percentage of hydrothermal magnetite grains in each till sample as determined by LDA1, LDA2 and the Ti-Ni/Cr discriminant diagram of Dare et al. (2014) were plotted on the geological map, with symbol size proportional to percentage hydrothermal magnetite grains (Figs. 22-24). From the results of all three

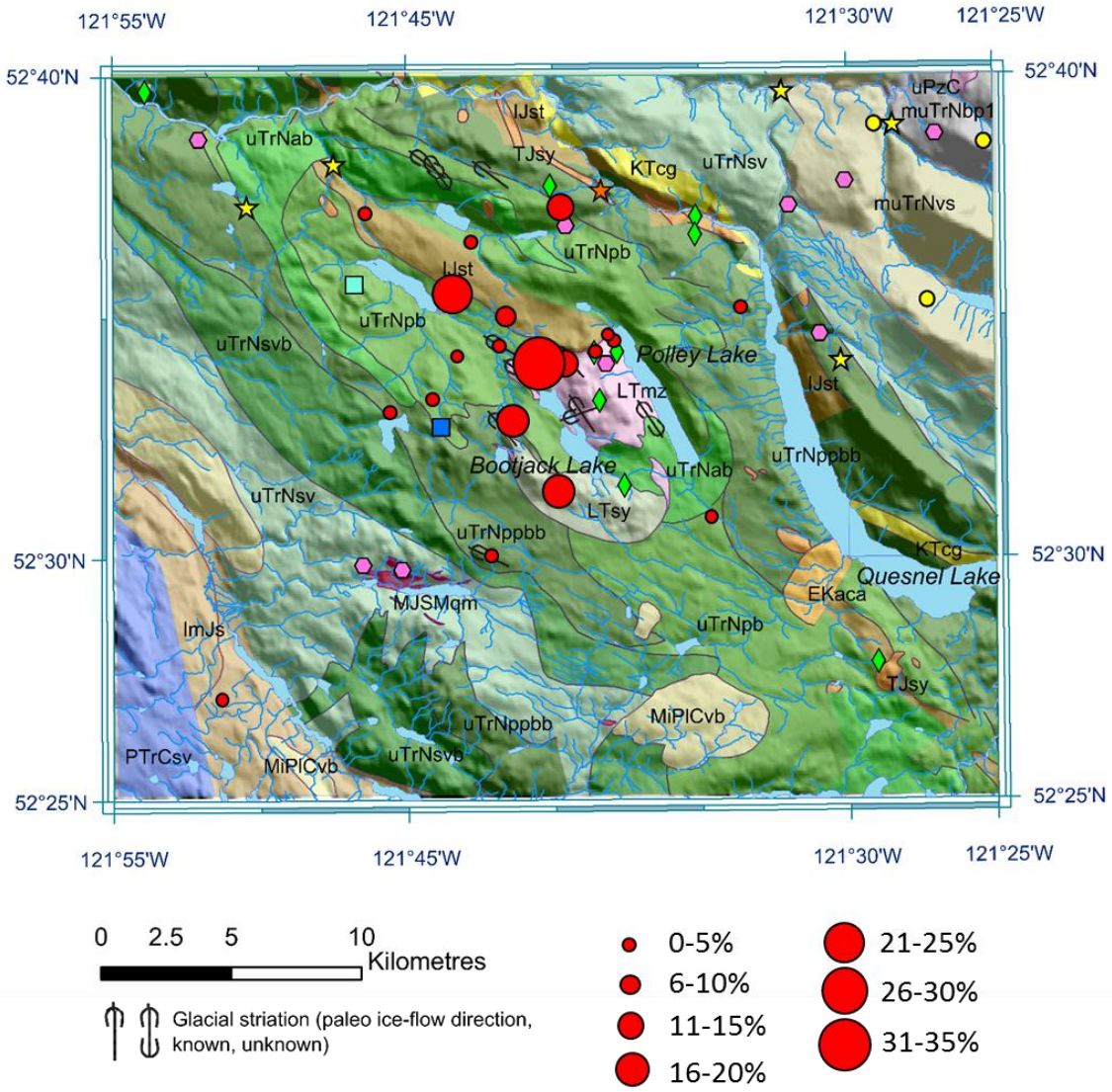

Figure 22. The percentage of hydrothermal porphyry magnetite (HTP) grains in each till sample as determined by the LDA1 model plotted on the geological map for each sample location. Symbol size is proportional to percentage HTP magnetite grains in the sample. Modified from Plouffe et al. (2013a). Bedrock geology from Logan et al. (2010) – legend in Figure 2.

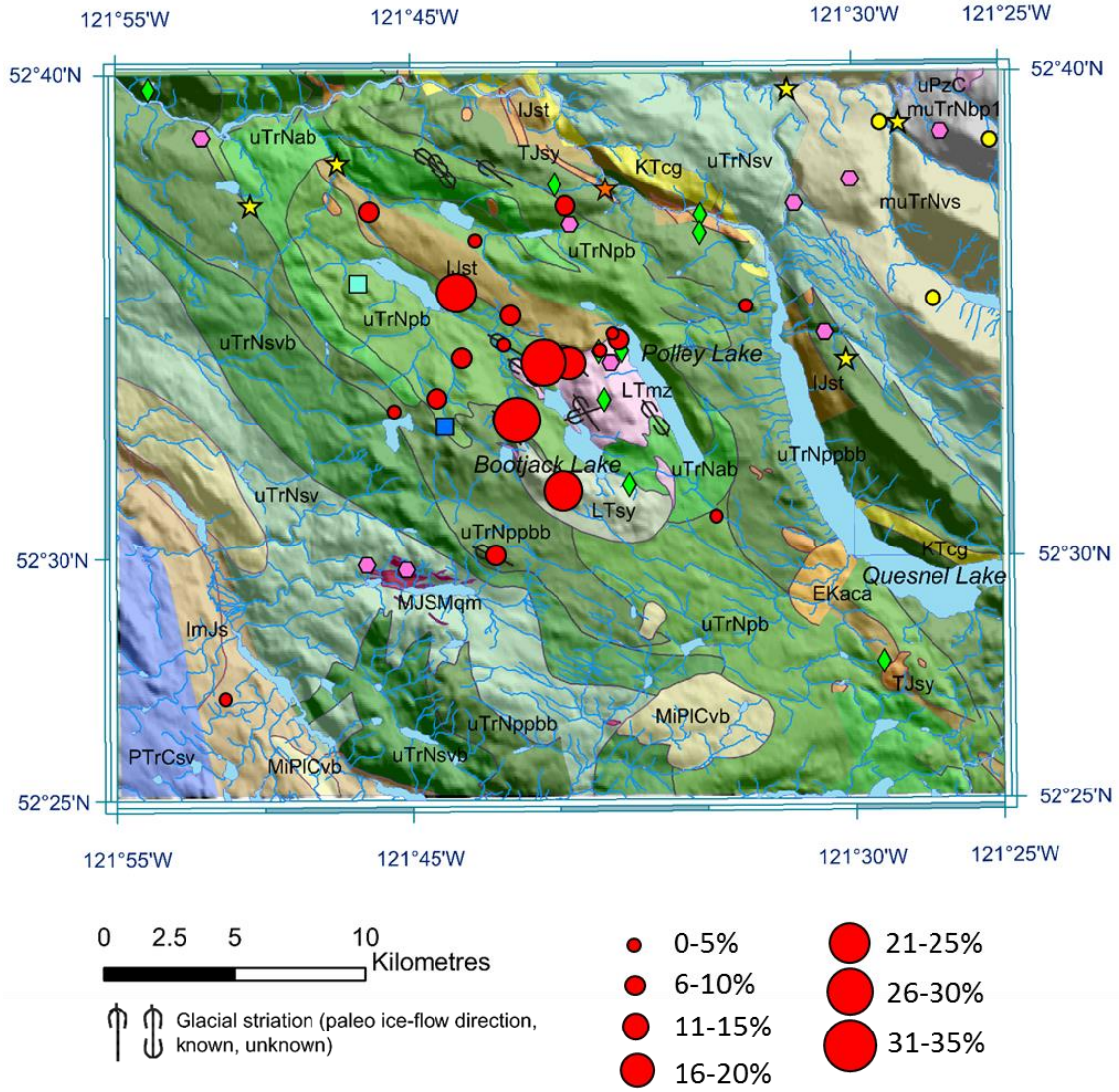

Figure 23. The percentage of hydrothermal porphyry magnetite (HTP) grains in each till sample as determined by the LDA2 model plotted on the geological map for each sample location. Symbol size is proportional to percentage HTP magnetite grains in the sample. Modified from Plouffe et al. (2013a). Bedrock geology from Logan et al. (2010) – legend in Figure 2.

.

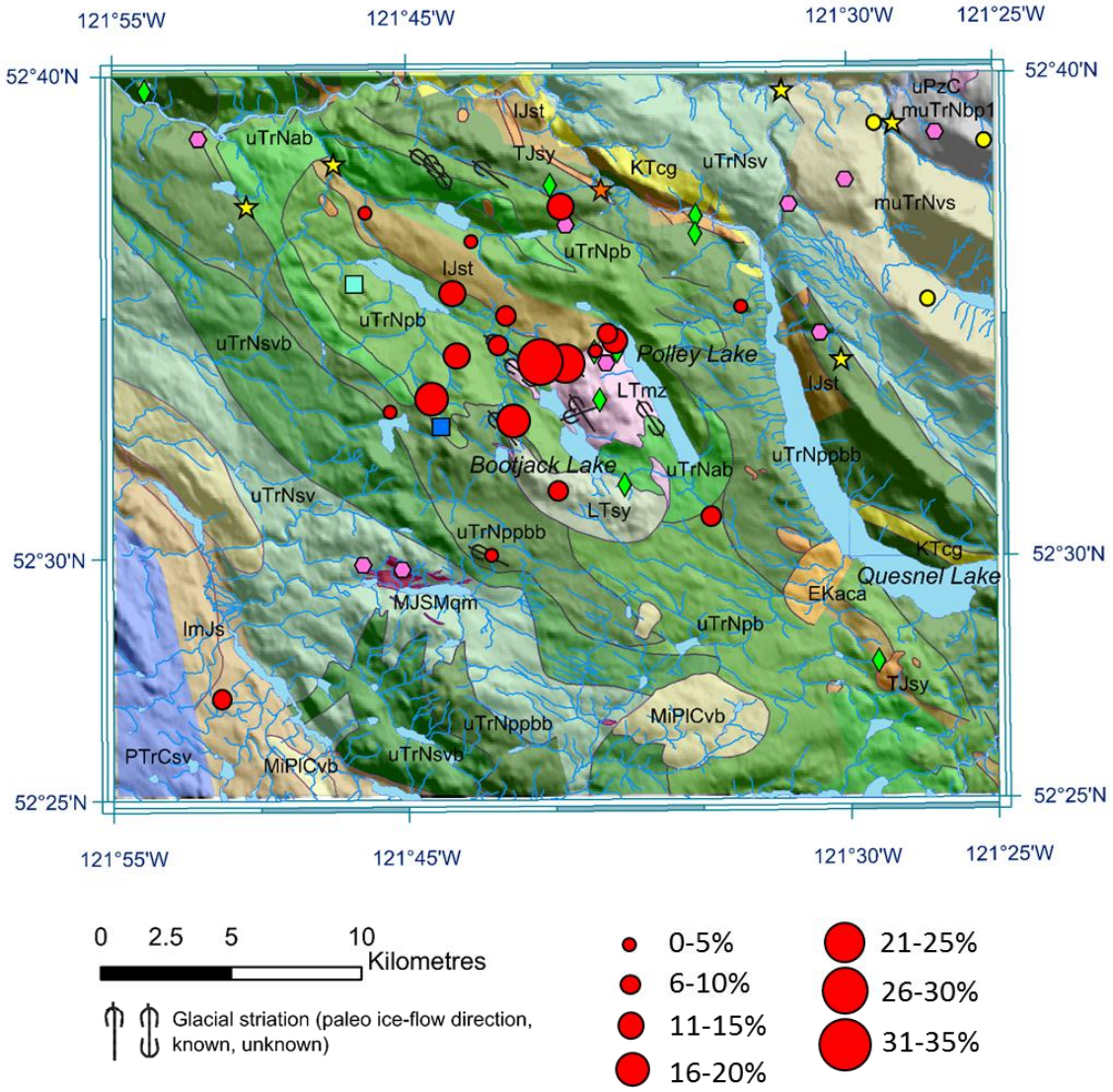

Figure 24. The percentage of hydrothermal (HT) magnetite grains in each till sample as determined by the Ti-Ni/Cr discrimination diagram of Dare et al. (2014) plotted on the geological map for each sample location. Symbol size is proportional to percentage hydrothermal magnetite grains in the sample. Modified from Plouffe et al. (2013a). Bedrock geology from Logan et al. (2010) – legend in Figure 2.

classification methods, samples with anomalous concentrations generally contain more than 10% hydrothermal magnetite grains, whereas below this amount is considered to be the regional background signal.

Classification of magnetite by the LDA1 discriminant functions identified six till samples with anomalous concentrations of hydrothermal magnetite grains (Table 10). Five of these samples were similarly identified with the LDA2 classification and occur along a northwest trending path that begins immediately southwest of the deposit with the furthest anomalous sample occurring approximately 4 km northwest of Mount Polley (Figs. 22, 23). To the west the anomaly is detected ~2.5 km from the deposit, but till samples at 5 km distance from the deposit are within the background range.

Northwest transport of magnetite is consistent with the dominant ice-flow direction interpreted in the study area and has also been documented using several ore-related and pathfinder elements, as well as a number of ore and alteration minerals at Mount Polley (Hashmi, 2015). The transport of magnetite grains several kilometers west-southwest of the deposit is consistent with the observations of Hashmi (2015). She found chalcopyrite, gold, and epidote grains in till samples west-southwest of the deposit. This bidirectional transport of material is characteristic of glacial dispersal whereby material was initially transported by the earlier ice-flow movement to the west-southwest during glacial advancement from the Cariboo Mountains, followed by reworking and transport of debris by ice-flow to the northwest at glacial maximum (Parent et al., 1996).

The Ti vs. Ni/Cr method of magnetite classification proposed by Dare et al. (2014) identified the same quantity of hydrothermal magnetite grains as the LDA2 discriminant functions, but the grains identified using the Ti-Ni/Cr diagram are distributed over a larger

number of till samples (Table 10). There is still an apparent bidirectional movement of material from the deposit to the west and northwest, but the dispersal of hydrothermal magnetite grains over a larger number of samples results in a more diffuse anomaly compared to that produced from the LDA classifications (Fig. 24). The four till samples with the greatest proportion of hydrothermal magnetite grains identified by the Ti-Ni/Cr diagram occur in a path trending west from the deposit to a distance of 5 km, much further than that determined by the LDA classifications, and by Hashmi (2015) for chalcopyrite, gold and epidote in till. Hydrothermal magnetite grains would be primarily transported to the northwest based on the dominant ice-flow trajectory interpreted at Mount Polley. In contrast, classification using the Ti-Ni/Cr diagram shows hydrothermal magnetite from the deposit has been transported greater distances to the west than to the northwest, raising suspicion on the validity of this method.

All till samples with anomalous concentrations of hydrothermal magnetite grains can be directly traced to the Mount Polley porphyry deposit based on ice-flow directions in the study area, with the exception of one till sample (12 TFE 102 A01) that occurs 5 km due north of the deposit (Figs. 22, 24). This sample contains 12% hydrothermal magnetite grains identified by both LDA1 and Ti vs. Ni/Cr discrimination methods (Table 10). Hydrothermal magnetite grains at this location are not likely to be derived from the Mount Polley deposit based on the remoteness of the sample. There are, however, numerous other porphyry mineral occurrences reported in the study area that could be the source for hydrothermal magnetite grains (Fig. 2). Given the ice-flow history of the region, proximal porphyry mineralization reported in syenite and monzonite intrusions (Fig. 2 - unit TJsy) that outcrop to the north and east of the sample are a more likely source for these grains. It

would appear that other alkalic intrusions in the area may be prospective targets for further exploration.

7. Conclusions

7.1 Summary

Previous studies have indicated the potential for magnetite chemistry to act as a valuable indicator for mineralized hydrothermal systems (McQueen & Cross, 1998; Carew, 2004; Kamvong et al., 2007; Dupuis & Beaudoin, 2011; Nadoll et al., 2012, 2014, 2015; Huang et al., 2014; Dare et al., 2014; Chen et al., 2015; Canil et al., in press). These studies, however, lacked any direct application, or test, to exploration of a porphyry deposit. The overall goal of this research was to first re-evaluate the chemical signature of hydrothermal magnetite from mineralized porphyry systems, and then directly test that approach as an exploration method on till sampled around a known porphyry Cu-Au deposit at Mount Polley.

Laser ablation-ICP-MS was performed on detrital magnetite grains (n = 985) from 20 till samples collected over an area of ~700 km^2 surrounding the Mount Polley deposit. This region was chosen because the glacial history has been reasonably constrained (Plouffe et al., 2013; Hashmi, 2015) and the composition of magnetite from mineralized and intrusive lithologies at the deposit was recently studied (Canil et al., in press). The LA-ICP-MS method offers lower detection limits than EMP and was most efficient at homogenizing primary magnetite compositions in grains showing exsolution. Calibration of LA-ICP-MS data was most effective using the AYCF method, which obtained consistent results for all elements analyzed. The AYCF method eliminated the use of an internal standard by another analytical method (commonly EMP), thus making for a more efficient protocol when analyzing large numbers of grains in an indicator mineral exploration study.

Hydrothermal magnetite from porphyry deposits exhibits a variation in minor and trace element contents of up to 2-3 orders of magnitude (e.g., Dupuis & Beaudoin, 2011; Nadoll et al., 2015; Canil et al., in press). This study showed how previously proposed binary discriminant diagrams are of limited use in distinguishing hydrothermal magnetite with the exception of the Ti-Ni/Cr diagram of Dare et al. (2014). Caution must be taken when interpreting magnetite chemistry using certain elements affected by secondary processes such as sphenitization (for Si and Ca), which was a relatively common phenomenon observed in detrital magnetite from till.

As an alternative method for classifying magnetite compositions, this study employed linear discriminant analysis (LDA) to uniquely identify hydrothermal magnetite using a more rigorous statistical approach than previously proposed. Linear discriminant analysis was successfully performed on magnetite compositions from various porphyry deposits and barren igneous rocks, achieving 91% successful classification on test data using Mg, Al, V, Mn, Co and Ni for LDA1 (n = 218), and 78% success using Mg, Al, Ti, V, Mn, Co and Ni for LDA2 (n = 253).

The ground-truth application of the discriminant models and the Ti-Ni/Cr diagram was performed on magnetite in till from the Mount Polley area. A significant number (7-9%) of magnetite grains in till were identified as hydrothermal in origin. The classification results from the LDA1 and LDA2 models were generally consistent, but when compared to that of the Ti-Ni/Cr diagram, significant discrepancies occur between the proportions of hydrothermal magnetite grains at each till sample location.

The dispersal of hydrothermal magnetite in till was found to coincide with deposit location and the interpreted ice-flow history initially to the west-southwest, followed by

northwest transport. Anomalous values of hydrothermal magnetite were detected in samples up to 2.5 km west-southwest and 4 km northwest of the deposit using the LDA models developed in this study. In contrast, the dispersal of hydrothermal magnetite grains in till classified using the Ti-Ni/Cr diagram is more diffuse. Anomalous concentrations of hydrothermal grains in till are found to occur at greater distance west of the deposit using the binary plot, inconsistent with the LDA models of this study and the dispersal of deposit-derived chalcopyrite, gold and epidote grains in till surrounding Mount Polley (Hashmi, 2015).

7.2 Future Work & Recommendations

The success of the LDA models in the Mount Polley area indicates that magnetite has a strong potential as an effective indicator in mineral exploration for porphyry systems. The LDA models used to classify magnetite was based on samples of known sources in igneous rocks and porphyry deposits from 16 locations. Further refinement of the LDA models would be possible with compilation of new magnetite compositions from a greater number of known deposits in other regions. Since magnetite precipitates during virtually all stages of hydrothermal alteration in porphyry Cu deposits, more study is needed to determine if the chemistry of hydrothermal magnetite changes with the different stages of alteration. Future experimental work on element partitioning in magnetite under the lower-temperature conditions of hydrothermal environments (<800°C) would provide a better understanding of the mechanisms and processes behind the wide compositions observed in hydrothermal magnetite. The misclassification of most igneous magnetite in till as derived from ore-related igneous rock (OIG) suggests that discrimination between ore-related and

barren igneous rock (BIG) may not be very definitive, or that the training dataset used in the LDA may not have been an accurate representation of all igneous magnetite compositions. The compositional differences between ore-related and barren igneous magnetite needs to be further examined because ore-related grains in till can provide an additional exploration tool for porphyry systems where mineralization has not yet been exposed at the surface.

Optimization of the technique for mineral exploration could be performed by reducing the number of magnetite grains analyzed per till sample. In this study, the number of analyses per sample was arbitrarily set at 50 and was able to detect anomalous concentrations of hydrothermal magnetite in till up to 4 km from the deposit. Significant reduction in the number of grains analyzed per till sample will increase the margin of error, which can lead to misrepresentation of the magnetite population in each sample. This is especially important for distal samples down-ice of a deposit where the number of hydrothermal magnetite grains in till becomes scarce. Therefore, significant reduction in the number of analyses is not recommended, however, the optimum amount required to ensure a target of viable size can be generated should be investigated further.

Electron microprobe analysis may be a faster and more cost effective analytical technique than LA-ICP-MS to analyze large numbers of indicator mineral grains in till samples. Nevertheless, this study shows that LA-ICP-MS is required to ensure that all trace elements imperative for use in the discriminant models (e.g., Ni and Co) for magnetite can be consistently measured to low detection limits. The LDA models showed that a smaller menu of elements, such as those amenable to routine EMP analysis in magnetite (Mg, Al, Ti, V, Mn) does not show effective discriminating power. The use of EMP is not required

if the AYCF method of internal standardless data reduction can be applied, as was shown in this study.

Bibliography

Allan, J.F., Sack, R.O. & Batiza, R. (1988): Cr-rich spinels as petrogenetic indicators: MORB-type lavas from the Lamont seamount chain, eastern Pacific; *American Mineralogist,* vol. 73, p. 741-753.

Anderson, R.G., Plouffe, A., Ferbey, T. & Dunn, C.E. (2012): The search for surficial expressions of buried Cordilleran porphyry deposits: background and progress in a new TGI-4 activity in the southern Canadian Cordillera; Geological Survey of Canada, Current Research 2012-7, 15 pages.

Atchison, J. (1986): The statistical analysis of compositional data; Chapman and Hall, New York, USA, 416 pages.

Averill, S.A. (2001): The application of heavy indicator mineralogy in mineral exploration with emphasis on base metal indicators in glaciated metamorphic and plutonic terrains; *in* Drift Exploration in Glaciated Terrain, M.B. McClenaghan, P.T. Bobrowsky, G.E.M. Hall & S.J. Cook (eds.), Geological Society, London, Special Publications, no. 185, p. 69-81.

Barnes, S.J. & Roeder, P.L. (2001): The range of spinel compositions in terrestrial mafic and ultramafic rocks; *Journal of Petrology*, vol. 42, no. 12, p. 2279-2302.

Bath, A.B. & Logan, J.M. (2006): Petrography and geochemistry of the Late Triassic Bootjack Stock (NTS 093A/12), south-central British Columbia; *in* Geological Fieldwork 2005, BC Ministry of Energy and Mines, Paper 2006-1, p. 5-19.

Boutroy, E., Dare, S.A.S., Beaudoin, G., Barnes, S.-J. & Lightfoot, P.C. (2014): Magnetite composition in Ni-Cu-PGE deposits worldwide: application to mineral exploration, *Journal of Geochemical Exploration*, vol. 145, p. 64-81.

Buddington, A.F. & Lindsley, D.H. (1964): Iron-titanium oxide minerals and synthetic equivalents; *Journal of Petrology*, vol. 5, no. 2, p. 310-357.

Canil, D., Grondahl, C., Lacourse, T. & Pisiak, L.K. (in press): Trace elements in magnetite from porphyry Cu-Mo-Au deposits in British Columbia, Canada; *Ore Geology Reviews,* 13 pages, http://dx.doi.org/10.1016/j.oregeorev.2015.10.007.

Carew, M.J. (2004): Controls on Cu-Au mineralization and Fe-oxide metasomatism in the Eastern Fold Belt, NW Queensland, Australia; PhD Thesis, James Cook University, Townsville, Australia, 308 pages.

Celis, M.A., Bouzari, F., Bissig, T., Hart, C.J.R. & Ferbey, T. (2014). Petrographic characteristics of porphyry indicator minerals from alkalic porphyry copper-gold

deposits in south-central British Columbia (NTS 092, 093); *in* Geoscience BC Summary of Activities 2013, Geoscience BC, Report 2014-1, p. 53-62.

Chayes, F. (1960): On correlation between variables of constant sum; *Journal of Geophysical Research*, vol. 65, no. 12, p. 4185-4193.

Chen, W.T., Zhou, M.-F. & Gao, J.-F. (2015): Geochemistry of magnetite from Proterozoic Fe-Cu deposits in the Kangdian metallogenic province, SW China; *Mineralium Deposita*, 15 pages, http://dx.doi.org/10.1007/s00126-014-0575-7.

Chou, I. & Eugster, H.P. (1977): Solubility of magnetite in supercritical chloride solutions; *American Journal of Science*, vol. 277, p. 1296-1314.

Colpron, M. & Nelson, J.L. (2011): A digital atlas of terranes for the northern Cordillera; British Columbia Ministry of Energy and Mines, BCGS GeoFile 2011-11.

Dare, S.A.S., Barnes, S.J. & Beaudoin, G. (2012): Variation in trace element content of magnetite crystallized from a fractionating sulfide liquid, Sudbury, Canada: implications for provenance discrimination; *Geochimica et Cosmochimica Acta*, vol. 88, p. 27-50.

Dare, S.A.S., Barnes, S.J., Beaudoin, G., Méric, J., Boutroy, E. & Potvin-Doucet, C. (2014): Trace elements in magnetite as petrogenetic indicators; *Mineralium Deposita*, vol. 49, no. 7, p. 785-796.

Davis, J.C. (2002): Statistics and data analysis in geology, 3rd edition; John Wiley & Sons, New York, USA, 638 pages.

Dick, H.J.B. & Bullen, T. (1984): Chromian spinel as a petrogenetic indicator in abyssal and alpine-type peridotites and spatially associated lavas; *Contributions to Mineralogy and Petrology*, vol. 86, p. 54-76.

Dickinson, W.R. (2004): Evolution of the North American Cordillera; *Annual Review of Earth and Planetary Sciences*, vol. 32, p. 13-45.

Dupuis, C. & Beaudoin, G. (2011): Discriminant diagrams for iron oxide trace element fingerprinting of mineral deposit types; *Mineralium Deposita*, vol. 46, p. 319-335.

Ferbey, T., Plouffe, A. & Anderson, R.G. (2014): An integrated approach to search for buried porphyry-style mineralization in central British Columbia using geochemistry and mineralogy: a TGI-4 project; Geological Survey of Canada, Current Research 2014-2, 12 pages.

Fraser, T.M., Godwin, C.I., Thompson, J.F.H. & Stanley, C.R. (1992): Geology and alteration of the Mount Polley alkalic porphyry copper-gold deposit, British

Columbia; *in* Geological Fieldwork 1992, BC Ministry of Energy and Mines, BC Geological Survey, Paper 1993-1, p. 295-300.

Fraser, T.M. (1994): Hydrothermal breccias and associated alteration of the Mount Polley copper-gold deposit (93A/12); *in* Geological Fieldwork 1993, BC Ministry of Energy and Mines, BC Geological Survey, Paper 1994-1, p. 259-267.

Frost, B.R. (1991): Magnetic petrology: factors that control the occurrence of magnetite in crustal rocks; *in* Oxide Minerals: Petrologic and Magnetic Significance, D.H. Lindsley (ed.), Mineralogical Society of America, Reviews in Mineralogy, vol. 25, p. 489-509.

Frost, B.R. & Lindsley, D.H. (1991): Occurrence of iron-titanium oxides in igneous rocks; *in* Oxide Minerals: Petrologic and Magnetic Significance, D.H. Lindsley (ed.), Mineralogical Society of America, Reviews in Mineralogy, vol. 25, p. 433-468.

Grigsby, J.D. (1990): Detrital magnetite as a provenance indicator; *Journal of Sedimentary Petrology*, vol. 60, no. 6, p. 940-951.

Haggerty, S.E. (1976): Opaque mineral oxides in terrestrial igneous rocks; *in* Oxide Minerals, D. Rumble III (ed.), Mineralogical Society of America, Reviews in Mineralogy, vol. 3, p. HG101-HG300.

Haggerty, S.E. (1991): Oxide textures – a mini-atlas; *in* Oxide Minerals: Petrologic and Magnetic Significance, D.H. Lindsley (ed.), Mineralogical Society of America, Reviews in Mineralogy, vol. 25, p. 129-137.

Hashmi, S. (2015): Quaternary geology and drift prospecting in the Mount Polley region (NTS 093A); MSc Thesis, Simon Fraser University, Vancouver, Canada, 165 pages.

Huang, X., Qi, L. & Meng, Y. (2014): Trace element geochemistry of magnetite from the Fe(-Cu) deposits in the Hami Region, Eastern Tianshan Orogenic Belt, NW China; *Acta Geologica Sinica*, vol. 88, no. 1, p. 176-195.

Irvine, T.N. (1965): Chromian spinel as a petrogenetic indicator – part 1: theory; *Canadian Journal of Earth Sciences*, vol. 2, p. 648-672.

Irvine, T.N. (1967): Chromian spinel as a petrogenetic indicator – part 2: petrologic application; *Canadian Journal of Earth Sciences*, vol. 4, p. 71-103.

Kamvong, T., Zaw, K. & Siegele, R. (2007): PIXE/PIGE microanalysis of trace elements in hydrothermal magnetite and exploration significance: a pilot study; 15th Australian Conference on Nuclear and Complementary Techniques of Analysis

and 9th Vacuum Society of Australia Congress, University of Melbourne, Melbourne, Australia, 4 pages.

Levson, V.M. (2001): Regional till geochemical surveys in the Canadian Cordillera: sample media, methods and anomaly evaluation; *in* Drift Exploration in Glaciated Terrain, M.B. McClenaghan, P.T. Bobrowsky, G.E.M. Hall & S.J. Cook (eds.), Geological Society, Special Publication, vol. 85, p. 45-68.

Lindsley, D.H. (1976): The crystal chemistry and structure of oxide minerals as exemplified by the Fe-Ti oxides; *in* Oxide Minerals, D. Rumble III (ed.), Mineralogical Society of America, Reviews in Mineralogy, vol. 3, p. L1-L60.

Liu, Y., Hu, Z., Gao, S., Günther, D., Xu, J., Gao, C. & Chen, H. (2008): In situ analysis of major and trace elements of anhydrous minerals by LA-ICP-MS without applying an internal standard; *Chemical Geology*, vol. 257, p. 34-43.

Logan, J.M. & Mihalynuk, M.G. (2005): Regional geology and setting of the Cariboo, Bell, Springer and Northeast porphyry Cu-Au zones at Mount Polley, south-central British Columbia; *in* Geological Fieldwork 2004, BC Ministry of Energy and Mines, BC Geological Survey, Paper 2005-1, p. 249-270.

Logan, J.M., Mihalynuk, M.G., Ullrich, T. & Friedman, R.M. (2007): U-Pb ages of intrusive rocks and $^{40}Ar/^{39}Ar$ plateau ages of copper-gold-silver mineralization associated with alkaline intrusive centres at Mount Polley and the Iron Mask Batholith, southern and central British Columbia; *in* Geological Fieldwork 2006, BC Ministry of Energy and Mines, BC Geological Survey, Paper 2007-1, p. 93-116.

Logan, J.M., Schiarizza, P., Struik, L.C., Barnett, C., Nelson, J.L., Kowalczyk, P., Ferri, F., Mihalynuk, M.G., Thomas, M.D., Gammon, P., Lett, R., Jackaman, W. & Ferbey, T. (2010): Bedrock geology of the QUEST map area, central British Columbia; British Columbia Geological Survey, Geoscience Map 2010-1, Geoscience BC Report 2010-5 and Geological Survey of Canada, Open File 6476.

Longerich, H., Jackson, S.E. & Günther, D. (1996): Laser ablation inductively coupled plasma mass spectrometric transient signal data acquisition and analyte concentration calculation; *Journal of Analytical Atomic Spectrometry*, vol. 11, p. 899-904.

Mellini, M., Rumori, C. & Viti, C. (2005): Hydrothermally reset magmatic spinels in retrograde serpentinites: formation of “ferritchromit” rims and chlorite aureoles; *Contributions to Mineralogy and Petrology*, vol. 149, p. 266-275.

McQueen, K.G. & Cross, A.J. (1998): Magnetite as a geochemical sampling medium: application to skarn deposits; *The State of the Regolith*, Geological Society of Australia, Special Publication, vol. 20, p. 194-199.

Mortensen, J.K., Ghosh, D.K. & Ferri, F. (1995): U-Pb geochronology of intrusive rocks associated with copper-gold porphyry deposits in the Canadian Cordillera; *in* Porphyry Deposits of the Northwestern Cordillera of North America, T.G. Schroeter (ed.), CIM Special Volume, no. 46, p. 142-158.

Mountjoy, D. (2011): Granitoid-hosted magnetite as an indicator mineral for porphyry Cu ore deposits; BSc Thesis, University of Victoria, Victoria, Canada, 41 pages.

Nadoll, P. & Koenig, A.E. (2011): LA-ICP-MS of magnetite: methods and reference materials; *Journal of Analytical Atomic Spectrometry*, vol. 26, p. 1872-1877.

Nadoll, P., Mauk, J.L., Hayes, T.S., Koenig, A.E. & Box, S.E. (2012): Geochemistry of magnetite from hydrothermal ore deposits and host rocks of the Mesoproterozoic Belt Supergroup, United States; *Economic Geology*, vol. 107, p. 1275-1292.

Nadoll, P., Angerer, T., Mauk, J.L., French, D. & Walshe, J. (2014): The chemistry of hydrothermal magnetite: a review; *Ore Geology Reviews*, vol. 61, p. 1-32.

Nadoll, P., Mauk, J.L., Leveille, R.A. & Koenig, A.E. (2015): Geochemistry of magnetite from porphyry Cu and skarn deposits in the southwestern United States; *Mineralium Deposita*, vol. 50, p. 493-515.

Newberry, N.G., Peacor, D.R., Essene, E.J. & Geissman, J.W. (1982): Silicon in magnetite: high resolution microanalysis of magnetite-ilmenite intergrowths; *Contributions to Mineralogy and Petrology*, vol. 80, p. 334-340.

Parent, M., Paradis, S.J. & Doiron, A. (1996): Palimpsest glacial dispersal trains and their significance for drift prospecting; *Journal of Geochemical Exploration*, vol. 56, p. 123-140.

Plouffe, A., Ferbey, T., Anderson, R.G., Hashmi, S. & Ward, B.C. (2013a): New TGI-4 till geochemistry and mineralogy results near the Highland Valley, Gibraltar, and Mount Polley mines, and Woodjam District: an aid to search for buried porphyry deposits; Geological Survey of Canada, Open File 7473, 58 pages.

Plouffe, A., Ferbey, T., Anderson, R.G., Hashmi, S., Ward, B.C. & Sacco, D.A. (2013b): The use of till geochemistry and mineralogy to explore for buried porphyry deposits in the Cordillera – preliminary results from a TGI-4 intrusion-related ore systems project; Geological Survey of Canada, Open File 7367, poster.

Razjigaeva, N.G. & Naumova, V.V. (1992): Trace element composition of detrital magnetite from coastal sediments of northwestern Japan Sea for provenance study; *Journal of Sedimentary Petrology*, vol. 62, no. 5, p. 802-809.

Rees, C. (2013): The Mount Polley Cu-Au porphyry deposit, south-central British Columbia, Canada; *in* 2013 Society of Economic Geologists Field Trip Guidebook, J. Logan & T. Schroeter (eds.), Series 43, p. 67-98.

Reimann, C. & Filzmoser, P. (2000): Normal and lognormal data distribution in geochemistry: death of a myth. Consequences for the statistical treatment of geochemical and environmental data; *Environmental Geology*, vol. 39, no. 9, p. 1001-1014.

Richards, J.P. (2015): The oxidation state, and sulfur and Cu contents of arc magmas: implications for metallogeny; *Lithos*, vol. 233, p. 27-45.

Roeder, P.L. (1994): Chromite: from the fiery rain of chondrules to the Kilauea Iki lava lake; *The Canadian Mineralogist*, vol. 32, no. 4, p. 729-746.

Ryder, J.M., Fulton, R.J. & Clague, J.J. (1991): The Cordilleran Ice Sheet and the glacial geomorphology of southern and central British Columbia; *Géographie Physique et Quaternaire*, vol. 45, no. 3, p. 365-377.

Sack, R.O. & Ghiorso, M.S. (1991): Chromian spinels as petrogenetic indicators: thermodynamics and petrological applications; *American Mineralogist*, vol. 76, p. 827-847.

Sappin, A.-A., Dupuis, C., Beaudoin, G., Pozza, M., McMartin, I. & McClenaghan, M.B. (2014): Optimal ferromagnetic fraction in till samples along ice-flow paths: case studies from the Sue-Dianne and Thompson deposits, Canada; *Geochemistry: Exploration, Environment, Analysis*, vol. 14, no. 4, p. 315-329.

Shau, Y.-H., Torii, M., Horng, C.-S. & Peacor, D.R. (2000): Subsolidus evolution and alteration of titanomagnetite in ocean ridge basalt from Deep Sea Drilling Project/Ocean Drilling Program Hole 504B, Leg 83: implications for the timing of magnetization; *Journal of Geophysical Research*, vol. 105, no. B10, p. 23,635-23,649.

Shcheka, S.A., Romanenko, I.M. & Chubarov, V.M. (1977): Silica-bearing magnetites; *Contributions to Mineralogy and Petrology*, vol. 63, p. 103-111.

Shiga, Y. (1988): Silician magnetite from the Kamaishe Mine, Japan; *Mining Geology*, vol. 38, no. 5, p. 437-440.

Sillitoe, R.H. (2000): Gold-rich porphyry deposits: descriptive and genetic models and their role in exploration and discovery; *Reviews in Economic Geology*, vol. 13, p. 315-345.

Sinclair, W.D. (2007): Porphyry deposits; *in* Mineral Deposits of Canada: A Synthesis of Major Deposit Types, District Metallogeny, the Evolution of the Geological Provinces, and Exploration Methods, W.D. Goodfellow (ed.), Geological Association of Canada, Mineral Deposits Division, Special Publication No. 5, p. 223-243.

Thompson, B. (1995): Stepwise regression and stepwise discriminant analysis need not apply here: a guidelines editorial; *Educational and Psychological Measurement*, vol. 55, no. 4, p. 525-534.

Turnock, A.C. & Eugster, H.P. (1962): Fe-Al oxides: phase relationships below 1000°C; *Journal of Petrology*, vol. 3, no. 3, p. 533-565.

Vermeesch, P. (2006): Tectonic discrimination diagrams revisited; *Geochemistry, Geophysics, Geosystems*, vol. 7, no. 6, 55 pages, http://dx.doi.org/10.1029/2005GC001092.

Verwey, E.J.W. & Heilmann, E.L. (1947): Physical properties and cation arrangement of oxides with spinel structures; *The Journal of Chemical Physics*, vol. 15, no. 4, p. 174-180.

Vincent, E.A. & Phillips, R. (1954): Iron-titanium oxide minerals in layered gabbros of the Skaergaard intrusion, East Greenland: Part I. Chemistry and ore-microscopy; *Geochimica et Cosmochimica Acta*, vol. 6, p. 1-26.

Waychunas, G.A. (1991): Crystal chemistry of oxides and oxyhydroxides; *in* Oxide Minerals: Petrologic and Magnetic Significance, D.H. Lindsley (ed.), Mineralogical Society of America, Reviews in Mineralogy, vol. 25, p. 11-68.

Weisse, P.A., Haggerty, S.E. & Brown, L.L. (1985): Paleomagnetism and magnetic mineralogy of the Nahant gabbro and tonalite, eastern Massachusetts; *Canadian Journal of Earth Sciences*, vol. 22, no. 10, p. 1425-1435.

Westendorp, R.W., Watkinson, D.H. & Jonasson, I.R. (1991): Silicon-bearing zoned magnetite crystals and the evolution of hydrothermal fluids at the Ansil Cu-Zn mine, Rouyn-Noranda, Quebec; *Economic Geology*, vol. 86, p. 1110-1114.

Whalen, J.B. & Chappell, B.W. (1988): Opaque mineralogy and mafic mineral chemistry of I- and S-type granites of the Lachlan fold belt, southeast Australia; *American Mineralogist*, vol. 73, p. 281-296.

Whiting, K.S. & Faure. G (1991): Transport of magnetite and ilmenite by glaciers in the Adirondack Mountains of New York; *The Journal of Geology*, vol. 99, no. 3, p. 482-492.

Yang, S., Wang, Z., Guo, Y., Li, C. & Cai, J. (2009): Heavy mineral compositions of the Changjiang (Yangtze River) sediments and their provenance-tracing implication; *Journal of Asian Earth Sciences*, vol. 35, p. 56-65.

Appendix A.
Till Sample Locations

Table 11. Coordinates for 74 till sample locations in the vicinity of the Mount Polley porphyry Cu-Au deposit.

			UTM Nad 83 Zone 10	
Till Sample	**Latitude (°N)**	**Longitude (°W)**	**Easting**	**Northing**
12PMA068A01	52.489691	121.800296	581457.14	5816181.81
12PMA069A01	52.493682	121.766509	583743.50	5816664.43
12PMA070A01	52.492312	121.732792	586035.15	5816551.68
12PMA071A01	52.500644	121.704341	587950.12	5817512.64
12PMA072A01	52.479967	121.686627	589194.28	5815234.61
12PMA073A01	52.597074	121.742664	585161.94	5828192.21
12PMA073A02	52.597074	121.742664	585161.94	5828192.21
12PMA075A01	52.587617	121.727151	586231.21	5827158.80
12PMA076A01	52.580769	121.710706	587358.87	5826416.88
12PMA077A01	52.573214	121.698597	588194.42	5825591.29
12PMA079A01	52.566539	121.681841	589343.51	5824869.48
12PMA080A01	52.565416	121.674724	589828.14	5824753.37
12PMA081A01	52.566351	121.661074	590751.38	5824874.45
12PMA083A01	52.571289	121.643891	591905.67	5825445.47
12PMA084A01	52.564112	121.684771	589149.85	5824595.95
12PMA086A01	52.579592	121.641286	592064.81	5826372.34
12PMA087A01	52.577354	121.637652	592315.69	5826128.02
12PMA088A01	52.575584	121.634374	592541.55	5825935.35
12PMA089A01	52.562829	121.629012	592931.83	5824523.56
12PMA091A01	52.549101	121.612081	594108.85	5823018.58
12PMA092A01	52.545711	121.645766	591832.00	5822598.13
12PMA092A02	52.545711	121.645766	591832.00	5822598.13
12PMA093A01	52.549929	121.651264	591450.40	5823060.33
12PMA093A02	52.549929	121.651264	591450.40	5823060.33
12PMA094A01	52.589349	121.720366	586687.43	5827359.55
12PMA095A01	52.582802	121.692107	588614.88	5826665.72
12PMA097A01	52.514849	121.684147	589292.00	5819117.38
12PMA098A01	52.521726	121.664167	590633.60	5819907.13
12PMA099A01	52.528602	121.688141	588993.23	5820642.16
12PMA100A01	52.538786	121.692626	588668.48	5821769.29
12PMA101A01	52.546492	121.690774	588778.50	5822628.75
12PMA101A02	52.546492	121.690774	588778.50	5822628.75
12PMA102A01	52.555422	121.678784	589573.32	5823636.81
12PMA103A01	52.569561	121.653644	591248.29	5825240.86

			UTM Nad 83 Zone 10	
Till Sample	**Latitude (°N)**	**Longitude (°W)**	**Easting**	**Northing**
12PMA564A01	52.420292	121.858251	577644.24	5808399.14
12PMA565A01	52.438282	121.859584	577522.00	5810398.65
12PMA566A01	52.451229	121.855536	577774.37	5811843.00
12PMA567A01	52.503189	121.806964	580979.58	5817675.67
12PMA568A01	52.513044	121.790547	582075.49	5818790.34
12PMA568A02	52.513044	121.790547	582075.49	5818790.34
12PMA569A01	52.515647	121.761541	584038.89	5819113.27
12PMA570A01	52.523416	121.782744	582585.57	5819952.84
12PMA571A01	52.527824	121.762216	583969.86	5820466.85
12PMA572A01	52.529914	121.792466	581913.93	5820664.55
12PMA573A01	52.534746	121.812699	580532.60	5821179.19
12PMA574A01	52.553882	121.735326	585743.18	5823396.83
12PMA575A01	52.549236	121.758997	584147.23	5822852.14
12PMA576A01	52.547672	121.788314	582162.39	5822644.47
12PMA577A01	52.566774	121.775164	583017.97	5824784.14
12PMA578A01	52.568979	121.720789	586698.93	5825093.35
12PMA579A01	52.570379	121.742596	585218.33	5825223.09
12PMA580A01	52.574546	121.762289	583875.75	5825663.45
12PMA581A01	52.580944	121.787646	582145.52	5826345.94
12PMA583A01	52.586844	121.780797	582598.43	5827010.00
12PMA584A01	52.596321	121.783749	582380.69	5828060.69
12PMA585A01	52.610061	121.712681	587166.90	5829672.50
12PMA586A01	52.619134	121.773592	583025.45	5830609.82
12PMA587A01	52.617357	121.674216	589756.39	5830531.28
12PMA588A01	52.620519	121.647276	591573.56	5830916.82
12TFE078A01	52.585202	121.559602	597586.81	5827103.69
12TFE079A01	52.537687	121.565501	597292.30	5821810.90
12TFE080A01	52.540566	121.550784	598283.95	5822150.98
12TFE085A01	52.518077	121.539942	599069.77	5819664.57
12TFE086A01	52.491166	121.677439	589795.45	5816491.53
12TFE087A01	52.497349	121.648407	591753.59	5817215.75
12TFE088A01	52.507012	121.612202	594190.60	5818337.17
12TFE089A01	52.512812	121.575881	596642.92	5819030.27
12TFE090A01	52.510746	121.542022	598945.11	5818846.27
12TFE097A01	52.634004	121.732572	585773.23	5832311.80
12TFE101A01	52.632491	121.688127	588783.97	5832197.29
12TFE101A02	52.632491	121.688127	588783.97	5832197.29
12TFE102A01	52.619309	121.663602	590470.86	5830761.63
12TFE103A01	52.613042	121.694664	588380.78	5830026.08
12TFE104A01	52.655052	121.641451	591895.47	5834765.27

Sample locations from this study are in bold.

Appendix B.
Magnetite from Till: Petrography, LA-ICP-MS Compositional Data & LDA Classification

Data file: Appendix B_till magnetite.xlsx

Description: Petrography and compositional data for detrital magnetite grains from till (n = 985). All LA-ICP-MS data is calibrated using the AYCF method. Classification results from linear discriminant analyses, LDA1 and LDA2, and the Ti vs. Ni/Cr diagram also given.

Appendix C.
Detection Limits for EMP Analysis

Table 12. Minimum, mean and maximum detection limits for electron microprobe analysis.

Element (ppm)	DL (min)	DL (max)	DL (mean)
Mg	312	388	352
Al	278	321	301
Si	404	844	588
Ca	371	467	409
Ti	514	668	573
V	253	700	581
Cr	9	578	463
Mn	867	1257	1021
Fe	4000	4927	4536
Ni	844	979	928

Appendix D.
Accuracy and Precision of LA-ICP-MS Analysis

Supplementary data file: Appendix D_BCR2g data.xlsx

Description: LA-ICP-MS analytical results for BCR2g including estimates of accuracy and precision.

Figure 25. Accuracy of LA-ICP-MS analyses recorded from September 16, 2013 through April 20, 2015 using the USGS basaltic glass reference BCR2g.

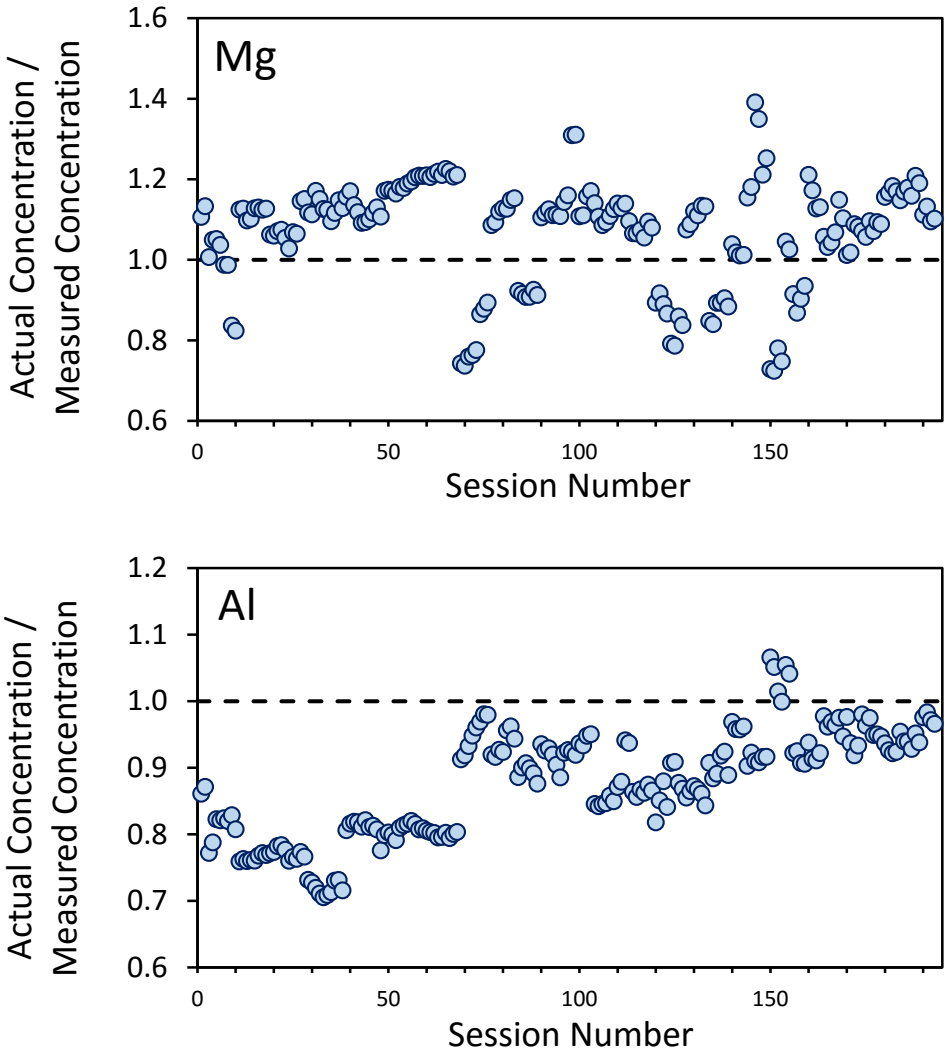

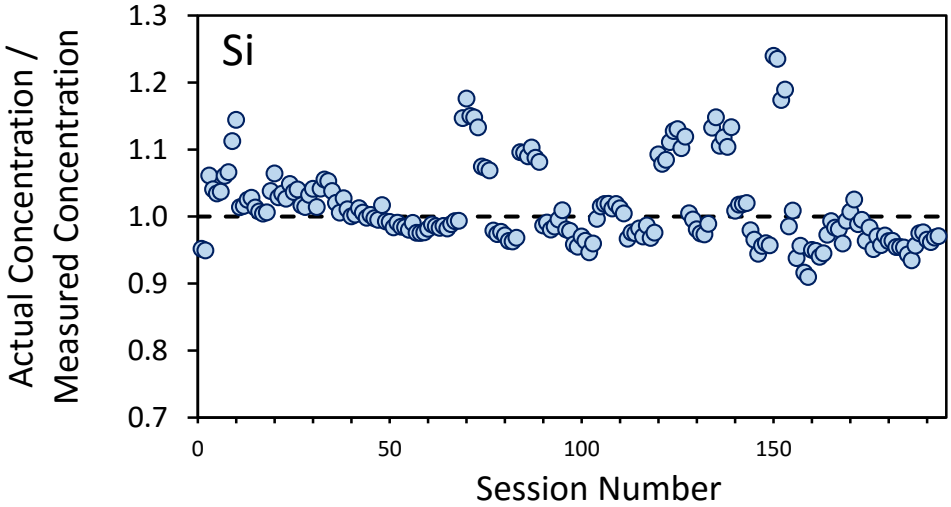
Si
Actual Concentration / Measured Concentration
1.3
1.2
1.1
1.0
0.9
0.8
0.7
0
50
100
150
Session Number

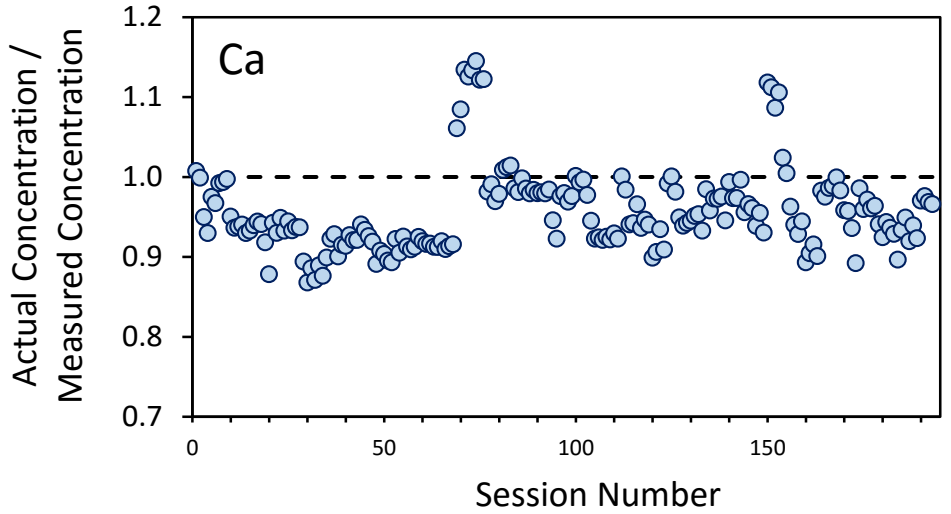
Ca
Actual Concentration / Measured Concentration
1.2
1.1
1.0
0.9
0.8
0.7
0
50
100
150
Session Number

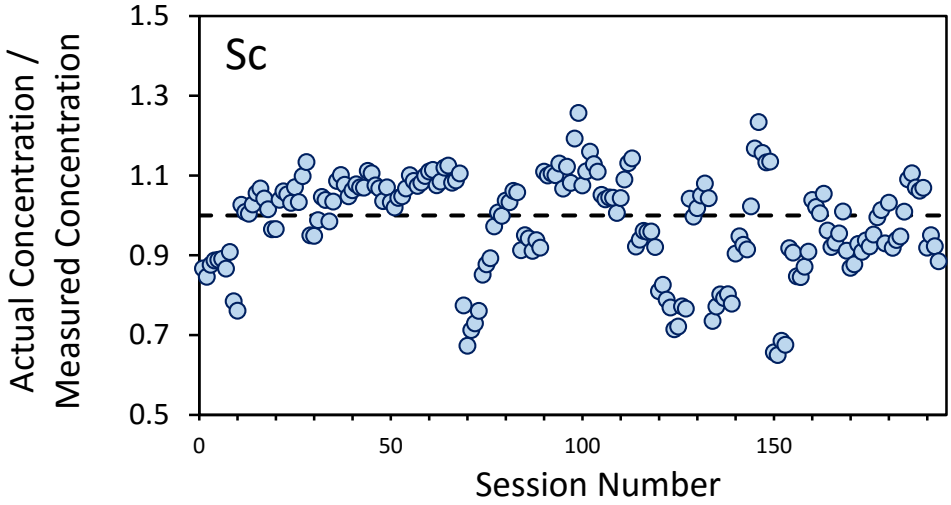
Sc
Actual Concentration / Measured Concentration
1.5
1.3
1.1
0.9
0.7
0.5
0
50
100
150
Session Number

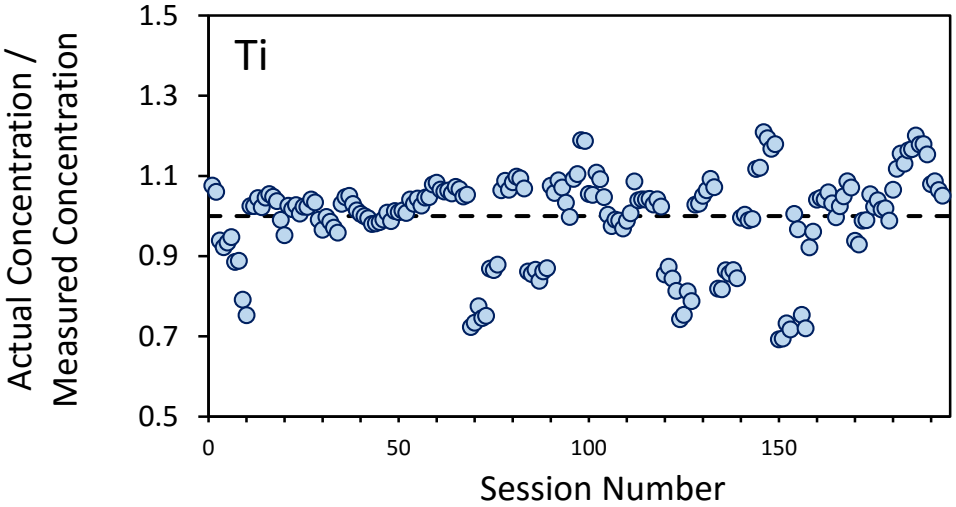
Ti
Actual Concentration / Measured Concentration
1.5
1.3
1.1
0.9
0.7
0.5
0
50
100
150
Session Number

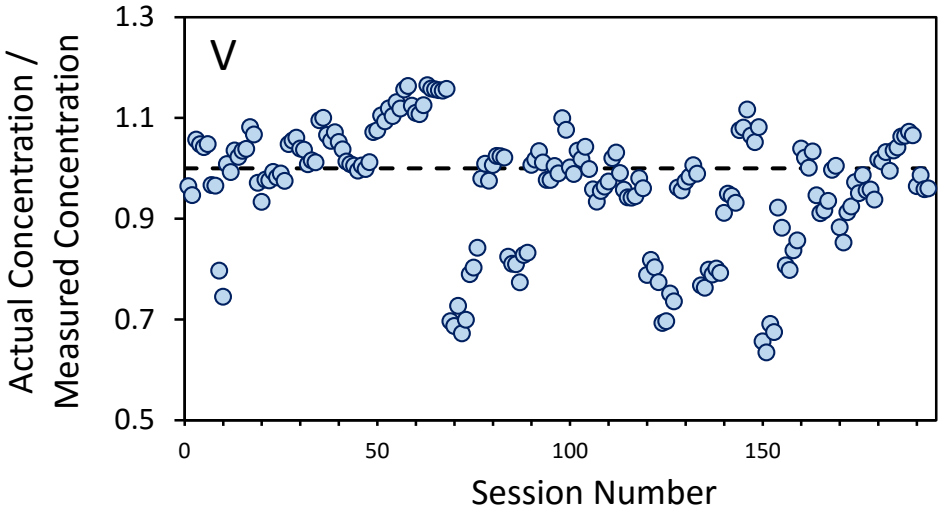
V
Actual Concentration / Measured Concentration
1.3
1.1
0.9
0.7
0.5
0
50
100
150
Session Number

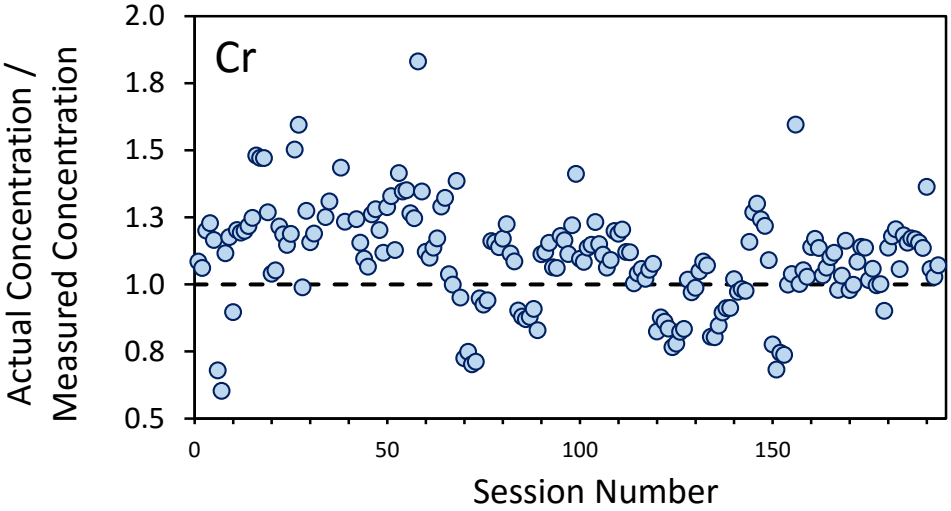
Cr
Actual Concentration / Measured Concentration
2.0
1.8
1.5
1.3
1.0
0.8
0.5
0
50
100
150
Session Number

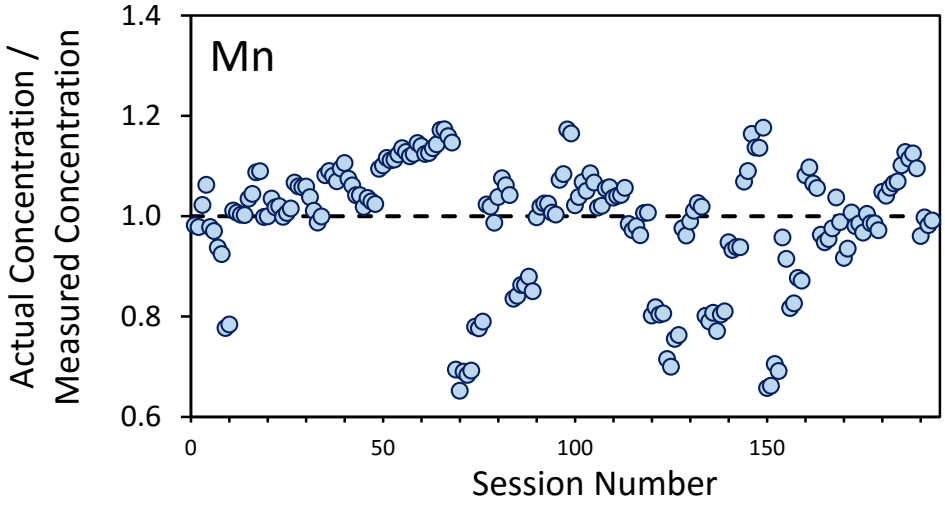
Mn
Actual Concentration / Measured Concentration
1.4
1.2
1.0
0.8
0.6
0
50
100
150
Session Number

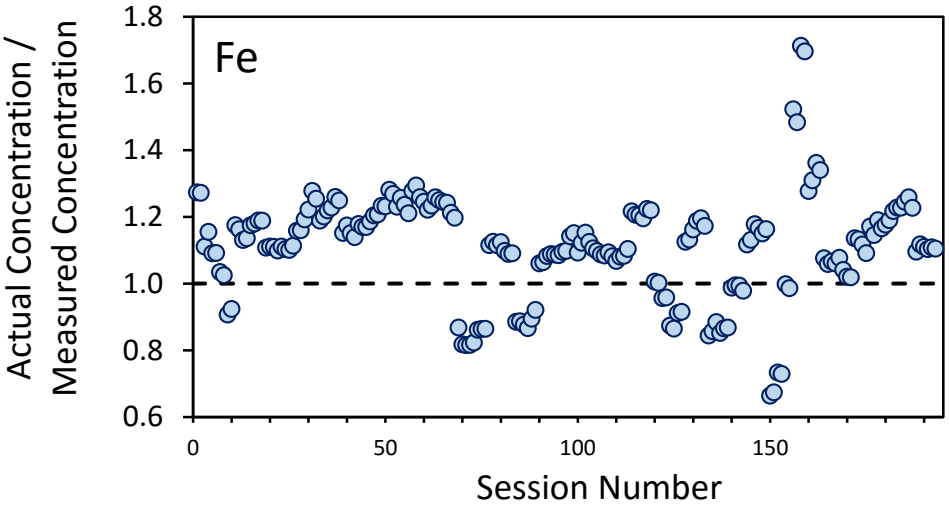
Fe
Actual Concentration / Measured Concentration
1.8
1.6
1.4
1.2
1.0
0.8
0.6
0
50
100
150
Session Number

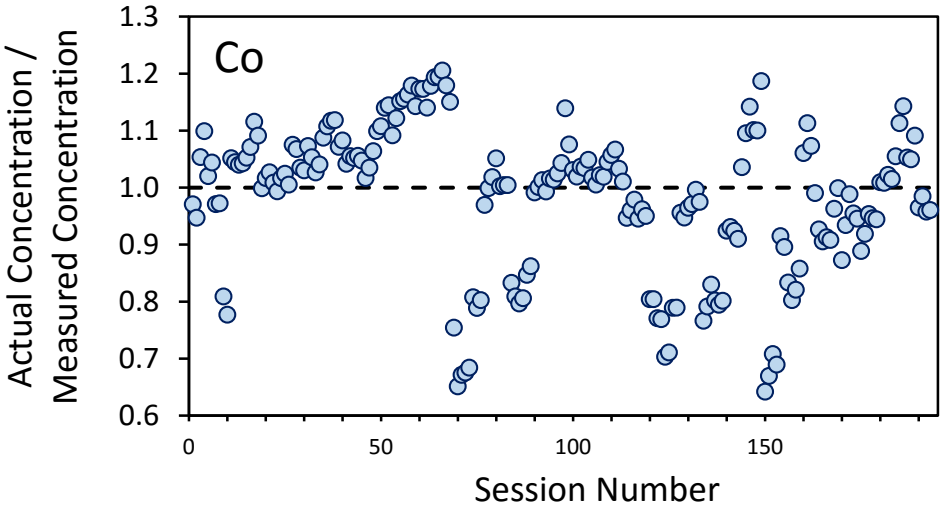
Co
Actual Concentration / Measured Concentration
1.3
1.2
1.1
1.0
0.9
0.8
0.7
0.6
0
50
100
150
Session Number

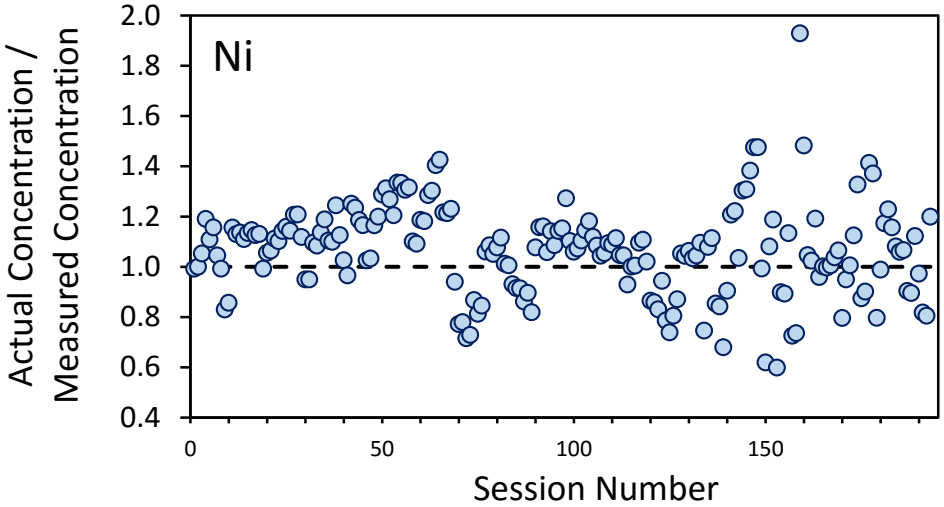
Ni
Actual Concentration / Measured Concentration
2.0
1.8
1.6
1.4
1.2
1.0
0.8
0.6
0.4
0
50
100
150
Session Number

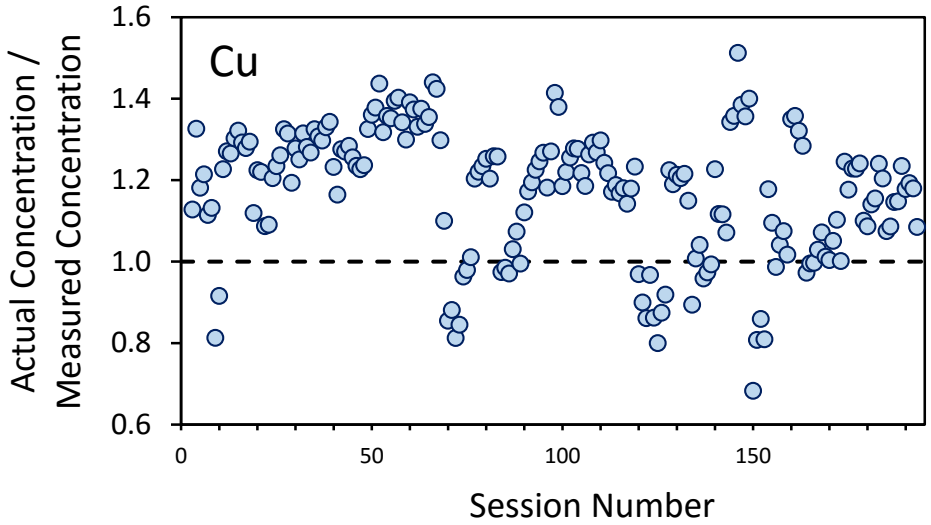
Cu
Actual Concentration / Measured Concentration
1.6
1.4
1.2
1.0
0.8
0.6
0
50
100
150
Session Number

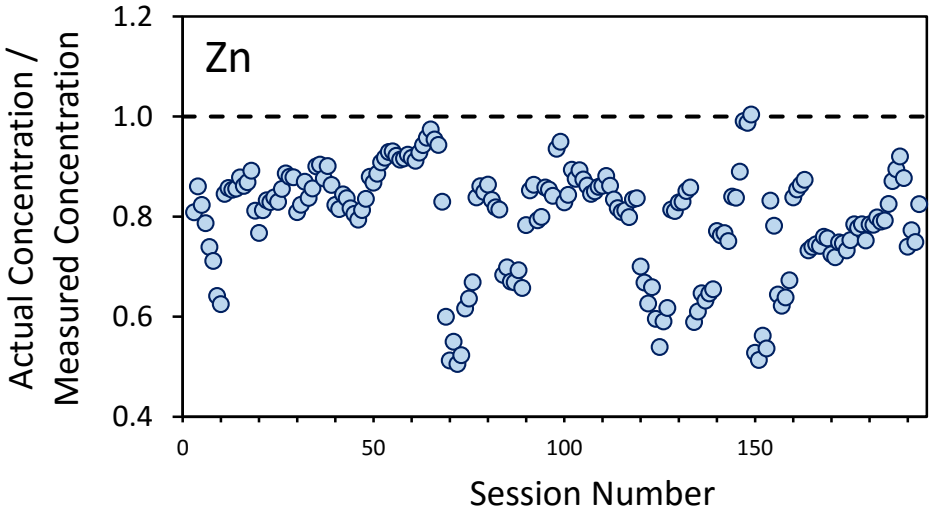
Zn
Actual Concentration / Measured Concentration
1.2
1.0
0.8
0.6
0.4
0
50
100
150
Session Number

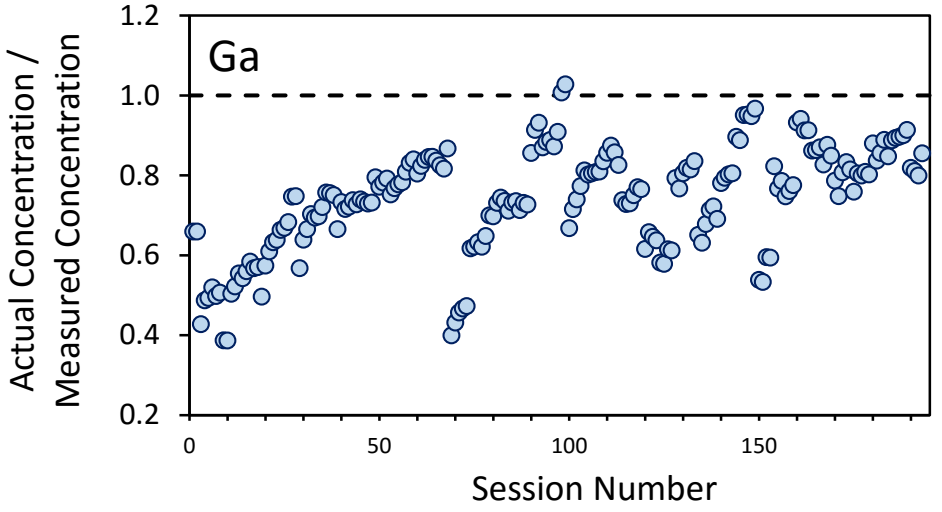
Ga
Actual Concentration / Measured Concentration
1.2
1.0
0.8
0.6
0.4
0.2
0
50
100
150
Session Number

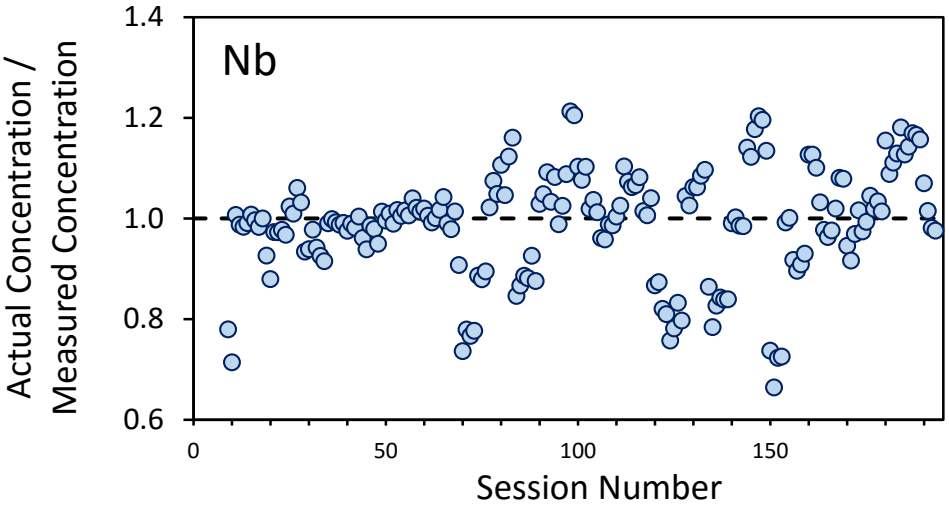
Nb
Actual Concentration / Measured Concentration
1.4
1.2
1.0
0.8
0.6
0
50
100
150
Session Number

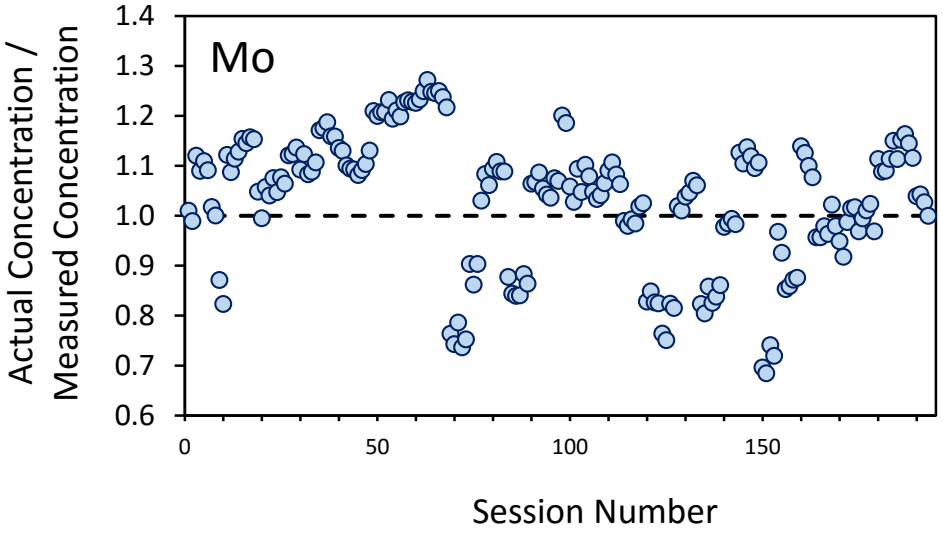
Mo
Actual Concentration / Measured Concentration
1.4
1.3
1.2
1.1
1.0
0.9
0.8
0.7
0.6
0
50
100
150
Session Number

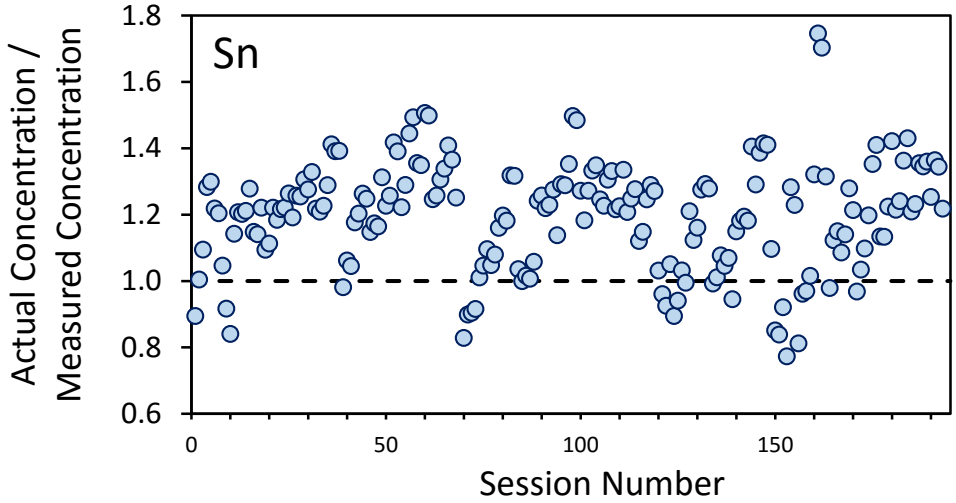
Sn
Actual Concentration / Measured Concentration
1.8
1.6
1.4
1.2
1.0
0.8
0.6
0
50
100
150
Session Number

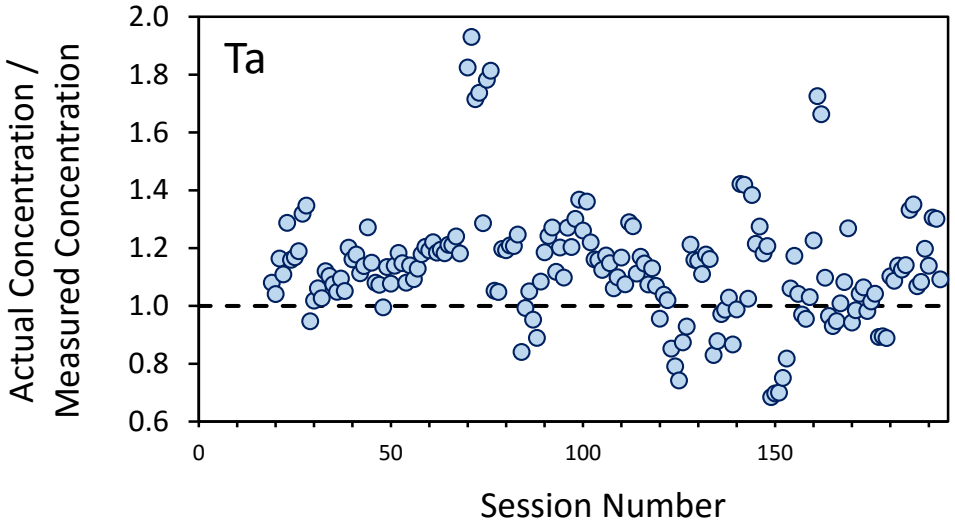
Ta
Actual Concentration / Measured Concentration
2.0
1.8
1.6
1.4
1.2
1.0
0.8
0.6
0
50
100
150
Session Number

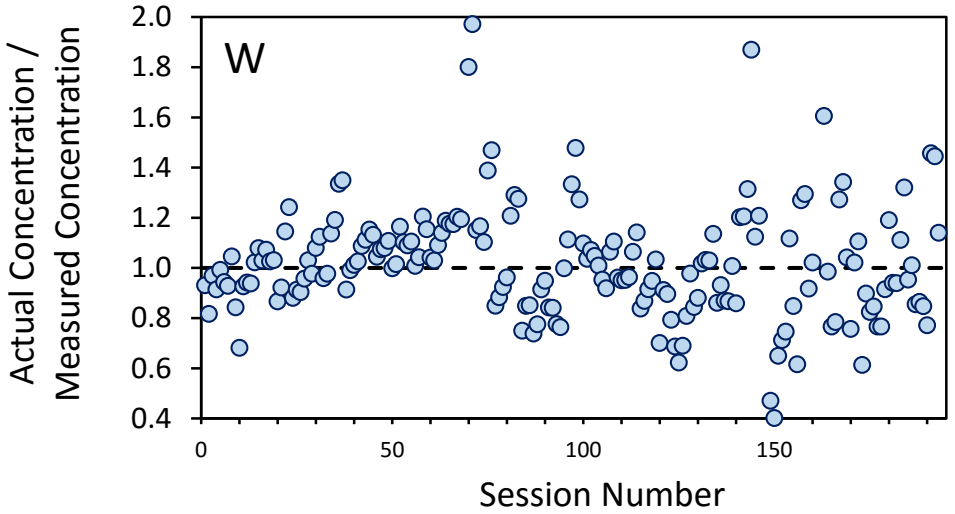
W
Actual Concentration / Measured Concentration
2.0
1.8
1.6
1.4
1.2
1.0
0.8
0.6
0.4
0
50
100
150
Session Number

Appendix E.
SYSTAT 13 Output for Linear Discriminant Analysis

Linear Discriminant Analysis: MDB1

▼Classical Discriminant Analysis

Group Frequencies

BIG	HTP	OIG
40	132	46

Group Means

	BIG	HTP	OIG
MG	-6.871	-6.843	-7.757
AL	-4.446	-6.107	-5.514
V	-5.072	-5.895	-5.892
MN	-5.965	-5.779	-6.478
CO	-9.663	-10.070	-9.584
NI	-10.158	-10.229	-9.334

Between Groups F-matrix
df : 6 210

	BIG	HTP	OIG
BIG	0.000		
HTP	44.239	0.000	
OIG	14.464	38.931	0.000

Wilks's Lambda

Lambda	:	0.268
df	:	(6,2,215)
Approx. F-ratio	:	32.669
df	:	(12,420)
p-value	:	0.000

Classification Functions

	BIG	HTP	OIG
CONSTANT	-274.388	-296.442	-256.021

MG	4.476	6.097	3.984
AL	-10.580	-14.579	-11.305
V	14.785	13.468	12.418
MN	-11.669	-9.799	-10.009
CO	-30.950	-32.785	-30.224
NI	-23.293	-23.070	-21.115

Variable		F-to-remove	Tolerance	Variable		F-to-enter	Tolerance
6	MG	49.546	0.494				
7	AL	115.622	0.426				
9	V	17.211	0.451				
10	MN	21.233	0.354				
11	CO	16.341	0.702				
12	NI	24.432	0.565				

Classification Matrix (Cases in row categories classified into columns)

	BIG	HTP	OIG	%correct
BIG	37	1	2	93
HTP	7	111	14	84
OIG	1	3	42	91
Total	45	115	58	87

Jackknifed Classification Matrix

	BIG	HTP	OIG	%correct
BIG	37	1	2	93
HTP	7	109	16	83
OIG	2	5	39	85
Total	46	115	57	85

Eigenvalues

1.667	**0.402**

Canonical Correlations

0.791	**0.535**

Cumulative Proportion of Total Dispersion

0.806	**1.000**

Test Statistic

Statistic	Value	Approx. F-ratio	df		p-value
Wilks's Lambda	0.268	32.669	12	420	0.000
Pillai's Trace	0.912	29.453	12	422	0.000
Lawley-Hotelling Trace	2.069	36.027	12	418	0.000

Canonical Discriminant Functions

	1	2
Constant	-12.150	-11.256

MG	0.703	0.384
AL	-1.387	0.091
V	-0.075	1.169
MN	0.412	-0.750
CO	-0.827	-0.525
NI	-0.306	-1.149

Canonical Discriminant Functions : Standardized by Within Variances

	1	2
MG	0.956	0.521
AL	-1.401	0.092
V	-0.066	1.039
MN	0.549	-1.000
CO	-0.509	-0.323
NI	-0.268	-1.005

Canonical Scores of Group Means

	1	2
BIG	-1.791	0.995
HTP	1.030	0.049
OIG	-1.399	-1.005

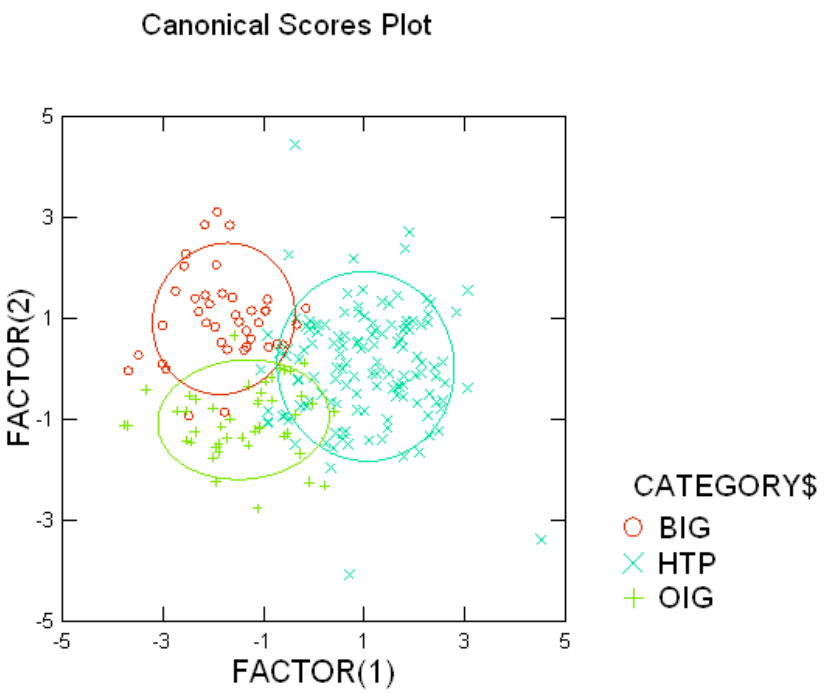

Linear Discriminant Analysis: MDB2

▼Classical Discriminant Analysis

Group Frequencies

BIG	HTP	OIG
49	140	64

Group Means

	BIG	HTP	OIG
MG	-6.940	-6.894	-7.739
AL	-4.708	-6.095	-5.651
TI	-4.688	-5.753	-5.759
V	-5.152	-5.959	-5.834
MN	-5.979	-5.842	-6.486
CO	-9.551	-10.069	-9.782
NI	-9.994	-10.195	-9.219

Between Groups F-matrix
df : 7 244

	BIG	HTP	OIG
BIG	0.000		
HTP	36.699	0.000	
OIG	11.015	31.299	0.000

Wilks's Lambda

Lambda	:	0.328
df	:	(7,2,250)
Approx. F-ratio	:	26.040
df	:	(14,488)
p-value	:	0.000

Classification Functions

	BIG	HTP	OIG
CONSTANT	-254.904	-290.051	-257.607
MG	2.133	3.389	1.668
AL	-19.187	-23.275	-20.374
TI	7.307	8.123	7.744
V	2.671	1.025	1.197
MN	-9.528	-8.647	-8.716
CO	-23.189	-24.750	-23.800
NI	-20.176	-20.846	-18.769

Variable		F-to-remove	Tolerance	Variable		F-to-enter	Tolerance
6	MG	40.192	0.529				
7	AL	84.253	0.314				
8	TI	7.443	0.293				
9	V	12.416	0.511				
10	MN	6.267	0.415				
11	CO	8.025	0.806				
12	NI	33.528	0.639				

Classification Matrix (Cases in row categories classified into columns)

	BIG	HTP	OIG	%correct
BIG	42	2	5	86
HTP	5	112	23	80
OIG	6	10	48	75
Total	53	124	76	80

Jackknifed Classification Matrix

	BIG	HTP	OIG	%correct
BIG	41	2	6	84
HTP	5	111	24	79
OIG	7	12	45	70
Total	53	125	75	78

Eigenvalues

1.356	**0.295**

Canonical Correlations

0.759	**0.477**

Cumulative Proportion of Total Dispersion

0.821	**1.000**

Test Statistic

Statistic	Value	Approx. F-ratio	df		p-value
Wilks's Lambda	0.328	26.040	14	488	0.000
Pillai's Trace	0.804	23.508	14	490	0.000
Lawley-Hotelling Trace	1.652	28.668	14	486	0.000

Canonical Discriminant Functions

	1	2
Constant	-14.699	-2.355

MG	0.627	0.477
AL	-1.500	0.281
TI	0.259	-0.192
V	-0.404	0.790
MN	0.212	-0.439
CO	-0.541	0.215
NI	-0.567	-1.043

Canonical Discriminant Functions : Standardized by Within Variances

	1	2
MG	0.814	0.619
AL	-1.493	0.279
TI	0.529	-0.392
V	-0.354	0.691
MN	0.275	-0.571
CO	-0.354	0.141
NI	-0.501	-0.920

Canonical Scores of Group Means

	1	2
BIG	-1.553	0.831
HTP	1.030	0.068
OIG	-1.064	-0.784
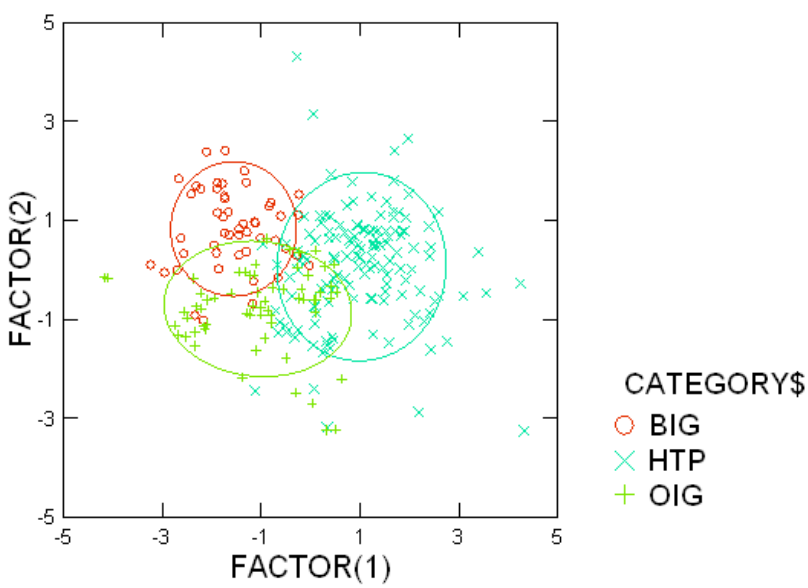
Canonical Scores Plot